ISSN 2683-9288

Science Reviews
from the end of the world

Volume 1
Number 2
March 2020

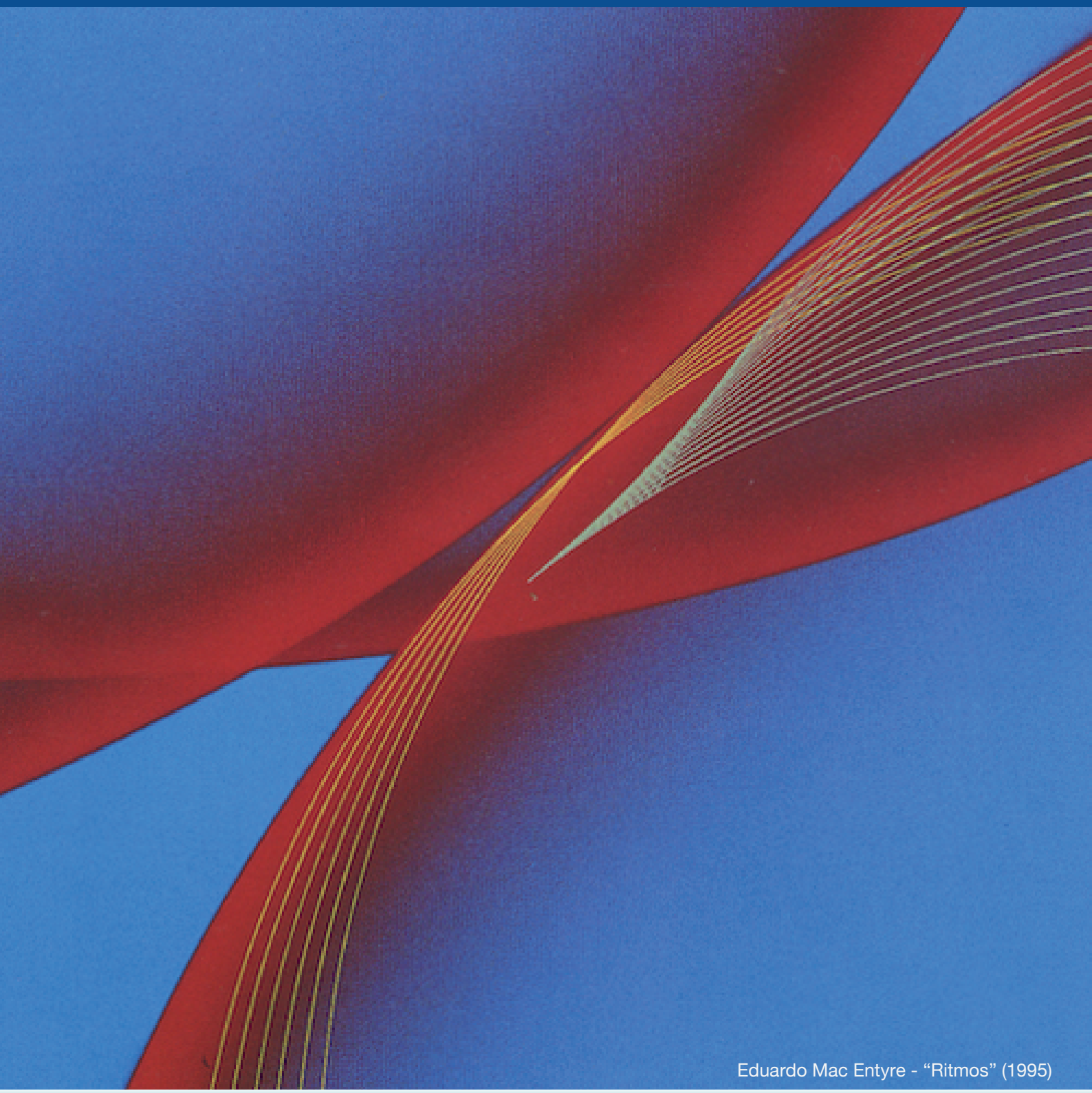

Eduardo Mac Entyre - “Ritmos” (1995)

Science Reviews
from the end of the world

Science Reviews - from the end of the world **is a quaterly publication that aims at providing authoritative reviews on hot research topics developed mainly by scientists that carry out their work far away from the main centers of science. Its research reviews are short, concise, critical and easy-reading articles describing the state of the art on a chosen hot topic, with focus on the research carried out by the authors of the article. These articles are commissioned by invitation and are accessible not only to hardcore specialists, but also to a wider readership of researchers interested in learning about the state-of-the-art in the reviewed subject. The reviews cover all fields of science and are written exclusively in English. They are refereed by peers of international prestige and the evaluation process follows standard international procedures.**

Centro de Estudios sobre Ciencia, Desarrollo y Educación Superior
538 Pueyrredón Av. - 2° C – Second building
Buenos Aires, Argentina - C1032ABS
(54 11) 4963-7878/8811
sciencereviews@centroredes.org.ar
www.scirevfew.net

Vol. 1, No. 2
March 2020

ISSN 2683-9288

Our cover: *Ritmos* (1995), oil on canvas by Eduardo Mac Entyre. From the collection Artistas plásticos con la ciencia. Reproduced by permission from the Comisión Administradora Permanente de la Exposición de Arte Centro Atómico Constituyentes, Comisión Nacional de Energía Atómica.

Science Reviews
from the end of the world

Table of Contents

Science Reviews
from the end of the world

Vol. 1, No. 2, March 2020 //

EDITORIAL

Awesome Chemistry from the End of the World

The second number of this first volume of *Science Reviews from the End of the World*, is dedicated to chemistry, more specifically, charge transfer processes in transition metal complexes. While Profs. Katz and Wolcan discuss the subject focused on inorganic complexes (attached to polymers in the case of Wolcan), Profs. Murgida and Brondino *et al* dedicate their reviews to metalloproteins. Therefore, we could say that the areas represented in this issue are inorganic, organometallic and bioinorganic chemistry.

The four featured researchers and their groups are from different cities of Argentina, distributed throughout the country: Buenos Aires, La Plata, Santa Fe and Tucumán. They are world leaders in their fields and regularly publish their research in first-class journals. As an editor, I am not only pleased but also thankful that they have accepted to participate in this journal, which is not only just starting, but also edited at the *End of the World*. We decided to add this subtitle to the journal, at first because of the famous lighthouse located at the very south of Argentina, referred to by Jules Verne in his novel *The Lighthouse at the End of the World*. However, this is not the only reason for using this reference – since our country is the southernmost country in South of America, we are often quite isolated from the rest of the world. Not only because of the distances that we have to travel – especially nowadays, with airplanes that make travelling a fast and easy journey – but also due to the high costs associated with that. In general, the grants provided by the State are quite tiny, a tenth or even a hundredth of the amounts granted in Europe, USA and other first-world countries. Nevertheless, our works are judged in the first-class journals by applying the same rules and guidelines applied to any submitted manuscript, which makes the works presented in this "editorial anomaly" even more attractive and unique.

Fabio Doctorovich
Editor

Bio

Fabio Doctorovich

Full Professor at the University of Buenos Aires (UBA, Argentina) and Researcher at CONICET, he obtained his PhD in Organic Chemistry from UBA in 1990. He was a postdoctoral fellow at the Georgia Institute of Technology working with Prof. E.C. Ashby and K. Barefield, first on single electron transfer, and afterwards on chemical reactions taking place in nuclear waste tanks. Back in Argentina, he started to work on nitric oxide (NO), including organic nitrosocompounds, inorganic iron, rhodium, ruthenium and iridium nitrosyl complexes, and reactivity of metalloporphyrins and pincer complexes towards HNO. He also worked on CO complexes, catalytic reactions, and other topics. Nowadays his main research focus is on reactions involving HNO. Prof. Doctorovich has published over 120 works in international journals such as *Accounts of Chemical Research, Journal of the American Chemical Society, Inorganic Chemistry, Nature Communications*, as well as the book *The Chemistry and Biology of Nitroxyl (HNO)* published at Elsevier, 2016. He has supervised 15 Ph. D. students. In 2011 he received the Guggenheim Fellowship and in 2016 the Innovar Prize.

IN THIS ISSUE

Science Reviews
from the end of the world

Vol. 1, No.2, March 2020 // pp. 6-23 /

Studying Electron Transfer Pathways in Oxidoreductases

María Gabriela Rivas, Pablo J. González, Felix M. Ferroni, Alberto C. Rizzi, and Carlos D. Brondino*

Departamento de Física, Facultad de Bioquímica y Ciencias Biológicas, Universidad Nacional del Litoral, Santa Fe, Argentina.
**Corresponding author. E-mail: brondino@fbcb.unl.edu.ar*

Abstract

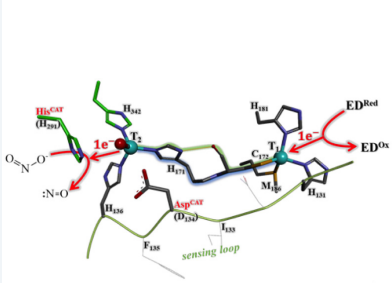

Oxidoreductases containing transition metal ions are widespread in nature and are essential for living organisms. The copper-containing nitrite reductase (NirK) and the molybdenum-containing aldehyde oxidoreductase (Aor) are typical examples of oxidoreductases. Metal ions in these enzymes are present either as mononuclear centers or organized into clusters and accomplish two main roles. One of them is to be the active site where the substrate is converted into product, and the other one is to serve as electron transfer center. Both enzymes transiently bind the substrate and an external electron donor/acceptor in NirK/Aor, respectively, at distinct protein points for them to exchange the electrons involved in the redox reaction. Electron exchange occurs through a specific intra-protein chemical pathway that connects the different enzyme metal cofactors. Based on the two oxidoreductases presented here, we describe how the different actors involved in the intra-protein electron transfer process can be characterized and studied employing molecular biology, spectroscopic, electrochemical, and structural techniques.

Keywords:
electron transfer pathways, oxidoreductases, transition metal ions

Introduction

Proteins are the most versatile macromolecules in living organisms. They have key roles in every metabolic pathway occurring inside living cells as (bio)catalysts, transporting and/or storing essential molecules, providing mechanical support and immune protection, generating movement, transmitting electric impulses, and controlling cell growth and differentiation (Berg *et al.,* 2012). About a third of all proteins present in living organisms contains one or more transition metal ions as cofactors and are called metalloproteins or metalloenzymes, accordingly (Silva and Williams, 1991). Metalloenzymes occur in the six Enzyme Commission Classes (E.C.C.). Within the oxidoreductases group (EC 1), almost half (44%) are metalloenzymes. A large percentage of transferases (EC 2, 40%), hydrolases (EC 3, 39%), lyases (EC 4, 36%), isomerases (EC 5, 36%), and ligases (EC 6, 59%), are also metalloenzymes (Andreini *et al.,* 2008).

Metalloenzymes of the oxidoreductase group catalyze specific reactions in which metal ions are part of the enzyme active site, function as electron transfer (ET) centers, or, less frequently, stabilize protein structure. These enzymes incorporate 81 % of the total Fe found in living organisms, as well as 93% of the total Cu, and 81% of total Mo plus W (Andreini *et al.* 2008). These four metals are the so-called redox-active elements of life since they can exist in several

oxidation states within the physiological range of electrochemical potential that can be handled by a living cell (*ca* from -800 to +800 mV, *vs* SHE). The redox cycling of these transition metal ions is the basis for them to work as electron conduits, mediating ET from the enzyme active site to a redox partner, and *vice versa*.

Oxidoreductases have an active site where the oxidation or reduction of the substrate occurs. In the first case, electrons obtained from substrate oxidation reduce the active site, and then are transferred through redox cofactors buried in the protein to a surface exposed center capable of reducing an electron acceptor (EA). On the other hand, when the enzyme catalyzes the reduction of a substrate, the process is the inverse. The electron donor (ED) transfers electrons to a surface exposed redox center of the enzyme, and electrons are conducted through an intra-protein chemical pathway to the active site where substrate reduction occurs. The processes described above stand for an important group of oxidoreductases, even though some develop the redox reaction in a single protein site. It should be noted that oxidoreductases catalyze bisubstrate reactions and the labeling of substrate and ED (or EA) is biased by the interests of the researcher. For example, a compound can be called "the substrate" because it is economically relevant for the pharma, fuel, or fine chemicals industry, or simply because it reacts at a particular enzyme site that is being thoroughly studied because it has some relevant and/or novel properties. Even though we will use this jargon throughout the manuscript, it is important to remark that the correct way of stating this is that an oxidoreductase has two substrates.

The oxidoreductases we describe here perform long-distance ET reactions. Long-range ET, which occurs through electron tunneling either within an enzyme or between proteins, is fundamental to several cellular processes, mainly those related to energy metabolism (Davidson, 1996; Davidson, 2002). Therefore, for researchers working with redox enzymes and ET proteins, the knowledge of ET theory and the role of the parameters that control ET rates are relevant to understand at a molecular level how an enzyme regulates a physiological process. Moreover, this knowledge might be used to design biocatalysts by exploiting the chemistry of oxidoreductases, or even to understand the effect of a point mutation in human diseases (Moser *et al.,* 2010).

The aim of this paper is to describe different experimental techniques that can be used to characterize and understand ET processes in oxidoreductases, and how some parameters that control ET rates can be experimentally measured or at least estimated independently. First, we will explain how to use voltamperometric and spectropotentiometric methods to characterize the redox properties of the metal centers comprising the ET pathway. Then, we will discuss different strategies to evaluate the ability of a given chemical path to act as ET pathway. Finally, we will show how X-ray data and molecular biology techniques, more specifically site-directed mutagenesis, can be used to predict ET pathways within a protein. All these methodologies/strategies will be explained based on two representative examples of oxidoreductases – a copper-containing nitrite reductase (NirK), which catalyzes the reduction of nitrite to nitric oxide, and a molybdenum-containing aldehyde oxidoreductase (Aor), which catalyzes the oxidation of aldehyde to the respective carboxylic acid.

1. Structural aspects and general reaction mechanisms of NirK and Aor

Figure 1 shows the essential metal cofactors for catalysis in NirK and Aor together with the intra-protein chemical pathways that link the metal cofactors through which ET occurs. Copper-containing NirK presents a homotrimeric structure with two copper atoms *per* monomer ~ 12 Å apart, one of type 1 (T1, also blue copper) and the other of type 2 (T2, also normal copper) (Nojiri, 2017). T1 and T2 are the ET center and the active site, respectively. The T1 copper ion is tetracoordinated with three strongly bound ligands, two N atoms from histidine imidazoles and a cysteine thiolate group, and a weaker methionine thioether group. Subtle differences in the T1 electronic structure determines the green or blue color of NirK from different organisms. On the other hand, T2 consists of a four-coordinate copper site bound to a labile water molecule and three N atoms from histidine imidazoles in a distorted tetrahedral geometry. The two copper sites are connected by two main chemical pathways – the shorter one, the Cys-His bridge, is thought to transport the electron needed for nitrite reduction to nitric oxide; the longer pathway, which has been called the substrate-sensing loop, is thought to work as a relay to trigger the T1→T2 electron flow through the Cys-His bridge upon nitrite-T2 binding (Strange *et al.,* 1999; Boulanger *et al.,* 2000). This sensing loop contains an aspartic acid residue (Asp^{CAT}) that forms a hydrogen bond with the T2 labile water molecule in the resting state, and with the nitrite-T2 complex in NirK reacted with nitrite (not shown); Asp^{CAT} was proposed to be essential in catalysis (Boulanger *et al.,* 2000, Kataoka *et al.,* 2000). The proposed reaction mechanism for NirK implies a two-proton coupled redox reaction in which nitrite, after binding T2, is converted to nitric oxide by one electron delivered by an external physiological ED (Suzuki *et al.,* 1994; Fukuda *et al.,* 2016; Nojiri 2017). The physiological ED of NirK were identified to be pseudoazurin, azurin or cytochrome *c*, depending on the microorganism. Thus, the complete ET implies three intermolecular reactions: an inter-protein ET between the physiological ED and the NirK T1 center, the T1-T2 intra-protein ET, and the ET reaction between T2 and substrate. Hereafter, the ET pathways discussed in this paper will refer only to the protein intramolecular step.

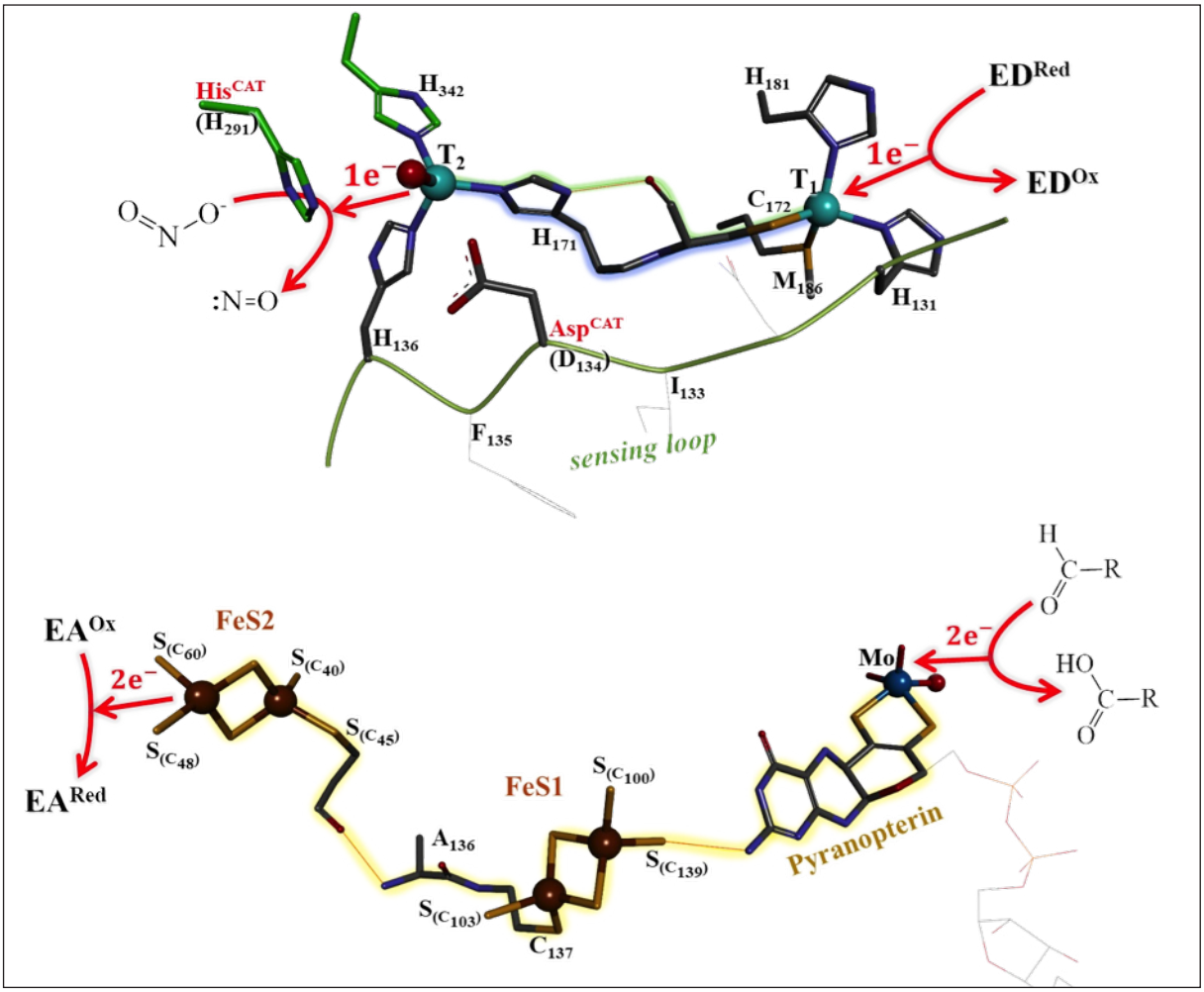

Figure 1. Metal centers in NirK (top) and Aor (bottom) together with the proposed intra-protein ET pathways. For NirK, the two alternative intra-protein ET pathways are highlighted in blue and green (Hadt *et al.,* 2014). The blue subpath is a pure covalent chemical pathway constituted by the protein backbone and the H171 and C172 side chains, whereas the green one involves the His-N$^{\delta 1}$H…O=C-Cys hydrogen bond that partially shortcuts the covalent link. For Aor, the proposed intra-protein ET pathway is highlighted in yellow. Structural drawings were performed with PDB structures 1SNR using *Sinorhizobium meliloti* NirK numbering, and 1VLB for Aor using *Desulfovibrio gigas* Aor numbering. The labels FeS1 and FeS2 in Aor correspond to the proximal and distal FeS centers, respectively, relative to the Mo atom position.

Aor is an oxidoreductase with more complex metal cofactors than those of NirK. Aor contains different types of metal ions at the active site and ET centers. The active site, where aldehydes are oxidized, comprises a Mo^{6+} ion coordinated to two oxo, one hydroxo/water (OH_x) and two sulfur ligands, the latter provided from a dithiolene moiety which is part of a pyranopterin cytidine dinucleotide (Figure 1, bottom). This complex molecule, together with two iron-sulfur (FeS) clusters of the [2Fe-2S] type, are the redox centers of Aor and comprise the ET pathway (Romao *et al.,* 1995; Rebelo *et al.,* 2001). The FeS1 (or proximal center) is closer to the Mo site ($d_{Mo\text{-}FeS1}$= 16.2 Å) and is buried inside the protein in a domain inaccessible to solvent. The FeS2 (or distal center) is further away from the Mo site ($d_{Mo\text{-}FeS2}$= 25.6 Å) and close to the protein surface, and it is able to transfer electrons to a flavodoxin, the physiological electron acceptor (Brondino *et al.* 2006, Krippahl *et al.* 2006). Upon aldehyde oxidation at the active site, Mo^{6+} is reduced to Mo^{4+}. The two reducing equivalents are sequentially transferred through the FeS centers to flavodoxin, as shown in Figure 1.

2. A brief description of ET theory

Most biological reactions, mainly those related to cell energy, involve long-range intra- and inter-protein ET, sometimes coupled to proton transfer (Formosinho and Barroso, 2012), between redox centers. A description of ET processes

occurring both in proteins and in small molecules can be made on the basis of Marcus theory (Marcus and Sutin, 1985). The study is relatively straightforward for small molecules. However, modelling ET processes in oxidoreductases, and in all ET proteins, is complicated as it requires to understand all the phenomena that control ET in a protein, e.g. protein dynamics, which may include non-ET processes that tune ET rates (Moser *et al.,* 2010). The Marcus model (equation 1) states that the ET rate (k_{ET}) is governed by the thermodynamic driving force (ΔG^o), the reorganization energy (λ), and the electronic coupling between the reductant (donor, D) and oxidant (acceptor, A) (T_{DA}, also written as H_{DA} or H_{AB})

$$k_{ET} = \frac{4\pi^2}{h\sqrt{4\pi\lambda RT}} T_{DA}^2 e^{-\frac{\left(\Delta G^0 + \lambda\right)^2}{4\lambda RT}} \quad (1)$$

where the remaining symbols have the usual meaning. The simplest representation for T_{DA} states an exponential decay with distance r between D and A (Hopfield, 1974)

$$k_{ET} = k_0 e^{-[\beta(r-r_0)]} e^{-\frac{\left(\Delta G^0 + \lambda\right)^2}{4\lambda RT}} \quad (2)$$

where r_0 is the van der Waals contact distance and k_0 is the maximum ET rate when D and A are in van der Waals contact ($r = r_0$) and $\lambda = -\Delta G°$. Parameter β in equation 2 is the decay factor, which measures the nature of the intervening medium with respect to its efficiency to mediate ET (Page *et al.,* 1999).

When studying inter-protein and/or intra-protein ET processes in oxidoreductases, it is important to determine all the essential parameters involved in equations 1 and 2. This information, together with kinetic, biochemical, and structural data, is necessary to understand in detail how the enzyme works. Experimentally, the value of T_{DA} could be measured by UVvis/NIR spectroscopies using the known Hush formalism for the case where the ET system presents a metal to metal charge transfer reaction, as it occurs in mixed-valence complexes (Creutz, 1983). This is not possible for the systems studied here, since the charge transfer band discussed above for Nir is between the Cu(II) ion and the S-Cys of T1, whereas Aor does not show any charge transfer band. When the enzyme has a redox center that can be independently spectroscopically monitored (UV-vis absorption, Raman, or EPR spectroscopies), the technique of choice to study ET processes is Laser Flash Photolysis (LFP) (formerly Pulse Radiolysis), provided that the process is amenable to light triggering. Performing LFP experiments at different temperatures allows one to least-squares fit equation 1 to the experimental data in order to determine ΔG^o, λ and T_{DA} (Davidson, 1996; Davidson, 2002; Davidson, 2008; Formosinho and Barroso, 2012). Next, equation 2 is fit to the same dataset, but fixing the previously determined parameters ΔG^o and λ. Through this procedure, parameters β and r can be determined. Given the large number of parameters to be determined, this approach applied to complex systems like oxidoreductases may conduct to erroneous interpretations of the intra-protein electron transfer process at molecular level (Davidson, 2002; Formosinho and Barroso, 2012). This fact determines that the characterization of the intraprotein ET pathway in these enzymes must be studied also through other experimental techniques. In the next sections we will discuss other techniques to determine parameters ΔG^o and T_{DA} independently, or at least to estimate their values using electrochemical and spectroscopic tools, and how ET processes in an oxidoreductase can be predicted and studied.

3. Determination of the driving force (ΔG^o) by electrochemical methods

Understanding the oxidoreductase catalytic mechanism and its relationship with the intramolecular ET process requires establishing the reduction potentials of the metal centers situated along the ET pathway, *e.g.* those for T1 and T2 for NirK, and Mo, FeS1, and FeS2 for Aor. As shown in equations 1 and 2, the ET rate (k_{ET}) depends on ΔG^o, which is related to the reduction potentials of the intervening redox centers of the oxidoreductase by

$$\Delta G^0 = -nF\Delta E^0 \quad (3)$$

where n is the number of electrons involved in the reaction and F is the Faraday constant. ΔE^{o}, also known as E_{cell}, is equal to the reduction potential (E^{o}) of oxidant A minus the reduction potential of reductant D. E^{o} is the half-cell potential or half-reaction reduction potential under standard conditions, *i.e.* 298 K, 1 atm, 1 M solutions. For most proteins, it is impossible to work at such concentrations and, therefore, midpoint reduction potentials (E_m or $E^{o'}$) of the redox cofactors are determined. E_m values can be experimentally determined through different electroanalytical methods, such as redox potentiometry and voltamperometry.

E_m values of several redox cofactors in metalloproteins have been determined using voltamperometric techniques like cyclic voltammetry, differential pulsed voltammetry (aka polarography) and square-wave voltammetry. For instance, we have determined the E_m of two physiological redox partners of NirK (*Sinorhizobium meliloti* Paz and *Bradyrhizobium japonicum* CytC) by cyclic voltammetry (Ferroni *et al.,* 2014). The experimental setup for this technique consists of three electrodes (working, reference, and auxiliary) immersed in an electrolyte buffered solution (Figure 2A). The redox protein adsorbed on the working electrode must be capable of exchanging electrons with the solid conducting material used. The applied potential is swept across a given range, and the current is measured. For a thorough explanation of direct electrochemistry of metalloproteins, see Leger *et al.* (Leger and Bertrand, 2008).

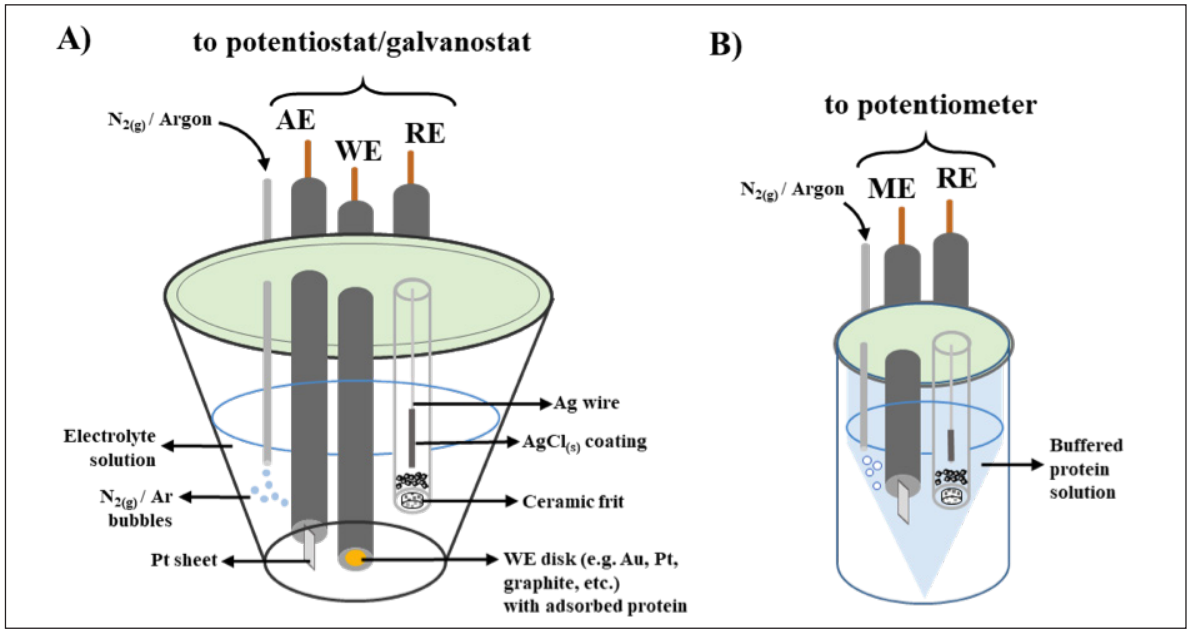

Figure 2. Three- and two-electrode cell setups used for voltamperometric (A) and potentiometric (B) measurements. WE, RE, AE and ME stand for Working, Reference, Auxiliary and Measuring Electrodes, respectively.

Voltamperometric techniques may present some technical problems, such as an inefficient ET between the metalloprotein and the working electrode, which may be overcome by spectropotentiometry. In contrast to voltamperometry, spectropotentiometry is an equilibrium technique in which the oxidoreductase in buffered solution is poised at several potentials by adding reducing (e.g. sodium dithionite or ascorbate) or oxidizing (e.g. potassium ferricyanide or hexachloroiridate) reagents. Solution potential at equilibrium is measured by a setup of two electrodes, comprising a measuring electrode (which must be a noble material like Au or Pt) and a reference electrode ($Ag_{(s)}$/AgCl or $Hg_{(l)}/Hg_2Cl_2$) (Figure 2B)

To understand how spectropotentiometry works, we will consider the simplest redox equilibrium

$$Ox + e^- \rightarrow Red$$

where Ox and Red stand for the oxidized and reduced species, respectively. Let us assume that Ox and/or Red can be quantified by any spectroscopic technique and that the electron involved in the half reaction is provided by a redox partner that is spectroscopically silent or does not interfere in the determination of the Ox/Red fraction.

Considering the Nernst equation for the redox half reaction and that the total concentration of the redox cofactor is [Total] = [Ox] + [Red], obtaining the change in Ox and Red concentration with solution potential (E) is straightforward:

$$[\mathrm{Ox}] = \frac{[\mathrm{Total}]}{1 + e^{\frac{nF}{RT}\left(E - E^{0}\right)}} \qquad (4)$$

To determine the signal intensity of Ox vs. E, a specific spectroscopic feature of the redox center must be monitored by techniques such UV-Vis absorption, EPR, CD, MCD, Fluorescence, NMR, FT-IR and RAMAN. The spectroscopic properties of the redox center (e.g. chromophore, paramagnet, etc.) determine the technique and whether the oxidized or reduced form is measured. We will explain below the UV-vis and EPR monitored potentiometry results we obtained with the two oxidoreductases described in this review.

3.1. UV-vis absorption spectroscopy

UV-vis absorption spectroscopy is one of the most useful and easy to apply (as regards costs and operator training) spectroscopic techniques to monitor redox cofactors. The optical spectra of metalloproteins give information on the electronic structure of redox cofactors, and the technique can also be used to study the absorbance of a specific chromophore as a function of a physicochemical variable such as concentration, pH, E, etc.

For potentiometric titrations monitored by UV-vis spectroscopy, the intensity of an absorption band or peak is related to the species concentration by the Beer-Lambert law. The common setup for determining the absorbance at different E values involves, as depicted in Figure 3A, an inert atmosphere vessel allowing the simultaneous measurement of E and the absorbance of the protein solution. A single wavelength or the entire absorption spectrum can be recorded at each stable E value. The intensity of a characteristic absorption peak of the redox center of interest can be plotted against E and equation 4 can be fit to the experimental dataset.

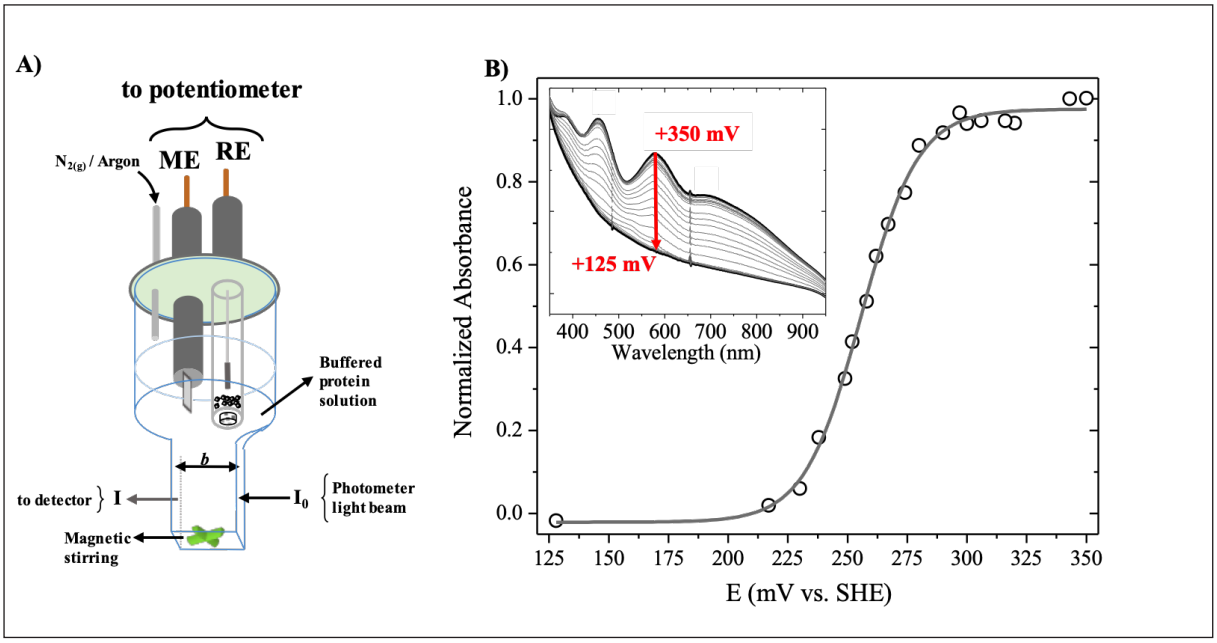

Figure 3. A) modified UV-vis quartz cuvette used for potentiometric titrations. B) Absorbance of NirK oxidized-T1 center at 590 nm as a function of the solution potential. Equation 4 was fit to the data to yield E_m = +250 mV. The inset shows the UV-vis absorption spectra of oxidized T1 of Nir for different potentials.

Panel B in Figure 3 shows a potentiometric titration of NirK monitored by UV-vis spectroscopy. Both the titration and absorbance measurements were simultaneously performed at 298 K and pH 6.0, yielding E_m = +250 mV (vs. SHE). Even though this procedure is useful to determine the T1 reduction potential of NirK, the ET driving force (ΔG^o) can only be calculated knowing both T1 and T2 reduction potentials, which cannot be evaluated by this procedure, as T2 does not present UV-vis absorption bands. The next EPR section will show how to measure both.

3.2. EPR spectroscopy

UV-vis spectroscopy is by far the simplest technique to perform a spectropotentiometric titration, but it cannot be used in cases of very weak or undetectable absorption bands, as is the case of the T2 copper site in NirK and the Mo-cofactor in Aor. Another example of the limitation of this technique is the case of the FeS centers in Aor, which show overlapped broad absorption bands that cannot be discriminated. In these cases, EPR was shown to be the technique of choice. The advantage of EPR is that most important redox active ions of life (Fe, Cu, Mo and W) can generally be well discriminated through their typical EPR signatures and properties, allowing the determination of E_m values by poising the protein solution at several potentials with reducing and/or oxidizing reagents. Furthermore, EPR can provide important information in those systems containing at least two paramagnetic cofactors presenting intercenter magnetic interactions. The EPR signals in the examples below will be used, as in the case of the UV-vis spectra, as a simple fingerprint of the cofactors. Readers interested in understanding more deeply the information that can be obtained from an EPR experiment can read (Rizzi *et al.,* 2016) and references therein.

The T2 center of NirK is paramagnetic in the cupric state and, therefore, can be monitored by EPR spectroscopy. Figure 4 (Top) shows two EPR spectra of NirK. In the as-prepared form, both T1 and T2 are in their oxidized Cu^{2+} state (d^9, spin S= 1/2), giving rise to nearly axial overlapped EPR signals (Spectrum A), which are distinguishable through their hyperfine coupling constant $A_{\parallel}$ ($A_{\parallel}^{T1} < A_{\parallel}^{T2}$). This feature allows simulating each spectrum separately, and also to quantify T1 and T2 concentrations; EPR parameters can be found in (Cristaldi *et al.* 2018). Upon incubation with sodium ascorbate (E ~ 0 mV), T1 becomes EPR silent, as it is reduced to Cu^{1+} (d^{10}, S= 0), whereas a fraction of T2 remains in the Cu^{2+} oxidation state (Figure 4, spectrum B). In contrast, no EPR signals are detected upon addition of a 10-fold molar excess of sodium dithionite under anaerobic conditions (E ~ -660 mV, not shown), indicating that both copper centers are reduced to the cuprous oxidation state. Ferricyanide addition to as-prepared NirK (E ~ +440 mV) does not modify the intensity and line shape of the EPR signal, indicating that both T1 and T2 are fully oxidized in the as-prepared sample (not shown). This relatively simple experiment allows inferring that the T1 reduction potential is higher than that of T2, and that the reduction potentials of both centers fall within the range +440 to 0 mV (Olesen *et al.,* 1998; Pinho *et al.,* 2004). Thus, this approach is useful in those cases where it is not possible to perform an EPR-monitored redox titration, for example because of limitations in sample amount.

In contrast to UV-vis absorption spectroscopy, metal centers EPR signals are recorded at cryogenic temperatures. Therefore, EPR spectroscopy does not allow simultaneously measuring solution potential and recording a spectrum. For this reason, in order to perform an EPR-monitored redox titration, samples of the protein solution poised at different E values at room temperature and under an O_2-free atmosphere, must be withdrawn, frozen to liquid nitrogen temperature, and measured afterwards. Note that, even though EPR measurements are performed at cryogenic temperatures due to experimental reasons, spectra correspond to samples poised at room temperature potential. Figure 4 (bottom) shows a redox potentiometric titration of NirK monitored by CW-EPR, together with the EPR spectra at different potentials in the inset. In this case, the intensity of the EPR signal observed comprises both T1 and T2 signals. A plot of signal intensity (area below integrated spectra) vs. solution potential (E) yielded a double sigmoid curve that was fit to the sum of two one-electron Nernst equations. The E_m values obtained at pH 7.0 were +224 and +108 mV (vs. SHE) for T1 and T2, respectively.

Before going to the EPR analysis of Aor, just a brief explanation regarding the electronic structure of Mo and FeS metal centers. Molybdenum in Aor can be found in three different oxidation states, Mo^{6+}, Mo^{5+}, and Mo^{4+}. Only Mo^{5+} (d^1, S= 1/2) is detectable by EPR and gives rise to signals with all g-values lower than 2. The two [2Fe-2S] centers can be found in two oxidation states. The oxidized state ($[2Fe\text{-}2S]^{2+}$) is EPR silent as it contains two strongly antiferromagnetically coupled Fe^{3+} ions with a ground state with S= 0, which is the only one thermally populated under the EPR experimental conditions. The [2Fe-2S] center becomes paramagnetic on reduction of one of the Fe^{3+} ions to Fe^{2+}. The resulting Fe^{2+}-Fe^{3+} pair ($[2Fe\text{-}2S]^{1+}$) is also strongly antiferromagnetically coupled, but with a S= 1/2 ground state and hence detectable by EPR (Johnson, 1998).

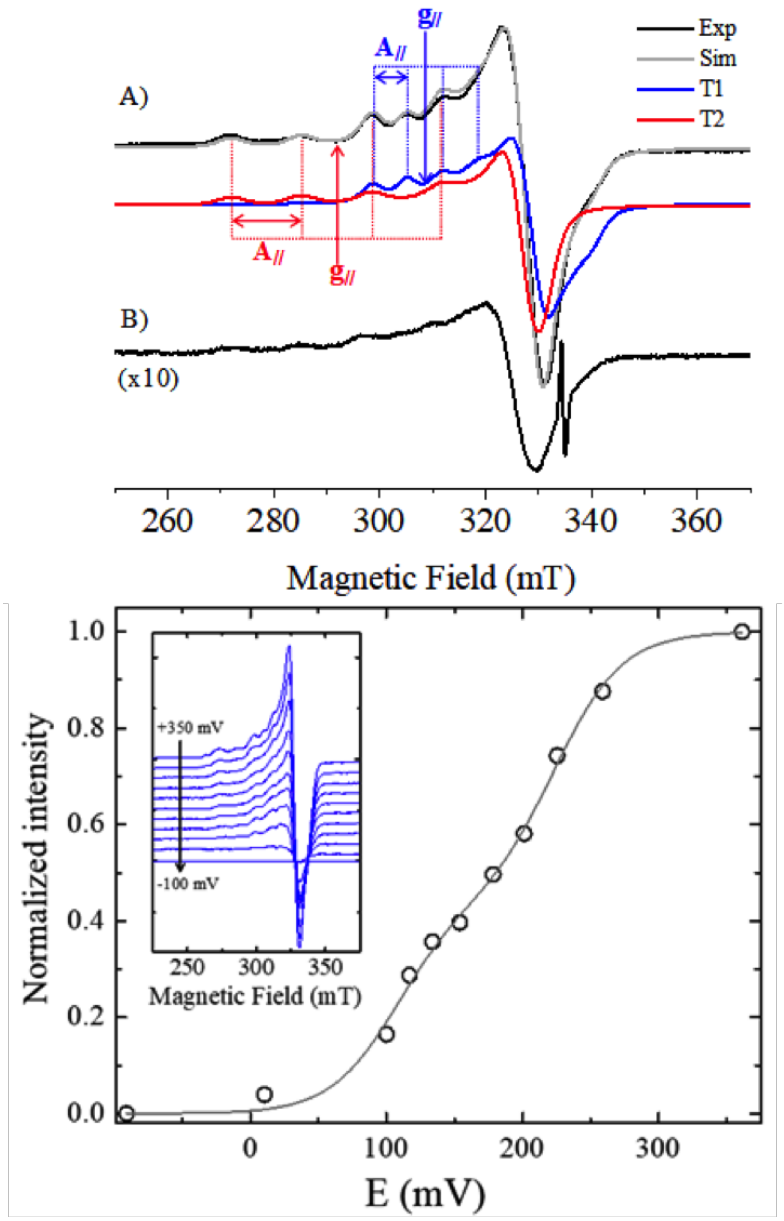

Figure 4. EPR signals (top) in the as-prepared (spectrum A) and ascorbate-reduced form (spectrum B) of NirK. Experimental spectra are in black; simulation of spectrum A is in gray and it was obtained by adding T1 and T2 simulations (blue and red, respectively). The EPR parameters indicated on the figure can be found in (Cristaldi *et al.,* 2018). Redox potentiometric titration of NirK from *S. meliloti* monitored by EPR (bottom). The solid line was obtained by least squares fitting the sum of two-independent Nernst equations with n= 1 to the data. EPR spectra as a function of *E* are shown in the inset. The midpoint reduction potentials obtained were +224 and +108 mV for T1 and T2, respectively (Ferroni *et al.* 2014).

In contrast to NirK, redox cofactors of Aor are EPR-silent in the as-prepared form, and EPR signals are only developed upon dithionite addition under strict anaerobic conditions. Dithionite reduction of Aor for 20 min under anaerobic conditions (E ~ -660 mV vs SHE, reduction for a time lower than 20 min gives rise to a different EPR signal) gives rise to EPR signals associated with the Mo^{5+} ion and the two $[2Fe\text{-}2S]^{1+}$ clusters (Figure 5). Using the same arguments given above in this section for estimating reduction potentials in Cu(II) centers of NirK, we can conclude that metal centers reduction potentials in Aor are below 0 mV (vs. SHE).

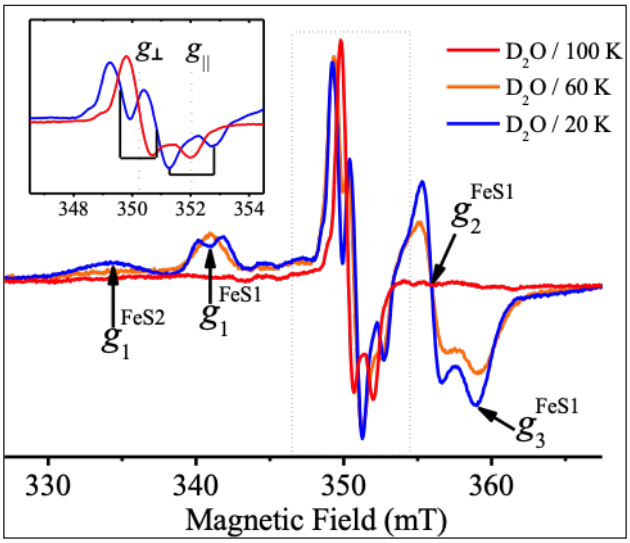

Figure 5. EPR signals of D_2O-exchanged Aor upon dithionite addition at different temperatures. The inset shows the Mo^{5+} signals at 100 K and 20 K. Note the nearly isotropic splitting of Mo^{5+} EPR features at low temperature originated by Mo-proximal FeS center magnetic coupling. EPR parameters indicated on the figure with arrows can be found in (González *et al.,* 2009) and references therein.

The Mo^{5+} signal obtained under these conditions is commonly named "slow-type" in the literature on Mo-enzymes (red and blue spectra in the inset on Figure 5) (Hille, 1996), but hereafter it will be referred to as Mo^{5+} EPR signal. Whereas ~100% of the FeS centers are paramagnetic at this solution potential, only about 10-15% of the total molybdenum is obtained as Mo^{5+} species. This indicates that at this potential, FeS centers were fully reduced to the paramagnetic $[2Fe\text{-}2S]^{1+}$ state, indicating that the E_m values of both FeS centers fall in the range of -450-0 mV (vs SHE). A similar analysis, but with some added complexity, can be performed for Mo. The fact that only 10-15% of Mo^{+5} species are detected by EPR indicates that the E_m values of the +6/+5 and +5/+4 couples fall in the same range, and also that both E_m values are very close.

After analyzing the EPR spectra of the system, *i.e.*, after the distinct EPR signals are identified, the redox titration can be performed. The E_m values of FeS centers can be obtained as explained for NirK. To analyze the E_m values associated with the redox transitions of the Mo cation, the redox equilibriums of both couples should be taken into account, as the redox behavior of Mo species depends on the couples Mo^{6+}/Mo^{5+} and Mo^{5+}/Mo^{4+}. This analysis yielded E_m values of -450 and -530 mV for the $Mo^{6+/5+}$ and $Mo^{5+/4+}$ couples, respectively, for *D. gigas* Aor, and, in addition, it was possible to determine E_m = -280 and -285 mV for FeS1 and FeS2, respectively (Moura *et al.,* 1978).

It should be noted that the ΔE^0 values for the pair T1/T2 obtained for NirK are uphill, *i.e.* in contrast of the electron flow experienced during catalysis. It is not uncommon to obtain such results in metalloproteins, and some explanations have been assayed stating that an uphill step can be compensated for diminishing the DA distance (Moser *et al.,* 2010). In the case of the NirK enzyme studied by us, there is strong evidence that the E_m of the Cu centers are modulated by the interaction of the enzyme with the substrate and the physiological ED during catalysis, giving rise to a downhill ET process ($\Delta E^0 > 0$ mV) (Ferroni *et al.,* 2014).

4. Assignment of the spectroscopically detected metal centers to those observed in the protein structure

The assignment of the spectroscopically detected metal centers to those observed in the X-ray structure is an essential step in characterizing proteins that contain pathways composed of various metal cofactors. This problem is simple in proteins with metal centers showing distinguishable spectroscopic features, *e.g.* the two Cu centers in NirK, where only T1 shows UV-Vis absorption bands (Figure 3B, inset), and T1 and T2 can be easily discriminated by EPR (Figure 4 top).

However, the solution is not trivial for proteins such as Aor, which has two very similar [2Fe-2S] centers. This problem can be solved using different strategies. The most common approach is to generate site-directed variants by molecular biology techniques, changing an amino acid residue that acts as a ligand of the redox cofactor, and then verifying which spectroscopic component was modified. In the case of Aor, the generation of site-directed variants was not possible. Therefore, assignment was based on the analysis of the weak magnetic interaction between Mo and the proximal FeS cluster that splits the Mo^{5+} EPR signal at low temperatures (Figure 5). This involves detecting which FeS (1 or 2) EPR signal is associated with the splitting of the Mo^{5+} spectrum. This can be achieved using EPR by poising an Aor sample at a potential value between the reduction potentials of the FeS centers in order to obtain different populations of reduced (paramagnetic) and oxidized (diamagnetic) FeS centers. This experiment was performed in *D. alaskensis* Aor, which presents more separated E_m values, which is not the case of *D. gigas* Aor. Once that the FeS EPR signal responsible for the Mo^{5+} EPR splitting is identified, the correlation is straightforward, as the Mo^{5+} EPR splitting must be provoked, as said above, by the crystallographically identified proximal FeS center (Figure 1). Thus, it was possible to conclude that the EPR signals identified as FeS1 and FeS2 correspond to the proximal and distal FeS centers of Aor, respectively. A thorough explanation about how this method was performed can be found in references (Andrade *et al.,* 2000; Rizzi *et al.,* 2016). Similar conclusions for Aor, but using an alternative strategy also based on the Mo^{5+} EPR signal splitting provoked by the proximal FeS center, consisted of simulating Mo^{5+} EPR signal splitting as a function of temperature. The dependence of Mo^{5+} splitting on temperature (see Figure 5) is due to the higher relaxation rate of FeS1 in the pair FeS1-Mo^{5+}, a characteristic that is present in all magnetically interacting pairs of spins presenting different relaxation rates. Ideas behind this issue, full experimental data for Aor, as well as the mathematical formalism employed in their analysis can be found in (González *et al.,* 2009) and references therein.

5. Evaluating the integrity of the ET pathway upon inhibition

Enzyme inhibition studies are mandatory to understand enzyme catalytic mechanisms. For oxidoreductases, as for any other class of enzymes, inhibition can be either irreversible or reversible. The latter can be competitive, uncompetitive, or non-competitive. The type of inhibition can be unambiguously determined through in-depth steady state enzyme kinetic studies (Cornish-Bowden 2004). Nevertheless, spectroscopic studies are needed to understand at a molecular level how enzyme inhibition occurs, and to gain insight into catalytic mechanisms. There is no specific methodology to study whether inhibition is due to disruption of the ET pathway. Hence, we will explain specific strategies we followed in our examples to evaluate integrity of the ET pathway upon inhibition.

Aor presents the peculiarity that the active site yields redox inert Mo^{5+} species upon adding enzyme inhibitors such as arsenite, ethylene glycol, and glycerol (Santos-Silva *et al.* 2009). This fact determines that Aor can be obtained in two states, in which Mo is always as Mo^{5+} but the FeS clusters can be either in their diamagnetic (oxidized) or paramagnetic (reduced) states. In other words, the Mo^{5+} species can be measured by EPR in these two enzyme states, one in which the Mo^{5+}-FeS1 coupling is "switched off" (oxidized form, diamagnetic FeS1), and a second where the coupling is "switched on" (reduced form, paramagnetic FeS1) (Boer *et al.,* 2004; Santos-Silva *et al.,* 2009). The experiment consists in measuring the intensity of the Mo^{5+} signal as a function of microwave power to evaluate the degree of saturation of the EPR signal. The higher the microwave power, the higher the probability that the EPR signal attains saturation. Another concept is necessary to understand the saturation EPR experiment. Magnetic coupling of the Mo^{5+} species with a nearby faster relaxing paramagnetic species enhances the relaxation rate of the slow-relaxing species. With these concepts in mind, it is easy to understand the saturation EPR experiment. The reduced sample of inhibited Aor (magnetic interaction "on") requires higher power to reach saturation due to the enhanced relaxation rate of the Mo^{5+} ion induced by the faster relaxing FeS1 center. This fact indicates that the Mo-FeS1 ET pathway can transmit magnetic interaction in the enzyme inhibited form, confirming that the ET pathway is not affected upon inhibition. Details on how to perform this experiment can be found in (Boer *et al.,* 2004; Rizzi *et al.,* 2016).

For NirK, the saturation strategy could not be used due to two simple reasons. First, no T1-T2 magnetic coupling is observable. Second, the two copper centers show similar relaxation rates. Therefore, to evaluate the integrity of the ET pathway in NirK, we exploited the pH dependence of its catalytic activity (Cristaldi *et al.,* 2018). NirK presents maximal activity at pH 5-6 and no activity at pH >8, in which the dependence with pH could be attributed the $N^{\delta 1}H\ldots O{=}C$ hydrogen bond present in the T1-T2 ET pathway (Figure 1). To prove this hypothesis, we performed kinetic studies of *S. meliloti* NirK at pH of maximal and minimal activity using dithionite as electron donor in which the starting and final oxidation states of the copper centers were monitored by UV-Vis and EPR spectroscopies. Both spectroscopies showed that at pH 6 both T1 and T2 center are as Cu^{2+} upon redox cycling the enzyme upon nitrite addition. In contrast, at pH 10 only T2 is reoxidized to Cu^{2+}, which confirms that the lack of activity at high pH may be due to an innefficient/non-existent ET. The conclusion that emerges from this experiment is that the Cys-His covalent pathway (marked in blue in Figure 1) is not

involved in ET since it is pH-independent, suggesting that the ET occurs through the pH-dependent green path in Figure 1. Another methodology used to evaluate ET pathway integrity will be discussed below under section 8.

6. Relation between electronic coupling (T_{DA}) and the isotropic exchange constant J

An application of the Marcus theory is to predict the k_{ET} between two distant redox centers bridged by a chemical pathway (Marcus and Sutin 1985). If the two redox centers are paramagnetic and coupled by isotropic exchange (J), the bridging chemical pathway not only mediates ET, but also transmits isotropic exchange (Calvo *et al.,* 2000) (Note: isotropic exchange, also known as superexchange, is the main Mo-FeS1 interaction that contributes to the splitting of the Mo^{+5} EPR signal, Figure 5; despite it is not magnetic in origin, it is usually regarded as a magnetic interaction). For large distances between spins, the term T_{DA}, which depends on the nature of the chemical pathway bridging two redox centers, is related to the isotropic exchange coupling constant by

$$J \approx -T_{DA}^{2}/U \qquad (8)$$

where U is the difference in energy between the chemical species DA and $D^{+}A^{-}$, with the latter being obtained when one electron is removed from D and transferred to A. Note also that this expression is valid for $T_{DA} << U$. Thus, we can see how the evaluation of J by EPR is related to the term T_{DA} that appears in equation 1.

Aor is a representative example in which the evaluation of J by EPR can be useful to study the factors that govern ET between redox centers in metalloproteins. The catalytic mechanism of Aor involves substrate binding followed by a two-electron oxidation of the Mo^{4+} center once the product is released (Brondino *et al.,* 2006). The structure of as-prepared Aor corresponds to the enzyme in the ready-state and is the starting point of the catalytic cycle (Figure 1, bottom), whereas that of alcohol-inhibited Aor (with the alcohol moiety being bound to the Mo^{5+} ion) resembles a situation where the product of the reaction (the corresponding acid, Figure 1) is formed and remains within bonding distance with the Mo ion (Santos-Silva *et al.,* 2009).

As for the Mo^{5+} EPR signal obtained from the enzyme resting state (Figure 5 and spectrum A in Figure 6), the alcohol-inhibited Aor Mo^{5+} EPR signal is also split by magnetic interaction with the proximal FeS center (Figure 6). The splitting of the EPR lines of glycerol- and ethylene glycol-reacted Aor increases notably relative to that of reduced as-prepared Aor.

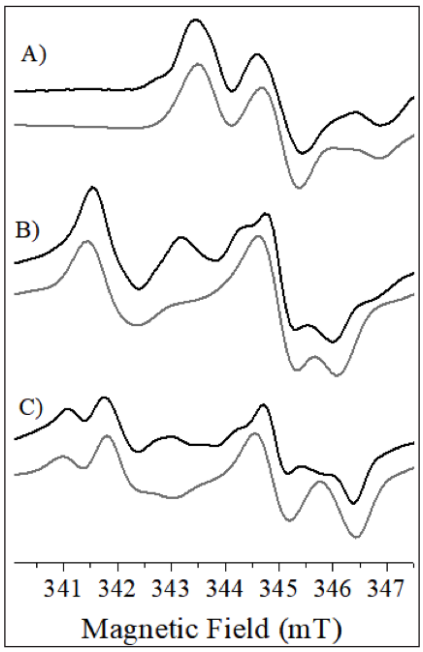

Figure 6. EPR spectra (black) at 20 K for the Mo^{5+} center of reduced as-prepared Aor (spectrum A), and ethylene glycol- and glycerol-reacted Aor (spectra B and C, respectively) with simulations (gray). Simulations yielded $J = -16.6 \times 10^{-4}$ cm^{-1} for as-prepared Aor and $J = -33.3 \times 10^{-4}$ cm^{-1} for ethylene glycol- and glycerol-reacted Aor. Simulation details can be found in reference (Gómez *et al.,* 2015).

The ≈2-fold increase in *J* (*J*-values are in the caption to Figure 6) upon alcohol binding indicates that the capability to transmit isotropic exchange is enhanced, likely due to structural changes in the Mo-FeS1 pathway, or changes in the electronic structure of either Mo^{5+} or FeS1. High resolution structural data of alcohol-inhibited Aor showed no changes associated with the pyranopterin chemical pathway, and the FeS1 EPR signal is identical to that of as-prepared Aor reduced with dithionite (Santos-Silva *et al.,* 2009). Therefore, the increase in *J*-value would indicate changes in the electronic structure of Mo^{5+}, which is a reasonable hypothesis considering the change of Mo^{5+} geometry produced after alcohol binding. This hypothesis was addressed by computational calculations that showed that coordination of the alcohols led to a redistribution of the electronic spin density at Mo^{5+} and its ligands (Gómez *et al.,* 2015). It is important to note that although these studies are not performed during catalysis, they allow one to obtain clues about how ET processes are carried out in these enzymes. For the resting state, calculations showed that part of the spin density is displaced towards the catalytically relevant OH_x ligand, whereas the spin density is displaced towards the dithiolene sulfur ligands of the pterin moiety in the situation that emulates product formation. This fact suggests that this spin density reorganization would raise T_{DA} upon product formation during catalysis, and thus favoring the ET process towards the FeS centers, a process which is required to return the enzyme to the original resting state.

7. Site-directed mutagenesis as a tool in the study of ET pathways

Specific structure-function relationships can be elucidated by site-directed mutagenesis, as this molecular biology tool can be useful to understand how certain amino acid residues of the polypeptide chains modulate ET rates. As an example about how a chemical pathway can be altered by site-directed mutagenesis, the Cys-His ET pathway of *S. meliloti* NirK was modified. As shown in Figure 1, this pathway has two subpaths, one that involves a pure covalent chemical pathway (highlighted in blue) constituted by the protein backbone and the Cys and His side chains, and another one that is a mixed chemical pathway constituted by a His-N^{d1}H…O=C-Cys hydrogen bond that partially shortcuts the T1-T2 bridging covalent link (highlighted in green, Figure 1). We constructed two variants of *S. meliloti* NirK, H171D and C172D (Note: H171D and C172D are two protein variants where the residues histidine 171 and cysteine 172 were changed to aspartic acid), and their kinetic, structural, and spectroscopic properties were compared with those of the wild type enzyme (Cristaldi *et al.,* 2018). The H171D variant (Figure 7) contains both T1 and T2 only connected by the pure covalent subpath and, even though it retains its ability to bind the substrate, it is unable to catalyze nitrite reduction. In contrast, the C172D variant contains two copper sites, one of them being similar to T2Cu in the wild type enzyme. The cysteine variant can reduce nitrite using artificial electron donors, which confirms that, though with less efficiency, the reaction can be conducted entirely at the active site without mediation of the Cys-His ET pathway. From kinetic studies on the wild type enzyme and C172D, it is evident that the involvement of the Cys-His chemical pathway increases enzyme efficiency for catalysis. This is not the case of H171D, where the modification of the ET pathway, more specifically the lack of the His- $N^{\delta1}$H…O=C-Asp hydrogen bond bridge, was suggested to be the cause for the lack of catalytic activity. In summary, site-directed mutagenesis is useful for modifying ET pathways selectively and hence demonstrate the relevance of certain chemical bonds in intra-protein ET. Readers interested in reading about alternative applications of this technique related to ET studies can see reference (Davidson, 2008).

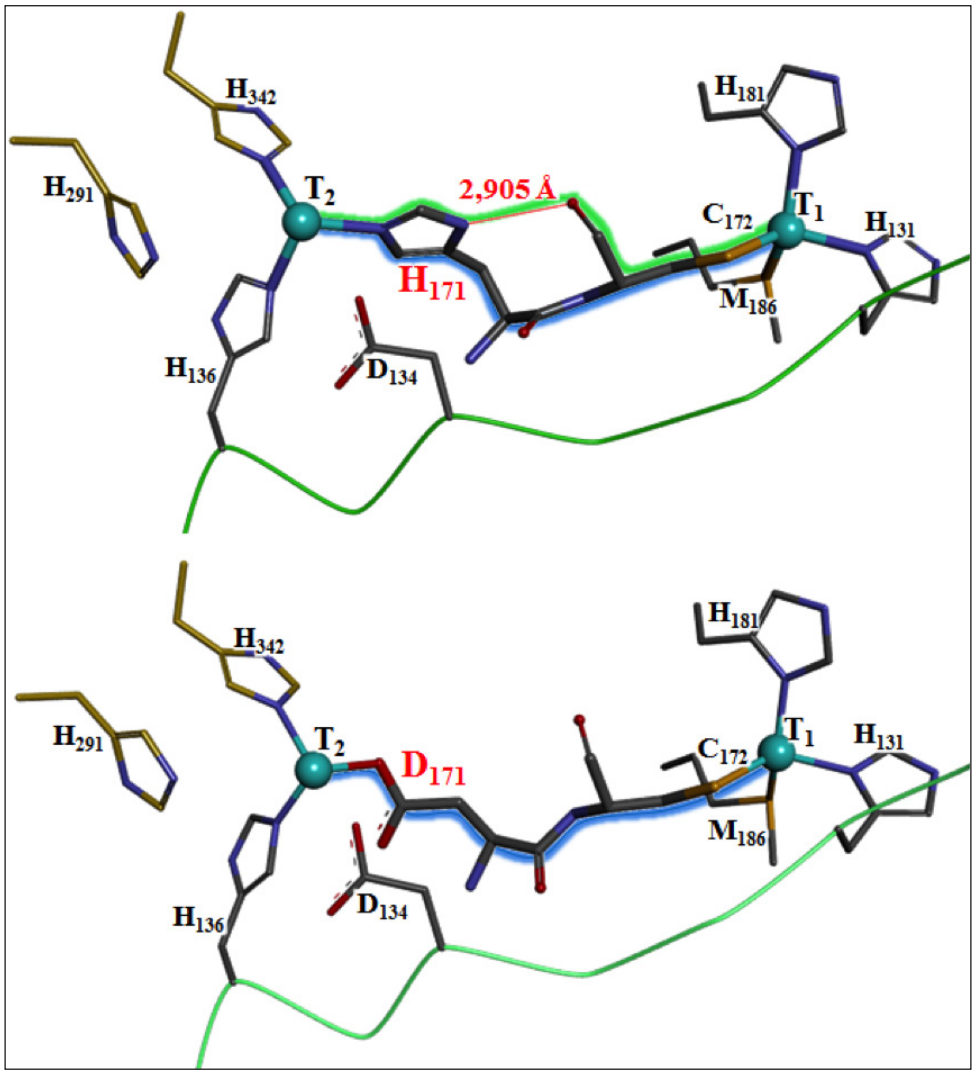

Figure 7. T1-T2 bridging pathways in wild-type *S. meliloti* NirK (top) and H171D variant (bottom) Figures were constructed using the atoms positions obtained from QM/MM calculations (Cristaldi *et al.,* 2018). The $N^{\delta 1}H\ldots O{=}C$ hydrogen bond is depicted in red.

8. X-ray crystallography and its use to unveil potential ET pathways

The ability to get atomic details in three dimensions has demonstrated to be a booster in biological sciences and has helped to understand the chemistry that is carried out at the catalytic active site and/or at the ET pathway of an enzyme or protein complex. The increasing use of X-ray crystallography in macromolecules relies on (i) the relatively large number of synchrotron X-ray sources currently available in the world, (ii) the ability to automate crystallization conditions screening (robotics and *in situ* visualization platforms), (iii) the use of optimized beamlines with efficient single-photon-counting detectors, (iv) automation, (v) user-friendly data-acquisition systems, and (vi) powerful data-processing/analysis packages (Grimes *et al.,* 2018; Muench *et al.,* 2019).

Relevant information from NirK and Aor X-ray structures, such as the identification of putative amino acids involved in the ET mechanism and the putative regions of interaction with external ED, have been obtained in the last years (Nojiri 2017). For NirK, X-ray crystallography has provided all the structural information regarding the catalytic T2 site and its surrounding area, the ways in which T2 and T1 are connected by the His-Cys bridge, the sensing loop, and the identification of second sphere copper coordination ligands relevant in catalysis (Strange *et al.,* 1999; Boulanger *et al.,* 2000; Kataoka *et al.,* 2000). All this information has been valuable in elucidating the catalytic mechanism of nitrite reduction at T2, and the T1-T2 ET process. The roles of Asp^{CAT} and His^{CAT} (Figure 1) as relevant players in the catalytic mechanism of NirK were based on crystallographic structures and the confirmation of their relevance achieved performing NirK variants through site directed mutagenesis. Remarkably, the identification of two Asp^{CAT} conformations, called proximal and gate keeper, led to suppose that this residue accomplishes an essential role in catalysis (Antonyuk

et al., 2005; Horrell *et al.,* 2016). The current hypothesis is that Asp^{CAT} would sense the binding of nitrite at T2 and then, through an unknown mechanism, would trigger the ET from T1 to T2 through the Cys-His pathway (Strange *et al.,* 1999; Cristaldi *et al.,* 2018). Even though X-ray crystallography cannot give in fact any evidence for this ET process, it opens up distinct types of possibilities that merit to be investigated by other techniques. X-ray crystallography in conjunction with EPR has also been essential in characterizing the FeS2-FeS1-Mo ET pathway in *D. gigas* Aor, which is explained above under Sections 5, 6, and 7.

More recently, one particularity of X-ray crystallography, thought to be a weakness of the technique, enlarged its capability. It is well known that X-ray radiation photoreduces metal centers in several cases, though the structures so determined are thought to be those of the oxidized proteins. Particularly, the T1 centers in NirK are prone to photoreduction by X-rays during data collection (Hough *et al.,* 2008). The T2 site of the resting-state enzyme, in contrast, remains unaffected, even at much higher X-ray doses. This fact determines that when a nitrite is bound to T2 in crystals soaked with substrate, the nitrite is converted to nitric oxide during X-ray data collection, indicating that T1-T2 ET is occurring under irradiation. Exploiting these features and using a serial crystallography approach (Horrell *et al.,* 2016), it was possible to obtain a structural movie capturing the conversion of nitrite to nitric oxide and the subsequent return to the enzyme resting state.

Nowadays, genome mining procedures allowed identifying putative novel NirK, with X-ray crystallography being not only the key to unveil their structures but also to predict the involvement of metal cofactors in ET processes. These novel proteins emerged as a new group of NirK which are arranged in a three-domain structure containing, in addition to the two-domain core with T1 and T2 centers, an extra domain with an additional metal cofactor. X-ray crystallographic data confirmed the presence of copper cofactor C-terminus-tethering in NirK from *Thermus scotoductus* SA-01 (Figure 8) (Opperman *et al.,* 2019), an extra heme c group at C-terminus in NirK from *Ralstonia picketii* (Antonyuk *et al.,* 2013), an extra N-terminus cupredoxin domain in the non-self-efficient NirK from *Hypomicrobium denitrificans* (Nojiri *et al.,* 2007), and an extra C-terminus heme c binding domain in NirK from *Pseudoalteromonas haloplanktis* (Tsuda *et al.,* 2013). The copper extra cofactor present in *H. denitrificans* NirK was suggested to be involved in the intra-protein ET pathway (Deligeer *et al.,* 2002; Yamaguchi *et al.,* 2004), but X-ray structural data combined with mutagenesis and kinetic assays using external electron donors refuted that assumption (Nojiri *et al.,* 2007). Even more, the functionality of *R. picketii* NirK and *P. haloplanktis* NirK was solely discussed based on terms of the X-ray structures (Antonyuk *et al.,* 2013; Tsuda *et al.,* 2013), such as intercofactor distances and nature of the chemical pathway linking the putative redox centers. However, additional experiments, as the ones explained in the sections above, are mandatory to confirm these hypotheses based only on X-ray structures.

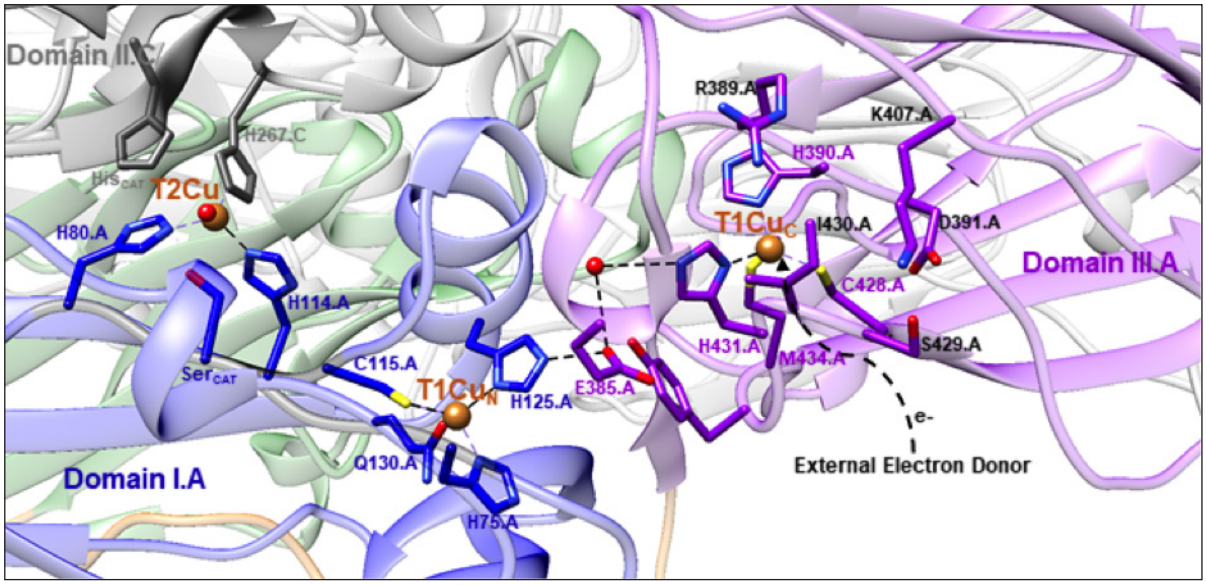

Figure 8. Metal cofactors and putative intraprotein electron transfer pathway in *T. scotoductus* NirK. The ET pathway ED→$T1Cu_C$→$T1Cu_N$→T2Cu is possibly established in 3 segments i) from the external electron donor to the $T1Cu_C$ through a hydrophobic patch surrounded by charged amino acids (residues in purple), ii) from $T1Cu_C$ to $T1Cu_N$ through a water molecule and Glu385 residue, and iii) from $T1Cu_N$ to T2Cu by either Cys-His bridge or the sensing loop.

Conclusions

This paper summarizes the use of various experimental techniques employed in the characterization of electron transfer pathways in oxidoreductases. The examples presented have been selected to show how the combination of molecular biology, spectroscopic, electrochemical, and structural techniques can be used to characterize the chemical pathways for electron transfer process in redox enzymes and electron transfer proteins. Although the methodologies used to study these types of systems are rather different, we present in this paper a unified view of the problem to show the multidisciplinary experimental approach of the subject.

It is clear that UV-vis and EPR in conjunction with other spectroscopies not discussed here are valuable tools to study not only the geometric and electronic structure of individual paramagnetic transition metal ions, but also to evaluate ΔG^{o} required in all long-distance electron transfer reactions. The biggest advantage of the spectropotentiometric techniques relative to those based on voltamperometry is that, in general, with just one technique one could discriminate all the redox active species present in an electron transfer pathway. The measurement of exact values for T_{DA} in an independent manner is more complicated in these oxidoreductases. For those systems presenting paramagnetic redox centers coupled by isotropic exchange, it is evident that the information relative to the T_{DA} term provided by EPR is very valuable, as not only the ability of a chemical pathway to mediate electron transfer can be inferred, but also the order of magnitude of T_{DA} can be estimated. However, this "paramagnetic redox centers coupled by exchange" characteristic is not present in all electron transfer systems, and therefore additional experimental approaches have to be implemented. Among them, structural techniques can provide the starting information as potential electron transfer pathways can be envisaged, but evidently these hypothetical conclusions must be proved with other techniques. Under this context, site directed mutagenesis studies appear as one of the election techniques, since the construction of specifically designed protein variants, whose kinetic properties can be measured in comparison with those of the wild type enzymes, constitutes in our opinion a powerful method that complements structural X-ray and spectroscopic data. Evidently, the information that can be obtained with all these methodologies is in most cases either qualitative or semiquantitative at the most, as they are not oriented to measure the k_{ET} specifically. However, the information gathered from all the experimental techniques presented here is mandatory to fully understand at a molecular level electron transfer processes in redox enzymes.

Acknowledgments

We thank FONCyT, CONICET, and CAI+D-UNL for financial support. M.G.R. P.J.G, F.M.F., and C.D.B are members of CONICET (Argentina).

References

[1] S. L. Andrade, C. D. Brondino, M. J. Feio, I. Moura and J. J. Moura. Aldehyde oxidoreductase activity in *Desulfovibrio alaskensis* NCIMB 13491 EPR assignment of the proximal [2Fe-2S] cluster to the Mo site. *Eur. J. Biochem.*, 267(7): 2054-2061, 2000.

[2] C. Andreini, I. Bertini, G. Cavallaro, G. Holliday and J. Thornton. Metal ions in biological catalysis: from enzyme databases to general principles. *J Biol Inorg Chem*, 13(8): 1205-1218, 2008.

[3] S. V. Antonyuk, H. Cong, R. R. Eady and S. S. Hasnain. Structures of Protein-Protein Complexes involved in electron transfer. *Nature*, 496(7443): 123-126, 2013.

[4] S. V. Antonyuk, R. W. Strange, G. Sawers, R. R. Eady and S. S. Hasnain. Atomic resolution structures of resting-state, substrate- and product-complexed Cu-nitrite reductase provide insight into catalytic mechanism. *Proc. Natl. Acad. Sci. U.S.A.*, 102(34): 12041, 2005.

[5] J. M. Berg, J. L. Tymoczko, L. Stryer and G. J. Gatto. *Biochemistry*. W. H. Freeman and Company, New York, USA, 2012.

[6] D. R. Boer, A. Thapper, C. D. Brondino, M. J. Romao and J. J. Moura. X-ray crystal structure and EPR spectra of "arsenite-inhibited" *Desulfo vibrio* aldehyde dehydrogenase: a member of the xanthine oxidase family. *J. Am. Chem. Soc.*, 126(28): 8614-8615, 2004.

[7] M. J. Boulanger, M. Kukimoto, M. Nishiyama, S. Horinouchi and M. E. P. Murphy. Catalytic Roles for Two Water Bridged Residues (Asp-98 and His-255) in the Active Site of Copper-containing Nitrite Reductase. *J. Biol. Chem.*,

275(31): 23957-23964, 2000.

[8] C. D. Brondino, M. G. Rivas, M. J. Romao, J. J. Moura and I. Moura. Structural and electron paramagnetic resonance (EPR) studies of mononuclear molybdenum enzymes from sulfate-reducing bacteria. *Acc. Chem. Res.*, 39(10): 788-796, 2006.

[9] R. Calvo, E. C. Abresch, R. Bittl, G. Feher, W. Hofbauer, R. A. Isaacson, W. Lubitz, M. Y. Okamura and M. L. Paddock. EPR Study of the Molecular and Electronic Structure of the Semiquinone Biradical QA-•QB-• in Photosynthetic Reaction Centers from Rhodobacter sphaeroides. *J. Am. Chem. Soc.*, 122(30): 7327-7341, 2000.

[10] A. Cornish-Bowden. *Fundamentals of enzyme kinetics*. Portland, London, 2004.

[11] C. Creutz. Mixed Valence Complexes of d5-d6 Metal Centers. In *Progress in Inorganic Chemistry*. John Wiley and Sons, Inc, 1983.

[12] J. C. Cristaldi, M. C. Gomez, P. J. Gonzalez, F. M. Ferroni, S. D. Dalosto, A. C. Rizzi, M. G. Rivas and C. D. Brondino. Study of the Cys-His bridge electron transfer pathway in a copper-containing nitrite reductase by site-directed mutagenesis, spectroscopic, and computational methods. *Biochim. Biophys. Acta Gen. Subj.*, 1862(3): 752-760, 2018.

[13] V. L. Davidson. Unraveling the kinetic complexity of interprotein electron transfer reactions. *Biochemistry*, 35(45): 14035-14039, 1996.

[14] V. L. Davidson. Chemically gated electron transfer. A means of accelerating and regulating rates of biological electron transfer. *Biochemistry*, 41(50): 14633-14636, 2002.

[15] V. L. Davidson. Protein control of true, gated, and coupled electron transfer reactions. *Acc. Chem. Res.*, 41(6): 730-738, 2008.

[16] Deligeer, R. Fukunaga, K. Kataoka, K. Yamaguchi, K. Kobayashi, S. Tagawa and S. Suzuki. Spectroscopic and functional characterization of Cu-containing nitrite reductase from *Hyphomicrobium denitrificans* A3151. *J. Inorg. Biochem.*, 91(1): 132-138, 2002.

[17] F. Ferroni, J. Marangon, N. Neuman, J. Cristaldi, S. Brambilla, S. Guerrero, M. Rivas, A. Rizzi and C. Brondino. Pseudoazurin from *Sinorhizobium meliloti* as an electron donor to copper-containing nitrite reductase: influence of the redox partner on the reduction potentials of the enzyme copper centers. *J Biol Inorg Chem*, 19(6): 913-921, 2014.

[18] S. Formosinho and M. Barroso. *Proton-Coupled Electron Transfer: A Carrefour of Chemical Reactivity Traditions*. The Royal Society of Chemistry, Cambridge, 2012.

[19] Y. Fukuda, K. M. Tse, T. Nakane, T. Nakatsu, M. Suzuki, M. Sugahara, S. Inoue, T. Masuda, F. Yumoto, N. Matsugaki, E. Nango, K. Tono, Y. Joti, T. Kameshima, C. Song, T. Hatsui, M. Yabashi, O. Nureki, M. E. P. Murphy, T. Inoue, S. Iwata and E. Mizohata. Redox-coupled proton transfer mechanism in nitrite reductase revealed by femtosecond crystallography. *Proc. Natl. Acad. Sci. U.S.A.*, 113(11): 2928-2933, 2016.

[20] M. Gómez, N. Neuman, S. Dalosto, P. González, J. G. Moura, A. Rizzi and C. Brondino. Isotropic Exchange Interaction between Mo and the Proximal FeS Center in the Xanthine Oxidase Family Member Aldehyde Oxidoreductase from *Desulfovibrio gigas* on Native and Polyalcohol Inhibited Samples: An EPR and QM/MM Study. *J Biol Inorg Chem*, 20(2): 233-242, 2015.

[21] P. J. González, G. I. Barrera, A. C. Rizzi, J. J. G. Moura, M. C. G. Passeggi and C. D. Brondino. EPR studies of the Mo-enzyme aldehyde oxidoreductase from *Desulfovibrio gigas*: An application of the Bloch-Wangsness-Redfield theory to a system containing weakly-coupled paramagnetic redox centers with different relaxation rates. *J. Inorg. Biochem.*, 103(10): 1342-1346, 2009.

[22] J. M. Grimes, D. R. Hall, A. W. Ashton, G. Evans, R. L. Owen, A. Wagner, K. E. McAuley, F. von Delft, A. M. Orville, T. Sorensen, M. A. Walsh, H. M. Ginn and D. I. Stuart. Where is crystallography going? *Acta Crystallogr. D*, 74(2): 152-166, 2018.

[23] R. G. Hadt, S. I. Gorelsky and E. I. Solomon. Anisotropic covalency contributions to superexchange pathways in type one copper active sites. *J. Am. Chem. Soc.*, 136(42): 15034-15045, 2014.

[24] R. Hille. The Mononuclear Molybdenum Enzymes. *Chem. Rev.*, 96(7): 2757-2816, 1996.

[25] J. J. Hopfield. Electron transfer between biological molecules by thermally activated tunneling. *Proc. Natl. Acad. Sci. U S A*, 71(9): 3640-3644, 1974.

[26] S. Horrell, S. V. Antonyuk, R. R. Eady, S. S. Hasnain, M. A. Hough and R. W. Strange. Serial crystallography captures enzyme catalysis in copper nitrite reductase at atomic resolution from one crystal. *IUCrJ*, 3(4): 271-281, 2016.

[27] M. A. Hough, R. R. Eady and S. S. Hasnain. Identification of the Proton Channel to the Active Site Type 2 Cu Center of Nitrite Reductase: Structural and Enzymatic Properties of the His254Phe and Asn90Ser Mutants. *Biochemistry*, 47(51): 13547-13553, 2008.

[28] M. K. Johnson. Iron-sulfur proteins: new roles for old clusters. *Curr. Opin. Chem. Biol.*, 2(2): 173-181, 1998.

[29] K. Kataoka, H. Furusawa, K. Takagi, K. Yamaguchi and S. Suzuki. Functional Analysis of Conserved Aspartate and Histidine Residues Located Around the Type 2 Copper Site of Copper-Containing nitrite reductase. *J. Biochem.*, 127(2): 345-350, 2000.

[30] L. Krippahl, P. N. Palma, I. Moura and J. J. G. Moura. Modelling the electron-transfer complex between aldehyde oxidoreductase and flavodoxin. *Eur. J. Inorg. Chem.*(19): 3835-3840, 2006.

[31] C. Leger and P. Bertrand. Direct electrochemistry of redox enzymes as a tool for mechanistic studies. *Chem. Rev.*, 108(7): 2379-2438, 2008.

[32] R. A. Marcus and N. Sutin. Electron transfers in chemistry and biology. *Biochim. Biophys. Acta- Reviews on Bioenergetics*, 811(3): 265-322, 1985.

33] C. C. Moser, J. L. Anderson and P. L. Dutton. Guidelines for tunneling in enzymes. *Biochim. Biophys. Acta*, 1797(9): 1573-1586, 2010.

[34] J. J. Moura, A. V. Xavier, R. Cammack, D. O. Hall, M. Bruschi and J. Le Gall. Oxidation-reduction studies of the Mo-(2Fe-2S) protein from *Desulfovibrio gigas*. *Biochem. J.*, 173(2): 419-425, 1978.

[35] S. P. Muench, S. V. Antonyuk and S. S. Hasnain. The expanding toolkit for structural biology: synchrotrons, X-ray lasers and cryoEM. *IUCrJ*, 6(2): 167-177, 2019.

[36] M. Nojiri. Structure and Function of Copper Nitrite Reductase. In *Metalloenzymes in Denitrification: Applications and Environmental Impacts*. The Royal Society of Chemistry, Cambridge, 2017.

[37] M. Nojiri, Y. Xie, T. Inoue, T. Yamamoto, H. Matsumura, K. Kataoka, Deligeer, K. Yamaguchi, Y. Kai and S. Suzuki. Structure and function of a hexameric copper-containing nitrite reductase. *Proc. Natl. Acad. Sci. U.S.A.*, 104(11): 4315-4320, 2007.

[38] K. Olesen, A. Veselov, Y. Zhao, Y. Wang, B. Danner, C. P. Scholes and J. P. Shapleigh. Spectroscopic, Kinetic, and Electrochemical Characterization of Heterologously Expressed Wild-Type and Mutant Forms of Copper-Containing Nitrite Reductase from *Rhodobacter sphaeroides* 2.4.3†. *Biochemistry*, 37(17): 6086-6094, 1998.

[39] D. J. Opperman, D. H. Murgida, S. D. Dalosto, C. D. Brondino and F. M. Ferroni. A three-domain copper-nitrite reductase with a unique sensing loop. *IUCrJ*, 6(2): 248-258, 2019.

[40] C. C. Page, C. C. Moser, X. Chen and P. L. Dutton. Natural engineering principles of electron tunnelling in biological oxidation-reduction. *Nature*, 402(6757): 47-52, 1999.

[41] D. Pinho, S. Besson, C. D. Brondino, B. de Castro and I. Moura. Copper-containing nitrite reductase from *Pseudomonas chlororaphis* DSM 50135. *Eur. J. Biochem.*, 271(12): 2361-2369, 2004.

[42] J. M. Rebelo, J. M. Dias, R. Huber, J. J. Moura and M. J. Romao. Structure refinement of the aldehyde oxidoreductase from *Desulfovibrio gigas* (MOP) at 1.28 A. *J Biol Inorg Chem*, 6(8): 791-800, 2001.

[43] A. C. Rizzi, P. J. Gonzalez, N. Neuman and C. D. Brondino. EPR as a Tool for Study of Isolated and Coupled Paramagnetic Centers in Coordination Compounds and Macromolecules of Biological Interest. *Eur. J. Inorg. Chem.*, 2016(2): 192-207, 2016.

[44] M. J. Romao, M. Archer, I. Moura, J. J. Moura, J. LeGall, R. Engh, M. Schneider, P. Hof and R. Huber. Crystal structure of the xanthine oxidase-related aldehyde oxido-reductase from *D. gigas*. *Science*, 270(5239): 1170-1176, 1995.

[45] T. Santos-Silva, F. Ferroni, A. Thapper, J. Marangon, P. J. González, A. C. Rizzi, I. Moura, J. J. G. Moura, M. J. Romão and C. D. Brondino. Kinetic, structural, and EPR studies reveal that aldehyde oxidoreductase from *Desulfovibrio gigas* does not need a sulfido ligand for catalysis and give evidence for a direct Mo-C interaction in a biological system. *J. Am. Chem. Soc.*, 131(23): 7990-7998, 2009.

[46] J. J. R. F. d. Silva and R. J. P. Williams. *The biological chemistry of the elements : the inorganic chemistry of life*. Clarendon Press, Oxford, 1991.

[47] R. W. Strange, L. M. Murphy, F. E. Dodd, Z. H. L. Abraham, R. R. Eady, B. E. Smith and S. S. Hasnain. Structural and kinetic evidence for an ordered mechanism of copper nitrite reductase. *J. Mol. Biol.* , 287(5): 1001-1009, 1999.

[48] S. Suzuki, T. Kohzuma, Deligeer, K. Yamaguchi, N. Nakamura, S. Shidara, K. Kobayashi and S. Tagawa. Pulse Radiolysis Studies on Nitrite Reductase from *Achromobacter cycloclastes* IAM 1013: Evidence for Intramolecular Electron Transfer from Type 1 Cu to Type 2 Cu. *J. Am. Chem. Soc.*, 116(24): 11145-11146, 1994.

[49] A. Tsuda, R. Ishikawa, H. Koteishi, K. Tange, Y. Fukuda, K. Kobayashi, T. Inoue and M. Nojiri. Structural and mechanistic insights into the electron flow through protein for cytochrome c-tethering copper nitrite reductase. *J. Biochem.*, 154(1): 51-60, 2013.

[50] K. Yamaguchi, K. Kataoka, M. Kobayashi, K. Itoh, A. Fukui and S. Suzuki. Characterization of Two Type 1 Cu Sites of *Hyphomicrobium denitrificans* Nitrite Reductase: A New Class of Copper-Containing Nitrite Reductases. *Biochemistry*, 43(44): 14180-14188, 2004.

Bios

María Gabriela Rivas

María Gabriela Rivas received her B.Sc. degree in Biotechnology from Universidad Nacional del Litoral (Argentina), followed by a Ph.D. in Biophysical Chemistry from the Department of Chemistry at the Faculdade de Ciências e Tecnologia of Universidade Nova de Lisboa (Portugal). From 2007 to 2009, she was a postdoctoral fellow at REQUIMTE (Portugal) and CNRS (France). Since 2013, she is a research scientist for CONICET and a professor at the Department of Physics of the School of Biochemistry and Biological Sciences of Universidad Nacional del Litoral (Argentina). Her main research interest is the study of molecular mechanisms for Mo and W-uptake in bacteria.

Pablo J. González

Pablo J. González received his diploma in Biotechnology from Universidad Nacional del Litoral in 2002. In 2006, he obtained his Ph.D. degree in Biophysical Chemistry from the Department of Chemistry at the Faculdade de Ciências e Tecnologia of Universidade Nova de Lisboa (Portugal). He had postdoctoral training in biophysical techniques applied to the study of metalloproteins before joining as a research scientist for REQUIMTE at FCT-UNL in Portugal. He is currently a professor at the Department of Physics and a research scientist for CONICET at the School of Biochemistry and Biological Sciences of Universidad Nacional del Litoral, Argentina.

Felix M Ferroni

Felix M Ferroni was born in San Pedro (Bs. As.), Argentina, in 1979. He obtained his degree in Biotechnology with highest honors in 2005, followed by a PhD in Biological Sciences in 2010, both at Universidad Nacional del Litoral, Argentina. He continued his career with a postdoc at CONICET (2010-2012) and a postdoc in biocatalysis and protein crystallography (2013-2015) at University of The Free State (South Africa). He is currently an Assistant Researcher for CONICET; his main research interest is the study of enzymes with cupredoxin-domains from extremophiles and soil bacteria with biocatalytic, crystallographic, electrochemical and biosesing purposes.

Alberto C. Rizzi

Alberto C. Rizzi received B.Sc. and Ph.D. degrees from Universidad Nacional del Litoral (Argentina) and was a postdoctoral fellow at Max Planck Institute for Bioinorganic Chemistry (Germany). He is now associate professor at the Department of Physics of the School of Biochemistry and Biological Sciences at Universidad Nacional del Litoral. His research interests include the role of transition metals ions in biology and the study of bioinorganic systems as models for complex biological compounds using Electronic Paramagnetic Resonance (EPR) and magnetic measurements.

Carlos D. Brondino

Carlos D. Brondino received his B.Sc. and Ph.D. degrees from Universidad Nacional del Litoral (Argentina). He was a postdoctoral and research fellow at the Department of Chemistry of Universidade Nova de Lisboa, Portugal. He is now a full professor, head of Department, and a research fellow for CONICET at the Department of Physics of the School of Biochemistry and Biological Sciences of Universidad Nacional del Litoral. His main research interests include the reaction mechanism of metalloenzymes involved in the biological cycles of nitrogen and sulfur, and the development of EPR-based methodologies to characterize the magnetic properties of paramagnetic systems of biological interest.

Science Reviews
from the end of the world

Vol. 1, No.2, March 2020 // pp. 25-44 /

The Nature of Charge-Transfer Excited States in Transition Metal Complexes Pertinent to Energy Conversion and Chemical Sensing

Néstor E. Katz

INQUINOA (UNT-CONICET), Facultad de Bioquímica, Química y Farmacia, Universidad Nacional de Tucumán, San Miguel de Tucumán, Argentina.
Email: nkatz@fbqf.unt.edu.ar

Abstract

We present procedures for determining the nature of charge-transfer excited states in transition metal complexes relevant to energy conversion and chemical sensing processes. In particular, we analyze the importance of resorting to both spectroelectrochemical and photophysical techniques to elucidate the "fingerprints" of the intermediates involved in the fate of these reactions. Our contributions to the subject are discussed.

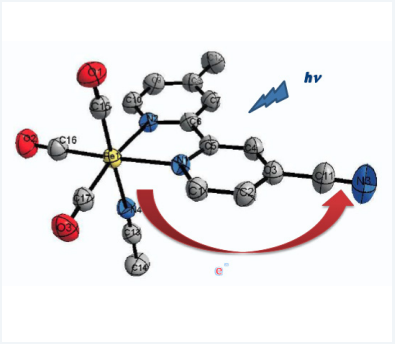

Keywords:
transition metal complexes, energy conversion, chemical sensing

Introduction

Inspired by the central role of transition metal complexes in natural processes that are fundamental to life on Earth, such as photosynthesis and respiration, inorganic chemists have long recognized that determining the nature of certain charge-transfer excited states can eventually lead to successful conversion of solar energy into electrical or chemical energy as well as to development of new sensing methods for medicinal purposes.

The importance of combining spectroelectrochemical techniques (reaction-oriented electrochemistry with species-focused spectroscopy) to analyze redox reactions in general has already been discussed by Kaim *et al.*[1] These results can be combined with photophysical techniques in order to identify intermediates involved in electron transfer processes that are relevant to the design of energy conversion schemes or to the discovery of new medical diagnosis and therapies. As a typical example, in a recent work by Keane *et al.*[2], the reaction mechanisms involved in the photo-oxidation of guanine in DNA by a Ru complex containing tetraazaphenanthrene ligands were explained by comparing the results obtained by UV-Vis and mid-IR spectroelectrochemical experiments with picosecond transient absorption and time-resolved IR experiments of the mentioned Ru complex bound to DNA.

In our group at INQUINOA (Institute of Chemistry of the Northwest of Argentina), located close to the end of the world, we have been interested since the 1990s in the synthesis and physicochemical characterization of new ruthenium and rhenium complexes that can be applied as photosensitizers in artificial photosynthesis or as sensors of biologically relevant analytes. We have resorted to **both** spectroelectrochemical and photophysical techniques to elucidate the "fingerprints" of the main intermediates involved in the evolution of charge-transfer processes in which these complexes are involved. This article focuses particularly on our contributions to this field.

1. Photosensitizers

We have recently reported[3] the synthesis and physicochemical properties of new ruthenium polypyridyl complexes of formulae $[Ru(bpy)_{3-x}(Mebpy\text{-}CN)_x](PF_6)_2$, (bpy = 2,2′-bipyridine, Mebpy-CN = 4-methyl-2,2′-bipyridine-4′-carbonitrile, x = 1 (**1**), 2 (**2**), 3 (**3**)) with the aim of applying them as photosensitizers onto ZnO nanowires. Cation structures in **1**-**3** are shown in Scheme 1. These complexes have nitrile groups in the periphery of the polypyridyl ligands, which can be used as anchoring entities to ZnO while preserving the integrity of the nanowires. Following a previous work by McCusker *et al.*[4], who reported a considerable increase in the lifetimes of excited states of Ru bipyridyl complexes by adding electron-withdrawing substituents such as nitrile groups in the 4,4´- positions of the bipyridyl rings, we could not only demonstrate that the photosensitizing properties of complexes **1**-**3** improve with increasing substitution of bpy by Mebpy-CN, but also design new solar cells that convert light into electrical energy by using TiO_2 or ZnO as semiconductors sensitized by these Ru species.

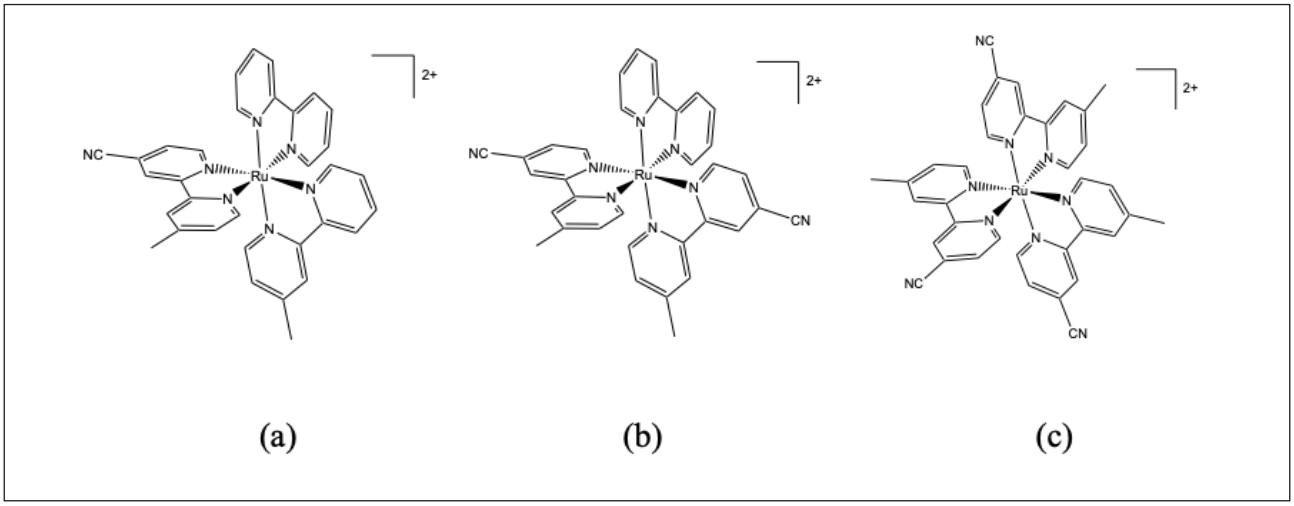

Scheme 1. Cation structures in complexes **1** (a), **2** (b) and **3** (c).

Spectroelectrochemical studies were carried out on complexes **1** - **3** in order to know the nature of the oxidized and reduced species. As shown in Figure 1(a), bleaching of the MLCT (metal-to-ligand charge transfer) bands at λ_{max} = 450-470 nm is observed when oxidizing the metallic center. New IL (intraligand) bands appear at λ_{max} = 330 nm with intensities increasing along the series. After reducing Mebpy-CN, as shown in Figure 1(b), new bands appear at λ_{max} = 350 nm, which are typical of bpy radicals.[5] These data can be compared to the photophysical properties of transient species that are described in the next paragraph. All the studied complexes exhibited an almost complete recovery of the initial spectra when re-oxidized or re-reduced.

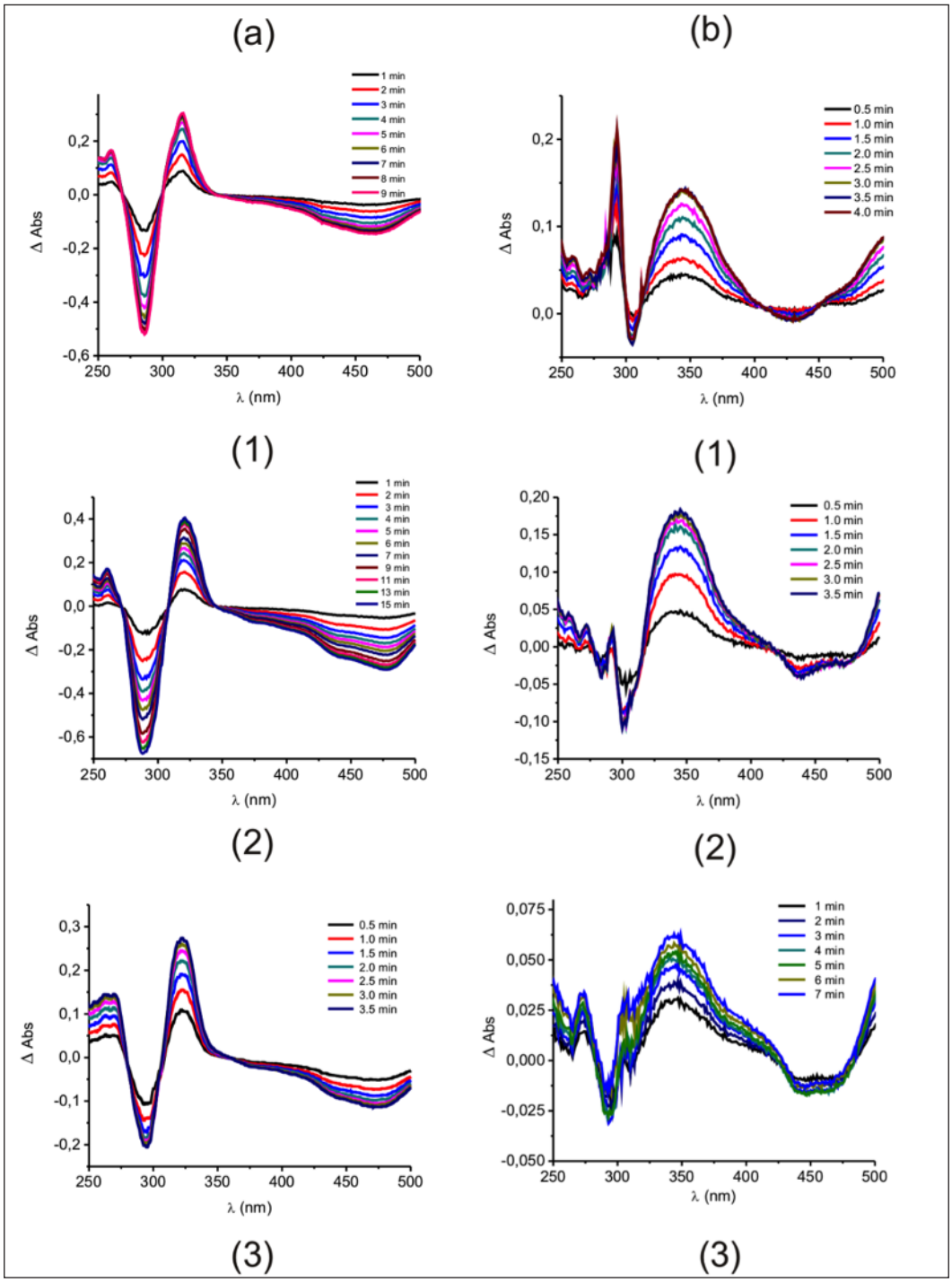

Figure 1. (a) Oxidative difference spectra acquired at an applied potential 150 mV higher than the oxidation potential of the metallic center of **1**, **2** and **3**, from top to bottom, respectively. (b) Reductive difference spectra acquired at an applied potential 75 mV lower than the first reduction potential of **1**, **2** and **3**, from top to bottom, respectively.

The photophysical properties of complexes **1-3** in CH_3CN at room temperature are summarized in Table 1. They all exhibit higher emission quantum yields (φ_{em}) and higher lifetimes (τ) for the lowest ^{3}MLCT excited states than those of prototype complex $[Ru(bpy)_3](PF_6)_2$, measured under the same conditions (φ_{em} = 0.095 and τ = 0.66 μs, respectively). Both values increase with increasing substitution of bpy by Mebpy-CN, indicating a higher delocalization induced by the nitrile groups, as described before by McCusker *et al*.[4] for the 4,4´-disubstituted bipyridyl species. The correlation between luminescence quantum yields and emission lifetimes has already been reported in a different series of ruthenium(II) polypyridyl complexes.[6]

Table 1. Photophysical properties of complexes **1-3** in CH_3CN, at r.t. (room temperature).

Complex	λ_{em} (nm)	φ_{em}	τ / μs [a]	k_{obs}x10^{-5}/ s^{-1}	k_rx10^{-5}/ s^{-1} [b]	k_{nr}x10^{-5}/ s^{-1} [c]
1	623	0.120	0.76 (0.73)	13.2	1.58	11.6
2	660	0.125	0.97 (1.09)	10.3	1.28	9.0
3	658	0.133	1.16 (1.22)	8.6	1.14	7.5

[a] Data obtained by LFP (in parentheses, by TCSPC). [b] $k_r = \varphi^{em} \cdot k_{obs}$. [c] $k_{nr} = k_{obs} - k_r$.

Figure 2 shows the time-resolved differential absorption spectra of complexes **1-3** obtained by LFP (laser flash photolysis), a powerful technique used to detect intermediates in light-induced processes. In all cases, bleaching of the MLCT bands at λ_{max} = 450-470 nm was observed, which can be explained by the presence of Ru^{III} in the excited state. Additionally, new bands appear at λ_{max} = 370 nm, assigned to IL transitions of the Mebpy-CN· radical, and at λ_{max} = 330 nm, associated to IL bands of the neutral ligands. As shown in Table 1, the lifetimes obtained by LFP agree, within experimental error, with those obtained by TCSPC (time-correlated single photon counting), another important photophysical technique used for determining a wide range of lifetimes of excited states in luminescent compounds.

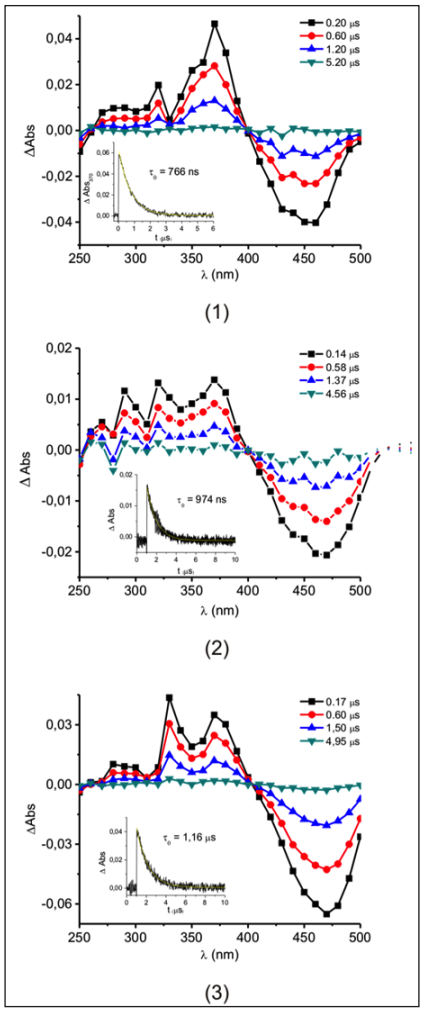

Figure 2. Time-resolved differential absorption spectra of **1** (top), **2** (middle) and **3** (bottom) in CH_3CN at different times (0.14 - 5.20 μs), λ_{exc} = 370 nm, obtained by LFP. Insets: absorbance decays at 370 nm and mono-exponential fittings.

The spectroelectrochemical measurements described before are consistent with these findings: a new band appears at λ_{max} = 350 nm when the complexes are reduced (displaced by charge effects in relation to the band at λ_{max} = 370 nm observed in LFP) and a new band appears at λ_{max} = 330 nm when the complexes are oxidized, both of them associated to IL transitions. The MLCT bands disappear when oxidizing the metal. Based on **both techniques**, the lowest-lying MLCT excited states in all complexes (**1**-**3**) can thus be formulated as charge-separated species [Ru^{III}-(Mebpy-$CN^{\cdot-}$)].

The experimental data described above can be explained by DFT (density functional theory) calculations, from which a detailed description of the molecular orbitals (MO) of coordination compounds, such as those described in this work, can be extracted. Indeed, as shown in Figure 3, the HOMOs (highest occupied molecular orbitals) in complexes **1**-**3** are all centered in only one d orbital of the Ru center. The LUMOs (lowest unoccupied molecular orbitals) in the same species are delocalized over the Mebpy-CN ligands; therefore, the lowest-lying energy absorption bands can be assigned to MLCT transitions from a non-bonding Ru orbital to an antibonding orbital of Mebpy-CN for all complexes. These pictures of molecular orbitals indicate the highest probabilities of electron densities and can be made by using programs such as GaussSum.[7] Calculated orbital energies are consistent with the redox potentials measured by electrochemical methods and disclose an increasing stabilization of the bipyridyl ligands when going from **1** to **3**, a result of importance for designing better sensitizers in solar cells that can absorb further in the IR region.

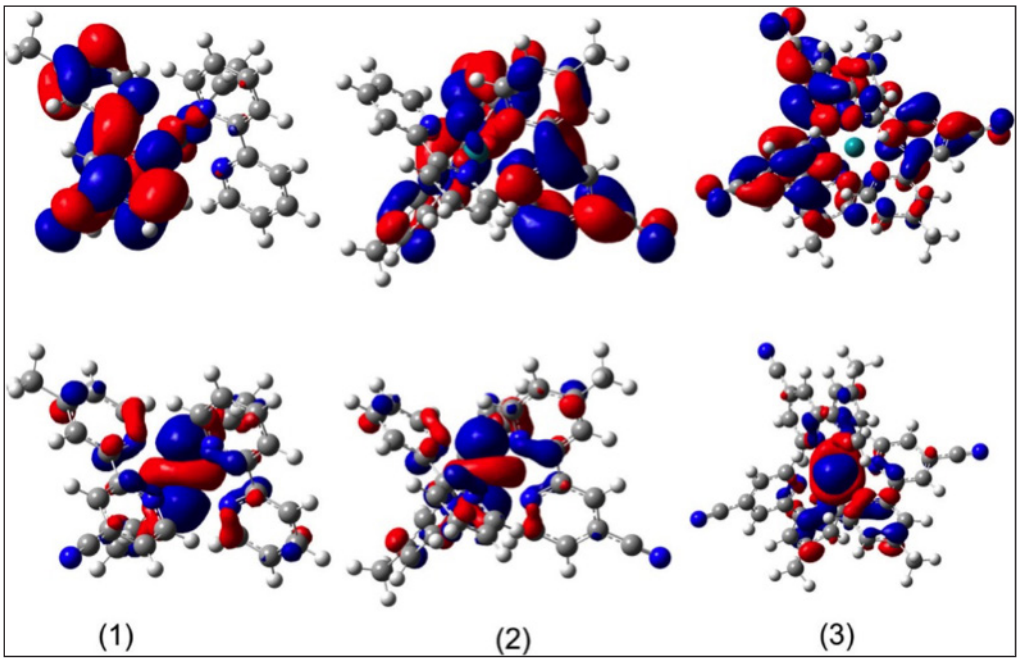

Figure 3. Pictures of LUMOs (top) and HOMOs (bottom) in complexes **1**-**3**.

In order to test the applications of these complexes in dye-sensitized solar cells (DSCs), we first anchored them on the surface of porous TiO_2 films.[8] The nitrile groups are linked to this nanocrystalline semiconductor, as evidenced by Raman spectra of the adsorbed species. In effect, the nitrile stretching frequency appearing at 2240 cm^{-1} in the pure complexes is displaced to 2333 cm^{-1} in the same complexes adsorbed onto TiO_2. This large positive shift indicates coordination of the free N of the nitrile group to a Ti^{4+} center. Solar cells can be built with these sensitized electrodes, a Pt-counter electrode and iodine/iodide as a redox mediator electrolyte dissolved in a polymeric matrix. When irradiated by a solar simulator, the cells assembled with the Ru complexes (**2**) and (**3**) as TiO_2 sensitizers exhibited almost identical current–potential curves, with short-circuit photocurrents of 1.25 mA cm^{-2}, fill factors of 0.5, and overall efficiencies around 0.4 %.[8] The Ru complex (**1**) and a similar Re complex with formula Re(Mepbpy-CN)$(CO)_3$Cl (**ReL**) did not perform as well as sensitizers. These results were consistent with those obtained from quantum efficiency curves and impedance spectra.

The quantum efficiency (*QE*) spectra of these solar cells, acquired at (25 ± 1) ºC, are shown in Figure 4(a). *QE* values were calculated as the ratio of the number of carriers collected by the solar cell to the number of photons of a given energy incident on it. Figure 4(b) shows the current-potential curves obtained under irradiation with the solar simulator (linear sweep voltammetry, 5 mV s^{-1}) at (30 ± 1) ºC. From these *I-V* curves, the efficiency of conversion of light into electrical energy could be determined for each cell.[8]

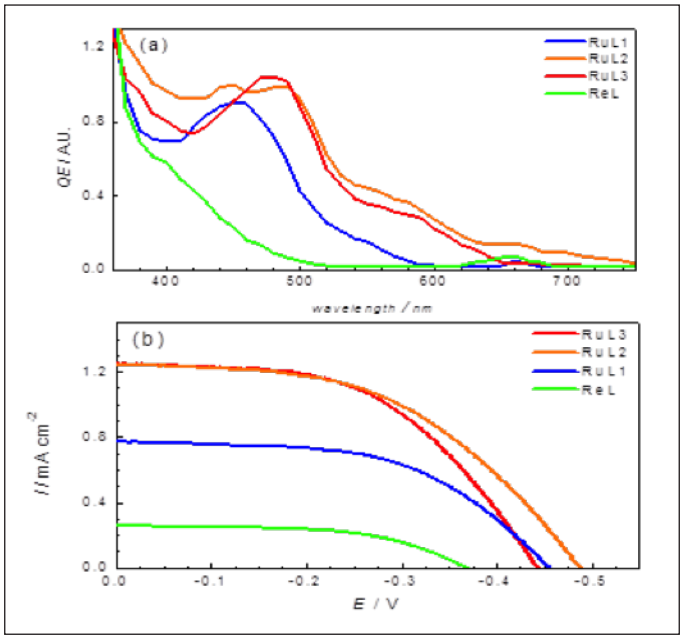

Figure 4. Solar cells (1 cm^2) assembled with TiO_2 sensitized with RuL1(**1**), RuL2 (**2**), RuL3 (**3**) and **ReL**: (a) quantum efficiencies spectra and (b) current-potential curves under polychromatic irradiation.

From Figure 4(a), it can be deduced that, except for the solar cell assembled with **ReL**-sensitized TiO_2, the higher efficiencies were observed for incident radiation with wavelengths between 460 and 520 nm, in excellent agreement with the UV–Vis spectra of sensitized TiO_2 films. By comparing *QE* and *I–V* curves in Figure 4, a similar performance under irradiation was disclosed for the cells assembled with complexes (**2**) and (**3**) as TiO_2 sensitizers, exhibiting overall efficiency values η = 0.44%. The lower performance of (**1**) can be associated with less amount of adsorbed complex, while the poor performance of the **ReL** solar cell can be related to its extremely low absorption in the visible region. We thus conclude that ruthenium bipyridyls substituted with nitrile groups can be considered as promising candidates for sensitizing semiconductors used in the design of novel DSCs.

Based on the previous conclusion, we have recently synthesized new ruthenium polypyridyl complexes whose physicochemical properties can be modulated by structural modifications adequate for increasing efficiency of the energy conversion process in DSCs.[9] These species, with formulae [Ru(4,4'-X_2-bpy)$_2$(Mebpy-CN)](PF$_6$)$_2$, where X = CH_3 (**4**), X = OCH_3 (**5**) and X = $N(CH_3)_2$ (**6**), whose structures are shown in Scheme 2, have been characterized by electrochemical, spectroscopic and photophysical techniques.

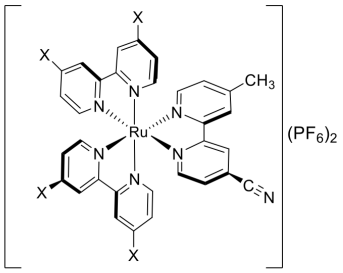

X = CH_3 **(4)**, X = OCH_3 **(5)**, X = $N(CH_3)_2$ **(6)**

Scheme 2. Structures of the complexes [Ru(4,4′-X_2-bpy)$_2$(Mebpy-CN)](PF$_6$)$_2$

As the electron donor strength of X in the 4,4′-X_2-bpy ligand increases when going from (**4**) to (**6**), a cathodic shift of the redox potentials of the Ru^{III}/Ru^{II} couples ($E_{1/2}$ = 1.23, 1.06 and 0.72 V, in CH_3CN, vs. SCE) and displacements towards lower energies of the absorption and emission maxima in CH_3CN ($\lambda_{max}/\lambda_{em}$ = 475/666, 485/707 and 530/800 nm) were

observed, consistent with quantum mechanical calculations. The emission quantum yields and the lifetimes of the excited states in CH_3CN saturated with Ar (τ = 672, 322 and 21 ns) decreased in the same order, according to the energy gap law.

The three complexes were anchored by the nitrile group to the surface of ZnO nanowires, which were grown in FTO (fluorine-doped tin oxide) glasses using a hydrothermal technique, and they all showed promising photosensitizing properties for the design of new solar cells.

Another example of a correlation between spectroelectrochemical and photopysical measurements helpful for disclosing the nature of light-induced excited states has been described in our recent work[10] concerning the properties of a rhenium(I) complex of formula $[Re(Mebpy\text{-}CN)(CO)_3(CH_3CN)]^+$, (**7**), whose structure is displayed in Scheme 3, as an ORTEP diagram deduced from X-ray diffraction data.

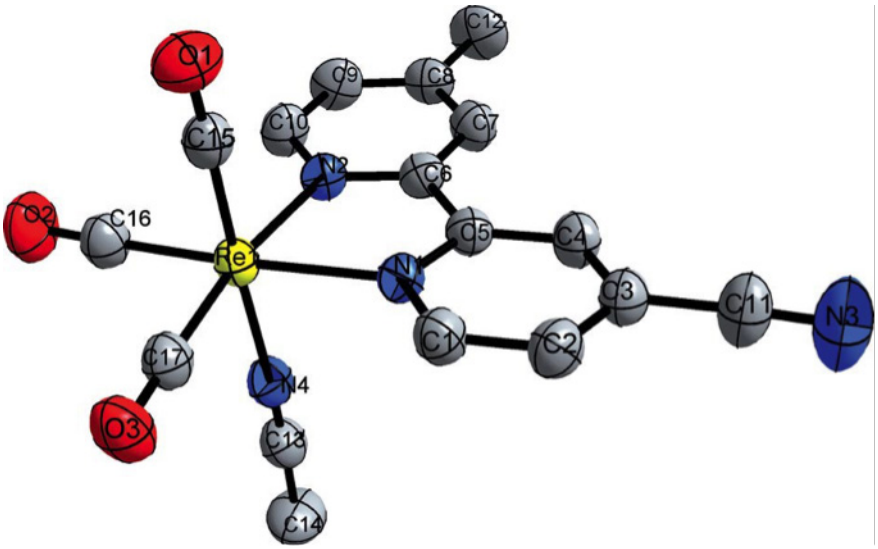

Scheme 3. Structure of $[Re(Mebpy\text{-}CN)(CO)_3(CH_3CN)]^+$, (**7**). The different colors indicate the following atoms: Re (yellow), C (black), N (blue) and O (red). All H atoms have been omitted for clarity reasons.

As shown in Figure 5, UV-Vis spectroelectrochemistry for this cation at an applied potential of $V = -0.9$ V, resulted in the bleaching of the MLCT band (from a d orbital of Re to a π^* orbital of bpy) at λ_{max} = 350 nm and the appearance of new bands at λ_{max} = 370 and 450 nm, which are consistent with the generation of the radical anion Mebpy-CN$^{\cdot -}$. Reoxidation at $V = -0.7$ V, produced an almost total recovery of the original complex.

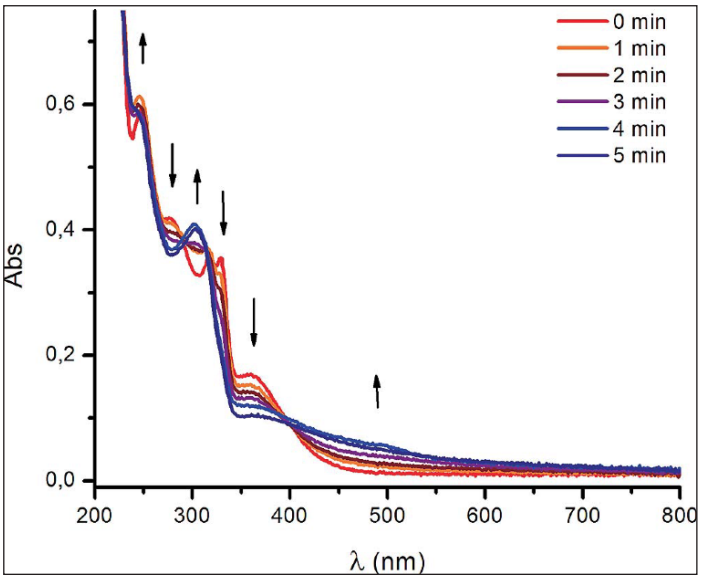

Figure 5. UV/Vis spectroelectrochemistry of (**7**) in CH_3CN, 0.1 M TBAH, at $V = -0.9$ V.

Figure 6 shows the transient spectra obtained at different times for the excited state of (**7**), as detected by LFP. The band maxima observed at λ_{max} = 370 and 460 nm correspond to IL transitions of Mebpy-CN$^{\cdot-}$. Similar values were observed in the time-resolved UV-Vis spectrum of excited [Re(bpy)$(CO)_3$Cl].[11] This assignment is consistent with the reduction experiments described in the paragraph above, as well as with the transient spectra observed for ruthenium complexes with Mebpy-CN. Excited states lifetimes were determined both by LFP (τ = 293 ns, as indicated in Figure 6) and TCSPC (τ = 283 ns); they were both mono-exponential and equal within experimental error, thus supporting the assignment of the emitting state as the charge-separated species [Re^{II}-(Mebpy-CN$^{\cdot-}$)].

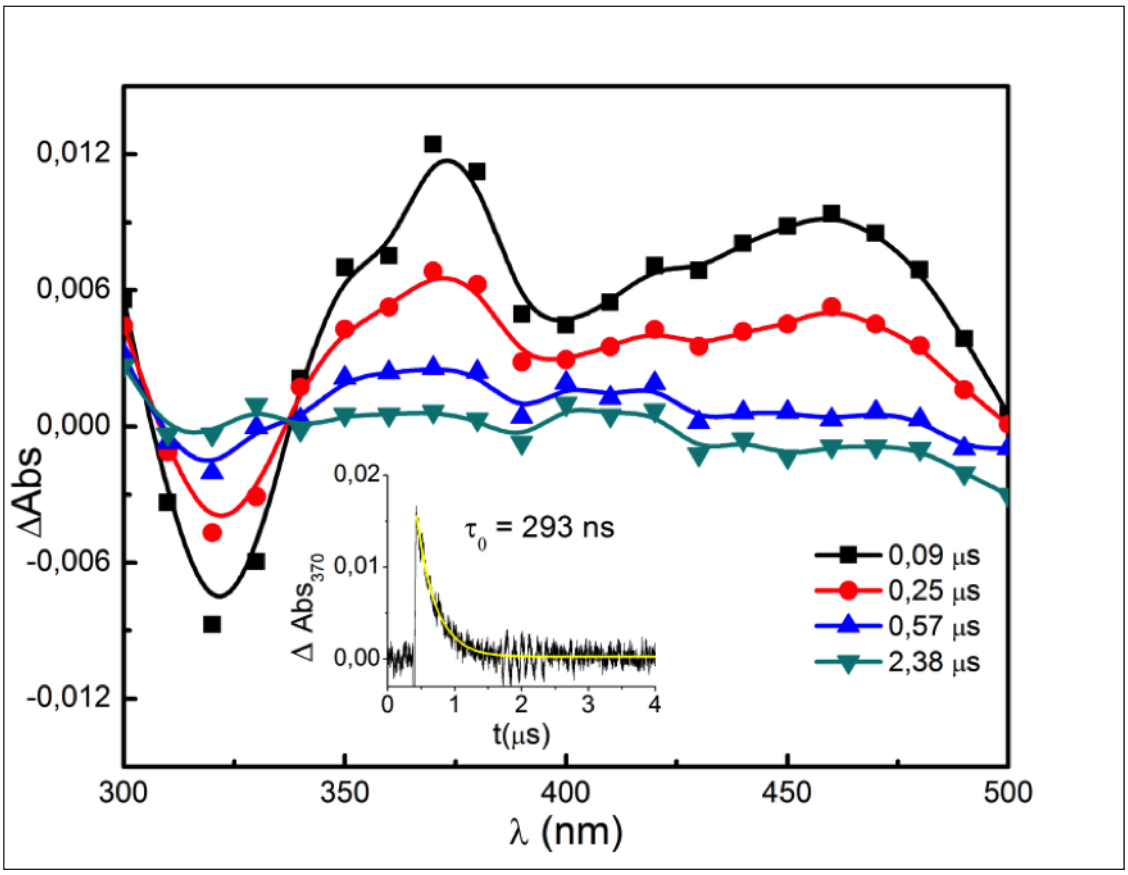

Figure 6. Transient spectra for the excited state of complex (**7**) in CH_3CN at r.t. obtained by LFP. Inset: transient absorption decay monitored at λ = 370 nm.

We conclude that spectroelectrochemical data for this triscarbonylrhenium(I) complex are fully compatible with transient absorption measurements, as was the case with the previously described series of polypyridylruthenium(II) complexes. However, using Re complexes as sensitizers in solar cells is limited by the small amount of visible light that they can absorb.

Using quantum mechanical DFT calculations, the compositions of some frontier MOs for complex (**7**) could be determined, as shown in Table 2.

Table 2. Energies and percent contributions of the 3 highest HOMOs and the 3 lowest LUMOs for the ground state of complex (**7**).

MO	*E*(eV)	Re(%)	Me-bpyCN (%)	CO's(%)	AN(%)
LUMO+2	-1.73	2	91	6	0
LUMO+1	-2.40	0	99	1	0
LUMO	-3.29	2	93	4	0
HOMO	-7.29	60	10	25	5
HOMO - 1	-7.40	61	10	23	5
HOMO -2	-7.62	69	2	29	0

The LUMO is centered at the Mebpy-CN ligand, but the mixing between d_{π}(Re) and CO orbitals in the HOMO of (**7**) indicates that the lowest energy lying absorption band of (**7**) can be assigned to a MLLCT (metal-ligand to ligand charge transfer) transition. The EDDM (electron-density difference map) for this band can thus be envisaged as a transfer of electronic density from the $Re(CO)_3$ fragment to Mebpy-CN. LUMO and HOMO diagrams for complex (**7**) are displayed in Figure 7.

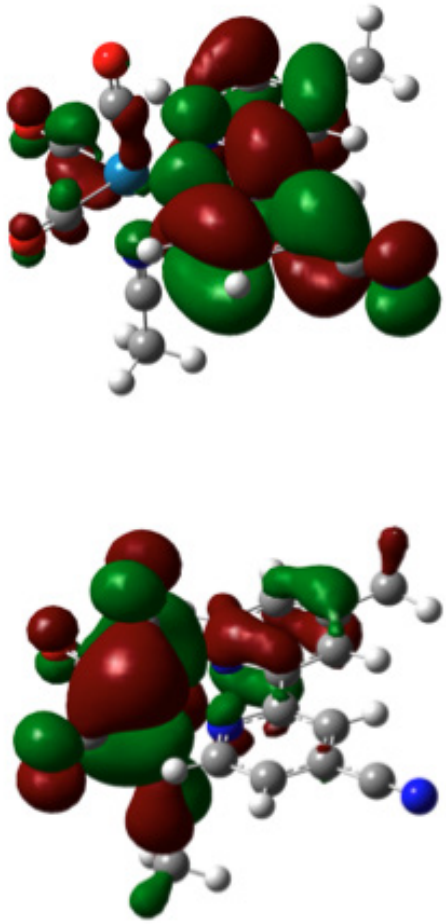

Figure 7. Pictures of LUMO (top) and HOMO (bottom) of complex (**7**).

The calculated UV-Vis spectrum of complex (**7**) matches with its experimental spectrum reasonably well, confirming the assignment of charge-transfer transitions.

2. Sensors

The parallel use of spectroscopic measurements with photophysical studies can also help to elucidate the nature of charge-transfer excited states relevant in chemical sensing.

As a prototypical example, we have recently reported[12] the synthesis and physicochemical properties of a new binuclear complex of formula $[(CH_3CN)(CO)_3Re(4,4''\text{-azobpy})Re(CO)_3(CH_3CN)](PF_6)_2$, (**8**), with 4,4´´-azobpy = 4,4´´-azobis-(2,2'-bipyridine). The symmetrical structure of the cationic part in (**8**), as deduced from NMR data, is shown in Scheme 4.

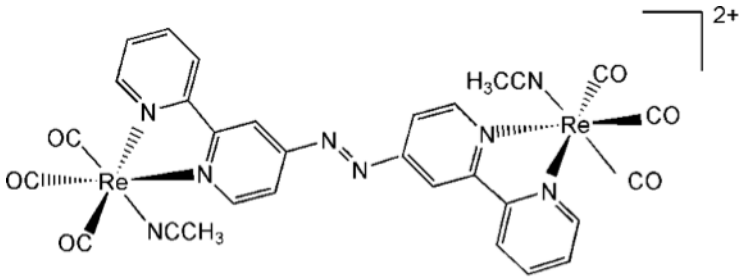

Scheme 4. Structure of the cation in complex (**8**).

The UV-Vis spectrum of (**8**) in CH_3CN is shown in Figure 8. The bands at $\lambda < 300$ nm were assigned to IL transitions by comparison with those observed for free 4,4´´-azobpy. The broad band between 300 nm and 500 nm could be deconvoluted into two components (at λ_{max} = 346 and 400 nm) which were assigned to MLCT $d_{\pi}(Re) \rightarrow \pi^*(4,4''\text{-azobpy})$ transitions. The band at the lower energy level was attributed to electron promotion from the HOMO mainly localized in the metal to the LUMO mainly localized in the azo bridge. On the other hand, the higher energy band was attributed to a transition from the HOMO to the LUMO+1 mainly localized in the bipyridyl rings. These assignments were confirmed by DFT calculations.

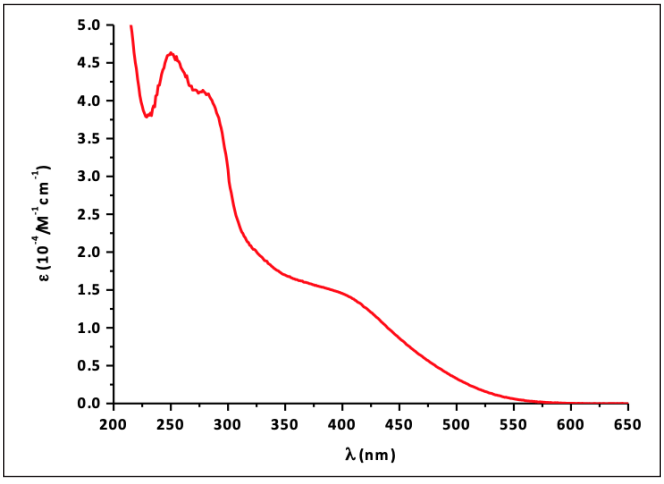

Figure 8. UV-Vis spectrum of complex (**8**) in CH_3CN.

When applying an external potential V = - 316 mV to the spectroelectrochemical cell filled with a solution of (**8**) ($C = 10^{-4}$ M) in CH_3CN, a decrease in the intensity of IL transition bands can be observed, while new bands appear at λ_{max} = 460, 550 and 800 nm , attributed to IL transitions of the azobpy$^-$ radical, as expected after 1-electron reduction of (**8**). These bands are similar to those reported for Re complexes containing reduced azo ligands.[13] The shift to higher energies

of the MLCT band at λ_{max} = 400 nm can be explained by the increase of electron density in the bridging ligand upon reduction and the subsequent destabilization of the HOMO Re (d_{π}) orbitals. When the applied potential is restored to 0 V, the original spectrum can be fully recovered, in agreement with voltammetric studies. When an external potential of V = - 800 mV is applied, the intensities of the bands attributed to the radical increase when compared to the first 1-electron reduction, and the MLCT band shifts to even higher energies. As shown in Figure 9, the UV-Vis spectra of the 2-electron reduction processes can be split into two sets: the first one corresponds to the first 1-electron reduction with an isosbestic point at λ = 395 nm, and the second one corresponds to the subsequent 2-electron reduction with two isosbestic points at λ = 449 nm and 595 nm.

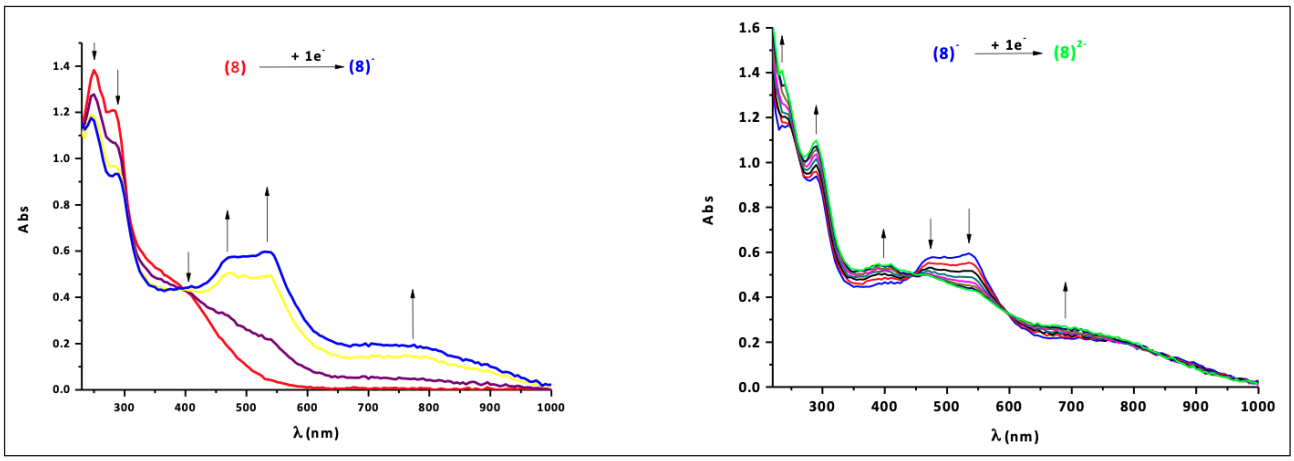

Figure 9. UV-Vis absorption changes in (**8**) after applying an external potential of V = -800 mV split into two subsequent 1-electron processes.

Results from UV-Vis spectroelectrochemistry can be nicely compared with changes observed in FT-IR spectroelectrochemical experiments. In effect, by using an IR spectroelectrochemical cell with an applied external potential V = - 316 mV, the frequencies corresponding to ν(C≡O) of the carbonyl groups in (**8**) shift to lower energies, with the band assigned to CO_{eq} groups (those at lower energy) being more affected. Isosbestic points are detected at 2036 and 1932 cm^{-1}, This effect can be explained by considering that the electron withdrawing character of the 4,4´´-azobpy ligand is diminished when its electron density increases upon reduction, leading to an increase of the π-backbonding effect from the metallic center to the CO ligands, and a consequent decrease of CO bond orders. Vibrational frequencies in diatomic species are proportional to the square root of the strength of the chemical bond between two atoms (as measured by its force constant).[14] The frequencies of CO_{eq} groups are more affected, since they have adequate symmetry to interact with the metal orbitals, as opposed to CO_{ax} groups that are orthogonal to the 4,4´´-azobpy ligand.[15] When the applied potential is restored to 0 V, the original spectrum is fully recovered.

As shown in Figure 10, when an external potential V = - 770 mV is applied, more pronounced shifts to lower energies of CO bands frequencies are observed as a consequence of the 2-electron reduction process of 4,4´´-azobpy. Isosbestic points are also detected, and the spectrum of the 1-electron reduction product can be observed at the beginning of the reduction.

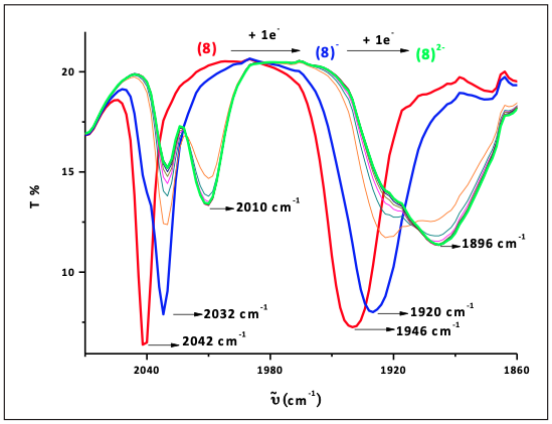

Figure 10. IR subsequent changes upon reduction of (**8**) in CH_3CN at V = - 770 mV.

The UV-Vis spectral changes of **(8)** upon addition of excess of the reductant *L*-Cysteine (*L*-Cys) were measured in a H_2O/CH_3CN mixture (1:1) at pH = 6. After reduction, the LUMO is populated and the band at λ_{max} = 400 nm (assigned to the lowest energy MLCT) disappears, while a new CT band is observed at λ_{max} = 342 nm, as shown in Figure 11. On the other hand, a new band appears at λ_{max} = 312 nm that can be assigned to a MLCT from the HOMO to the LUMO+1. Reaching the ratio [*L*-Cys]/[complex] 2:1, no changes on the UV-Vis spectra have been detected, thus pointing to a double reduction of the azo group. This chemical reduction is also reversible when the solution is exposed to atmospheric oxygen. The detection limit was determined to be in the submicromolar region, so that this rhenium complex can be used for sensing *L*-Cys; abnormal levels of thiols in human blood are indicative of diverse neurological diseases.[16]

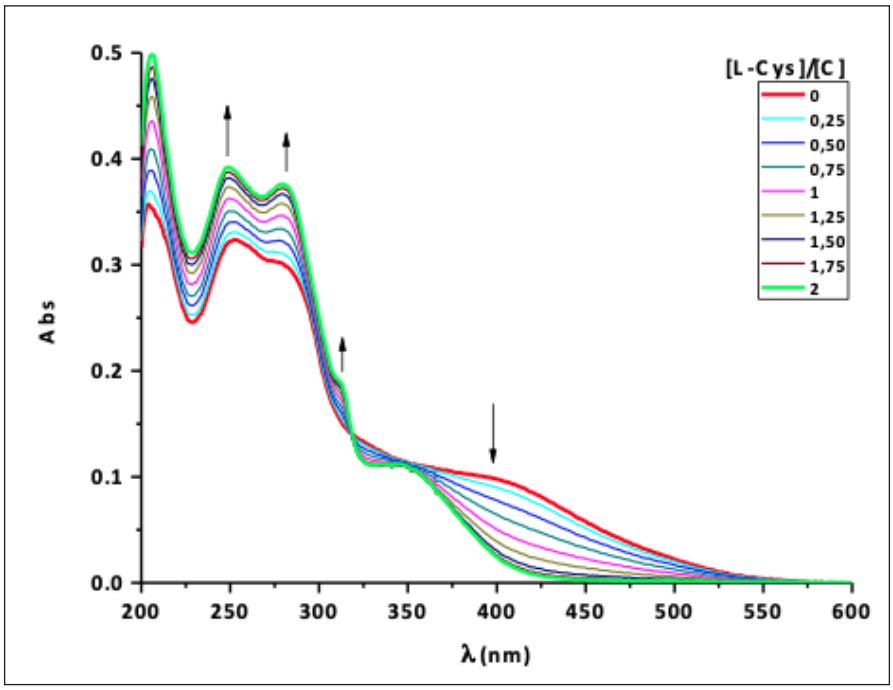

Figure 11. UV-Vis spectral changes with the addition of *L*-Cys at different ratios [*L*-Cys]/[C] where C is the molar concentration of (**8**) in H_2O/CH_3CN (1:1).

When adding excess sodium dithionite (a strong reductant of formula $Na_2S_2O_4$) to a solution of (**8**) in a CH_3CN/H_2O mixture (300:1), the UV-Vis spectrum, as shown in Figure 12, displays the same changes as those described before upon reduction with *L*-Cys. However, after reduction with dithionite, the emission intensity is enhanced by an order of magnitude in comparison with the non-reduced complex, as shown in Figure 13. An explanation for this emission enhancement effect, which is absent in the *L*-Cys reduced product, is based on the fact that the concentration of water is much higher in the former case. Water may quench the emission from the ^{3}MLCT excited state by protonation of the reduced azo moiety.

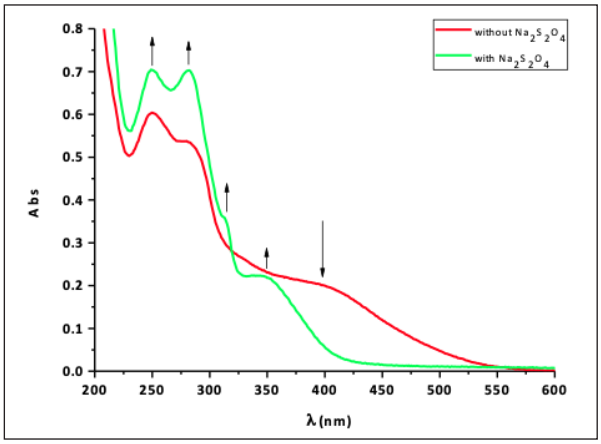

Figure 12. Changes in the UV-Vis spectrum of (**8**) upon addition of $Na_2S_2O_4$, to CH_3CN/H_2O (300:1).

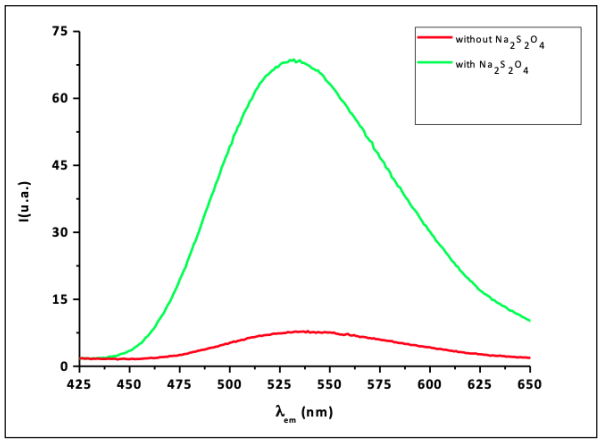

Figure 13. Changes in the emission spectrum of (**8**) upon addition of $Na_2S_2O_4$ to CH_3CN/H_2O (300:1).

It can be concluded that complex (**8**) acts an "on-off" molecular switch, a property reflected in the observed large changes in both absorption and emission spectra when adding a strong reductant such as dithionite in CH_3CN/H_2O (300:1) solutions.

As shown in Figure 14, dual emission has been detected for complex (**8**) in pure CH_3CN. At λ_{exc} = 346 nm, a weak emission is observed at λ_{em} = 530 nm (with quantum yield $\varphi = 3 \times 10^{-4}$), which can be attributed to a decay from a ^{3}MLCT d_π(Re)-π^* excited state with the π^* orbitals centered at the bipyridyl rings. At λ_{exc} = 400 nm, a new emission appears at λ_{em} = 575 nm (with a similar quantum yield), which can be ascribed to a decay from a ^{3}MLCT d_π(Re)-π^* excited state with the π^* orbitals centered at the azo bridging group. At room temperature, emission bands of tricarbonylpolypyridylrhenium(I) complexes are normally non-structured, so that this dual emission cannot be ascribed to coupling to vibrational modes. Although azopyridines usually undergo *cis-trans* isomerization when applying UV and/or visible light, we irradiated samples of complex (**8**) in a CH_3CN solution at λ_{exc} = 270 nm for a couple of hours and no changes in absorption or emission spectra were detected, in agreement with previous reports on Ru complexes with 4,4´-azopy.[13] This result evidenced that isomerization cannot account for the two nearly isoenergonic emissions.

It must be noted that we found emission in complexes containing 4,4´´-azobpy as the only chromophoric ligand for the first time. In Ru or Os bipyridyl species of 4,4´´-azobpy, this luminescence is masked by the strong emission originated from ^{3}MLCT d_π(M)-π^* excited states (M = Ru or Os) with the π^* orbitals centered at the auxiliary 2,2´-bipyridyl ligands.[17]

Figure 15 shows the fit of both decays as measured by TCSPC with two lifetimes: τ = (16 ± 1) ns for the decay at λ_{em} = 530 nm and τ = (621 ± 7) ns for the decay at λ_{em} = 575 nm. The excitation wavelength (λ_{exc} = 390 nm) was close to the value of the absorption maximum of the lowest energy MLCT. The results were similar when using an excitation wavelength (λ_{exc} = 340 nm) close to the value of the higher energy MLCT, but the weighting factor of the lower lifetime is much higher, supporting its assignment to the emission at λ_{em} = 530 nm.

Both the quantum yield and the lifetime for the first decay are much lower than those reported for similar Re(I) species, indicating luminescence quenching by crossing to a second MLCT state, which in turn decays with a low quantum yield due to quenching of the bridging ligand by excited states. The longer lifetime may be due to increased delocalization on the bridging ligand 4,4´´-azobpy as compared to bpy. It is well known that excited states lifetimes in this type of complexes can be increased when IL transitions are involved. TD-DFT calculations, described in the following paragraph, support the conclusion that the lowest-energy emission originates from an excited state with the LUMO centered on the azo moiety.

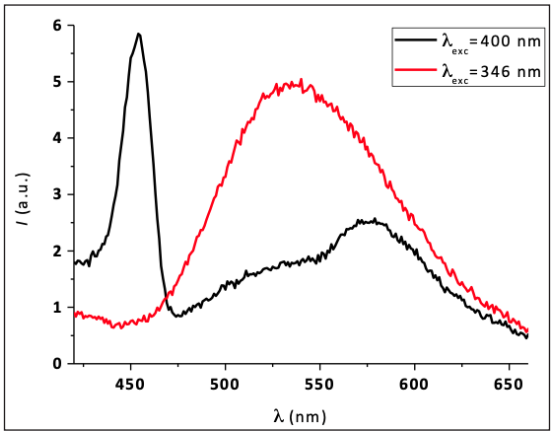

Figure 14. Emission spectra of (**8**) in deareated CH_3CN, at room temperature and at two excitation wavelengths (the red line corresponds to λ_{exc} = 346 nm and the black line, to λ_{exc} = 400 nm). The band at λ_{em} = 450 nm is a Raman band of CH_3CN.

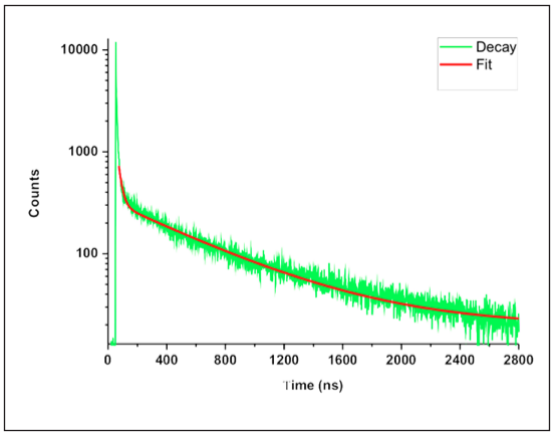

Figure 15. TCSPC decays of excited states of (**8**) in deareated CH_3CN, at room temperature and λ_{exc} = 390 nm.

TD-DFT calculations were done for both complex (**8**) and its reduced and protonated form (hydrazine bridge). Scheme 5 shows the energy level diagrams together with figures for some frontier MO's. The LUMO for complex (**8**) is centered on the azo moiety of 4,4´´-azobpy, while that of the reduced and protonated species (**8H$_2$**) is centered on the bipyridyl rings of 4,4´´-azobpy. These findings are consistent with the spectroscopic and photophysical properties described before. However, when a strong reductant such as dithionite is added in acetonitrile/water (v/v, 300/1), the emission is enhanced by one order of magnitude (see Fig. 13), since the LUMO becomes centered on the bipyridyl rings. Additionally, the MO energy diagrams in Scheme 5 indicate that the difference between the LUMO and the HOMO in the reduced/protonated form are almost equal to the difference between the LUMO+1 and the HOMO in complex (**8**), so that both emissions (originated from a MLCT excited state centered on the bipyridyl rings) are expected to occur at almost the same energies.

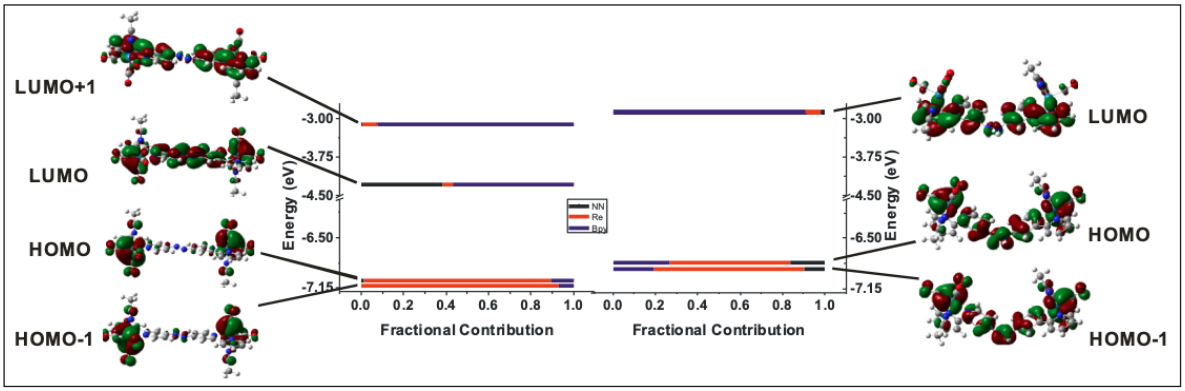

Scheme 5. MO energy diagrams for complex (**8**) (left) and for the doubly reduced and protonated species (**8H$_2$**) (right).

Another example of the importance of using both spectroelectrochemical and photophysical data to infer the nature of charge-transfer excited states in molecules that can act as sensors or "molecular switches" is a new mononuclear Ru complex with formula $K_2[Ru(L)(CN)_4]$, (**9**) , with L = 4,4´´-azobis-(2,2'-bipyridine), that we recently prepared and characterized by spectroscopic, electrochemical and photophysical techniques.[18] The structure of the anion in (**9**) is shown in Scheme 6. The use of $[Ru(L)(CN)_4]^{2-}$ species as sensors of biological relevant analytes has not been widely explored, and the azo function is one of the most versatile functional units due to its sensitivity to the addition of electrons, protons or photons.[12,13,17,19] The use of (**9**) as a water soluble probe for *L*-Cys detection by means of its remarkable spectroscopic changes upon reduction and subsequent protonation has also been successfully explored.[18]

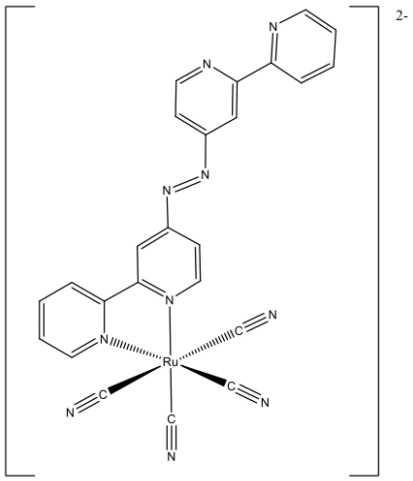

Scheme 6. Anion structure in complex (**9**).

In effect, as shown in Figure 16, when excess *L*-Cys is added to an aqueous solution of (**9**), the intensity of the lowest energy absorption band of its UV-Vis spectrum (at λ_{max} = 497 nm) decreases. There is also an increase in IL band absorbance at λ_{max} = 242 nm, and a new band appears at λ_{max} = 394 nm after 10 min. Three isosbestic points are detected at λ = 313, 370 and 418 nm. Moreover, the changes induced by reduction with *L*-Cys are fully reversible; the original spectrum of (**9**) can be fully recovered by the addition of one drop of a 1:5 H_2O_2/water solution. The mechanism of azo compounds reduction in an aqueous solution is well known, and the formed product is the hydrazo species -HN-NH- when using dithionite as reducing agent;[20] recently, Zeng *et al*.[21] reported the same results for Ru complexes having L as bridging ligand and using GSH as reductant.

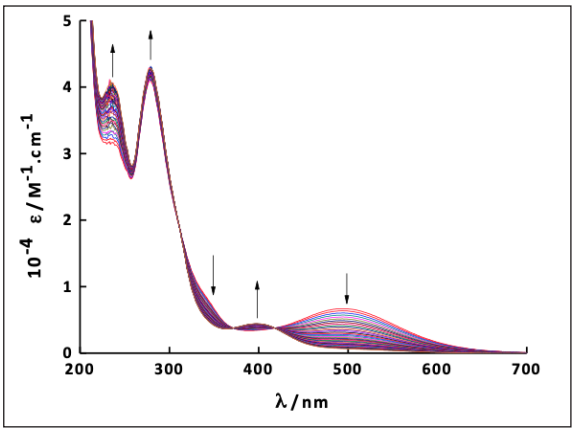

Figure 16. UV-Vis spectral changes upon addition of an *L*-Cys excess to an aqueous solution of (**9**)(C = 5.1 x 10^{-5} M). The arrows indicate the evolution of spectra from t = 0 to t = 10 min.

When an external potential of value V = -800 mV is applied to a spectroelectrochemical cell containing an aqueous solution of (**9**) (C = 3.8 x 10^{-5} M), the intensities of the bands in the UV region increase, with greater changes being

observed for the band at λ_{max} = 242 nm. In the visible region, the intensity of the band at λ_{max} = 497 nm decreases, while a new band emerges at λ_{max} = 394 nm. Identical isosbestic points, as shown in Figure 16, are detected. The original spectrum was restored when a potential of 0 V was applied for 10 min after reduction.

This is the first report of applying the spectral changes originated from a double PCET (proton-coupled electron transfer) process of an azo group in a bipyridyl ligand coordinated to a tetracyanoruthenium(II) moiety, as shown in Scheme 7, for molecular sensing purposes, in particular for detecting the biologically relevant analyte *L*-Cys. We have only performed these experiments at neutral pH but, considering that detecting thiols in living cells is a highly relevant issue in biochemistry,[22,23] we propose to extend these studies including pH effects on the sensitivity of detection of *L*-Cys and similar biological reductants such as GSH. Since the analytical method described here is of the kinetic mode, we hope that selectivity will be eventually achieved by fixing different times of detection. Additionally, it can be envisaged that these types of complexes may be useful for detecting the related "smallest thiol", H_2S/HS^-, which has an important physiological role as a signaling agent.[24] More possibilities arise when considering the fact that thiolates can be used as ligands in redox-active transition metal complexes with a biochemical behavior connected with other crucial physiological messengers such as NO.[25] The diverse uni- or multi-electron transfers in which both compounds are involved in aqueous solutions generate intermediate species whose structure and reactivity have to be studied in order to understand biological responses. On the other hand, the photochemical behavior of these species could be an interesting area to be further explored.

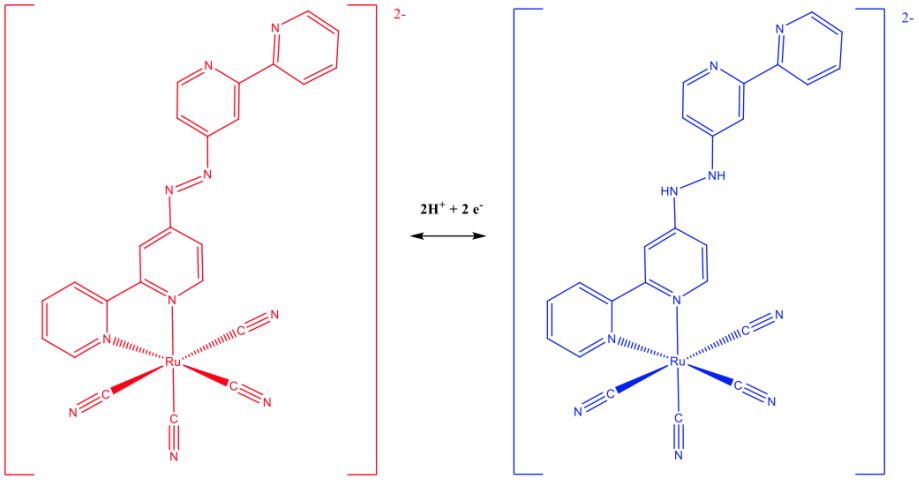

Scheme 7. PCET process between complex (**9**) (red) and complex (**9H2**) (blue).

Complex (**9**) does not emit in water at r.t., since the azo group of 4,4´´-azobpy can quench the radiative decay from the lowest ^{3}MLCT excited state. Reviving the emission can be achieved by introducing an electron in the π* orbital mainly localized on the bridging group (-N=N-) so that the non-radiative decay path is suppressed. Upon reduction and protonation of (**9**), the emission is turned on. This "off-on" switching behavior – based on a different mechanism – has been described before for Ru (II) and Ir (I) complexes in the sensing of thiols.[22,23]

As shown in Figure 17, there is no emission in (**9**), but upon reduction and protonation of the azo group to form the species (**9H2**), emission appears at λ_{em} = 610 nm (λ_{exc} = 394 nm). The quantum yield of (**9H2**) in water is ϕ = 0.0027, which is about half the value observed for the related complex $[Ru(bpy)(CN)_4]^{2-}$.[26]

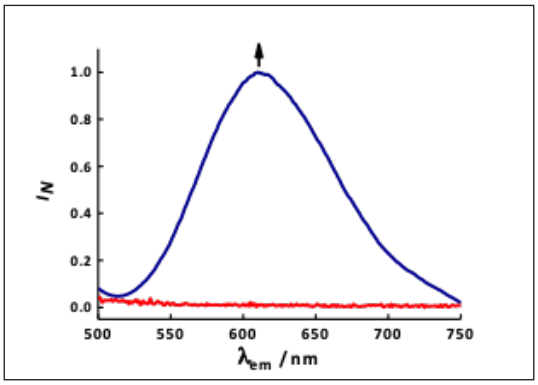

Figure 17. Normalized emission spectra of (**9**) (red) and (**9H2**) (blue) in water (λ_{exc} = 394 nm) at r.t.

Excellent linear correlations were found between the absorbance changes of (**9**) ($C \approx 10^{-5}$ M) at λ = 497 nm and [*L*-Cys] after 5 min, as well as between emission changes at λ = 610 nm and [*L*-Cys] after 5 min. From these plots, detection of *L*-Cys at the submillimolar level can be made. It should be noted that emission and absorption properties of cyano-ruthenium complexes are extremely solvent-dependent due to strong interactions of the cyanide co-ligands with solvents of different acceptor numbers; therefore, the nature of the involved electronic states can also be modulated by solvent changes.[27]

For a reasonable explanation of the absorption and emission properties of (**9**) and its reduced and protonated form (**9H2**), quantum mechanical calculations were carried out. The MO's diagrams of (**9**), and (**9H2**) – built with DFT calculations – are shown in Figures 18 and 19, together with the contributions of each group.

Figure 18 shows that the HOMO in (**9**) is localized in the metal with contributions of the coordinated cyano groups, while the LUMO is located mainly in the azo bridge of L = 4,4´´-azobpy; on the other hand, the LUMO+1 MO has more contributions of the bpy ring. Thus, the lowest energy visible absorption band is expected to be a MLCT Ru → L, with L having an important contribution from the azo bridge, while the second band at higher energy can be assigned to a similar MLCT Ru → L, with L having an important contribution from the bpy ring.

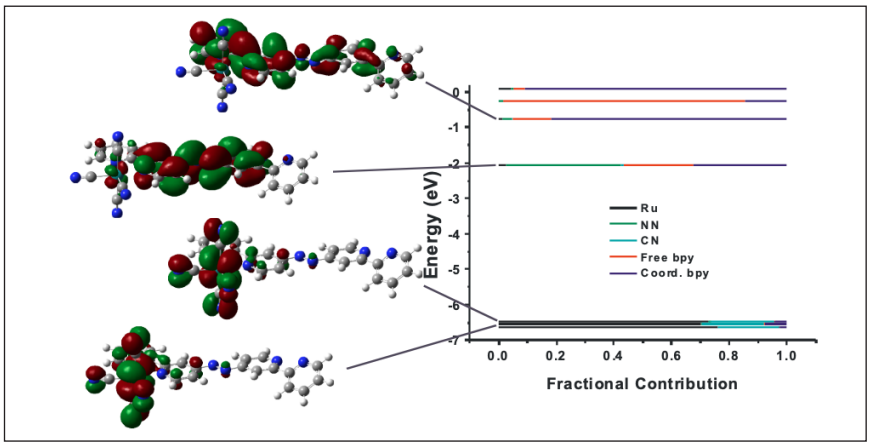

Figure 18. MO energies and electron density diagrams for the two highest HOMOs and two lowest LUMOs in (**9**). Different group contributions are marked by different colors.

Figure 19 shows the MO diagrams in (**9H2**). The effect of the first one-electron reduction, as proposed before, is filling the π* orbital centered on the azo bridge. Upon reduction and protonation to form the hydrazo form, the complex adopts a torsioned configuration, which implies rotation trough the -HN-NH- bond as depicted in the same Figure.

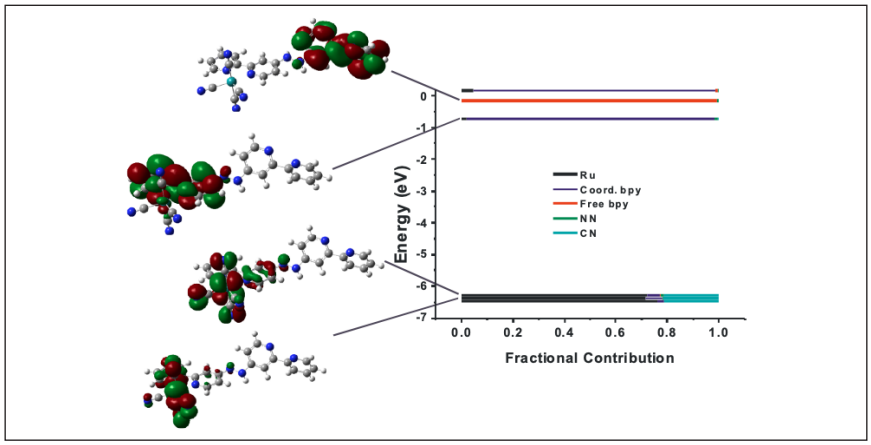

Figure 19. MOs energies and electron density diagrams for the two highest HOMOs and two lowest LUMOs in (**9H2**). Different group contributions are marked by different colors.

All these assignments were corroborated by calculations at the TD-DFT level. The calculated UV-Vis spectrum of (**9**) presents reasonable agreement with its experimental spectrum, as shown in Figure 20.

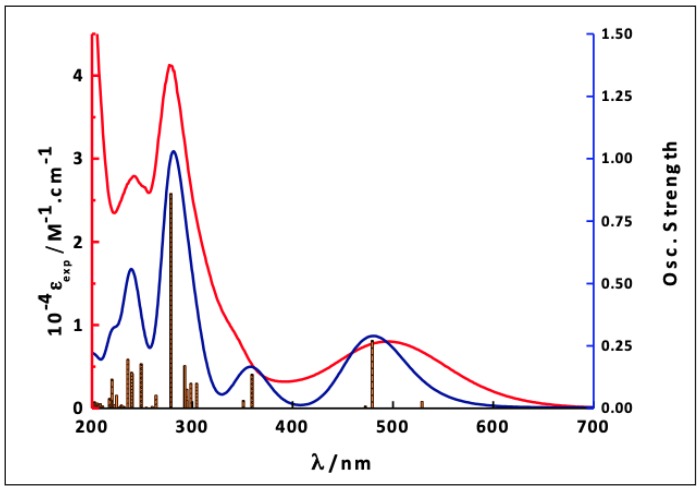

Figure 20. Experimental (red plot) and calculated (blue plot) UV-Vis spectrum of (**9**) in water at r.t.

TCSPC measurements were carried out to explore the nature of the excited states of (**9H2**). The lifetime of the ^{3}MLCT excited state of the reduced and protonated form of (**9**), obtained by reduction with *L*-Cys in aqueous media (Tris buffer, pH = 7.5), was determined by following the emission decay at λ = 610 nm after pulse excitation at λ = 390 nm. The decay of the ^{3}MLCT emission showed a double exponential behavior. The shortest lifetime (τ_1 = 9.7 ns) was assigned to the decay from the ^{3}MLCT excited state of the *cis* form of (**9H2**), while the longer one (τ_2 = 75 ns) was assigned to a decay from a similar state of the *trans* isomer. These assignments were supported by DFT and TD-DFT calculations of (**9H2**) for the *cis* and *trans* isomers, that revealed the presence of two lowest triplets for each isomer, with that of the *trans* form being at a higher energy that that of the *cis f*orm. This is the expected result, according to the energy gap law.[28]

We conclude that the "on-off" behavior of complex (**9**) can be successfully applied for the determination of the biologically relevant analyte *L*-Cys at the submillimolar range in water. The spectral changes originated from the Ru-4,4´´-azobpy excited state originated upon reduction and protonation of the azo group can be explained by quantum mechanical calculations.

Conclusions

We conclude that both **spectroelectrochemical and photophysical** experiments are complementary in elucidating the nature of light-induced charge-transfer excited states in transition metal complexes that are pertinent in energy conversion or chemical sensing. Simultaneously resorting to these experimental techniques and using quantum mechanical calculations to interpret the obtained results can lead to successful designs of new sensitizers for solar cells or of new chemical sensors for analytes relevant in medical diagnosis and treatment.

To extend the concept introduced by Kaim of using the **best of two worlds** (reaction-oriented electrochemistry with species-focused spectroscopy)[1] to analyze redox reactions in general, we tried to show here the **best of three worlds** (spectroscopy, electrochemistry and photophysics) to characterize the nature of light-induced excited states, an issue which can be considered as a metaphor of a scientific contribution from a far "third world" country.

Acknowledgements

I wish to thank all my collaborators at INQUINOA, INBIONATEC and INFINOA for their important scientific contributions. Financial support from ANPCyT, CONICET and UNT are gratefully acknowledged. N. E. K. is a Member of the Research Career (CONICET).

References

[1] W. Kaim, and J. Fiedler. Spectroelectrochemistry: the best of two worlds. *Chem. Soc. Rev.* 38: 3373-3382, 2009.

[2] P. M. Keane, J. Tory, M. Towrie, I. V. Sazanovich, C. J. Cardin, S. J. Quinn, F. Hartl, J. M. Kelly, and C. Long. Spectro-electrochemical Studies on $[Ru(TAP)_2(dppz)]^{2+}$- Insights into the Mechanism of its Photosensitized Oxidation of Oligonucleotides. *Inorg. Chem.* 58: 663-671, 2019.

[3] J. H. Mecchia Ortiz, N. Vega, D. Comedi, M. Tirado, I. Romero, X. Fontrodona, T.Parella, F. E. Morán Vieyra, C. D. Borsarelli, and N. E. Katz. Improving the Photosensitizing Properties of Ruthenium Polypyridyl Complexes. *Inorg. Chem.* 52: 4950-4962, 2013.

[4] C. E. McCusker, and J. K. McCusker. Synthesis and spectroscopic characterization of CN-substituted bipyridyl complexes of Ru (II). *Inorg. Chem*. 50: 1656-1669, 2011.

[5] W. R. Browne, C. G. Coates, C. Brady, P. Matousek, M. Towrie, S. W. Botchway, A. W. Parker, J. G. Vos, and J. J. McGarvey. The Early Picosecond Photophysics of Ru(II) Polypyridyl Complexes: A Tale of Two Timescales. *J. Am. Chem. Soc.* 125: 1706-1707, 2003.

[6] L. O'Neill, L. Perdisatt, and C. O'Connor. Influence of Auxiliary Ligands on the Photophysical Characteristics of a Series of Ruthenium(II)–Polypyridyl Complexes. *J. Phys. Chem. A* 116: 10718-10735, 2012.

[7] N. M. O'Boyle, A. L. Tenderholt, and K. M. Langner. Cclib: a library for package-independent computational chemistry algorithms. *J. Comp. Chem*. 29: 839-845, 2008. Available from: http://gausssum.sf.net.

[8] J. H. Mecchia Ortiz, C. Longo, and N. E. Katz. Polypyridyl ruthenium complexes containing anchoring nitrile groups as TiO_2 sensitizers for application in solar cells. *Inorg. Chem. Comm.* 55: 69-72, 2015.

[9] F. F. Salomón, N. C. Vega, T. Parella, F. E. Morán Vieyra, C. D. Borsarelli, C. Longo, M. Cattaneo, and N. E. Katz, manuscript in revision.

[10] J. H. Mecchia Ortiz, F. E. Morán Vieyra, C. D. Borsarelli, I. Romero, X. Fontrodona, T. Parella, N. D. Lis de Katz, F. Fagalde, and N. E. Katz. Mono- and Dinuclear Complexes of Tricarbonylrhenium(I) with 4-Methyl-2,2´-bipyridine-4´-carbonitrile. *Eur. J. Inorg. Chem.* 2014(21): 3359-3369, 2014.

[11] K. Kalyanasundaram. Luminescence and Redox Reactions of the Metal-to-ligand Charge-transfer Excited State of Tricarbonylchloro(polypyridyl)rhenium(I) Complexes. *J. Chem. Soc. Faraday Trans. 2*. 82: 2401-2415, 1986.

[12] P. O. Abate, G. Pourrieux, F. E. Morán Vieyra, M. Cattaneo, M. Vergara, and N. E. Katz. A new molecular switch based on a symmetrical dinuclear complex of two tricarbonylrhenium(I) moieties bridged by 4,4″-azobis-(2,2′-bipyridine). *Polyhedron*, 21: 3359-3369, 2018.

[13] G. Pourrieux , F. Fagalde , I. Romero, X. Fontrodona , T. Parella, and N. E. Katz. Electron-, Proton-, and Photon-Induced Spectroscopic Changes in Chromophore-Quencher Tricarbonyl(2,2′-Bipyridine)rhenium(I) Complexes with 4,4´-Azobis (pyridine). *Inorg. Chem*. 49: 4084-4091, 2010.

[14] P. Atkins, and J. de Paula. *Physical Chemistry*, Oxford University Press, Oxford, United Kingdom, 8th. Ed., 2006.

[15] D. M. Dattelbaum, K. M. Omberg, J. R. Schoonover, R. L. Martin, and T. J. Meyer. Application of Time-Resolved Infrared Spectroscopy to Electronic Structure in Metal-to-Ligand Charge-Transfer Excited States. *Inorg. Chem.* 41(23): 6071-6079, 2002.

[16] D. Maheshwaran, S. Priyanga, and R. Mayilmurugan. Copper(II)-benzimidazole complexes as efficient fluorescent probes for L-cysteine in water. *Dalton Trans.* 46 : 11408-11417, 2017.

[17] J. Otsuki, K. Sato, M. Tsujino, N. Okuda, K. Araki, and M. Seno, M. Ruthenium Complexes Containing an Azobipyridine Ligand as Redox-Responsive Molecular Switches. *Chem. Lett.* 25: 847-848, 1996.

[18] P. O. Abate, G. Pourrieux, F.E. Morán Vieyra,C. D. Borsarelli, T. Parella, M. M. Vergara, and N. E. Katz, A Novel Mononuclear Complex of 4,4´´-azobis(2,2´-bipyridine) Coordinated to Tetracyanoruthenium(II) Can Behave as a "Molecular Switch". Polyhedron 174: 114149, 2019.

[19] V. Gonzalez, T. Wilson, I. Kurihara, A. Imai, J. A. Thomas, and J. Otsuki. A dinuclear ruthenium(II) complex that functions as a label-free colorimetric sensor for DNA. *Chem. Commun.* 1868-1870, 2008.

[20] A. H. Gemeay. Kinetics and mechanism of the reduction of some azo-dyes by inorganic oxysulfur compounds. *Dyes and Pigments*, 54: 201-212, 2002.

[21] L. Zeng, S. Kuang, G. Li, C. Jin, L. Ji, H. Chao. A GSH-activatable ruthenium(II)-azo photosensitizer for two-photon photodynamic therapy. *Chem. Commun*. 53: 1977-1980, 2017.

[22] G.-Y. Li, J-P. Liu, H. Y. Huang, Y. Wen, H. Chao, and L-N. Ji. Colorimetric and luminescent dual-signaling responsive probing of thiols by a ruthenium(II)-azo comple. *J. Inorg. Biochem*. 121:108-113, 2013.

[23] G. Li, Y. Chen, J. Wu, L. Ji, and H. Chao. Thiol-specific phosphorescent imaging in living cells with an azobis(2,2-bipyridine)-bridged dinuclear iridium(III) complex. *Chem. Commun.* 49: 20140-2042, 2013.

[24] H. Kimura, N. Shibuya, and Yuka Kimura. Hydrogen Sulfide Is a Signaling Molecule and a Cytoprotectant. *Antioxidants & Redox Signaling*, 17: 45-57, 2012.

[25] J. P. Marcolongo, A. Zeida, L. D. Slep, and J. A. Olabe. Thionitrous Acid/Thionitrite and Perthionitrite Intermediates in the "Crosstalk" of NO and H_2S. *Advances in Inorganic Chemistry*, 70: 277-309, 2017.

[26] C. A. Bignozzi, C. Chiorboli, M. T. Indelli, M. A. Rampi Scandola, G. Varani and F. Scandola. Simple poly(pyridine) ruthenium(II) photosensitizer: (2,2'-bipyridine) tetracyanoruthenate(II). *J. Am. Chem. Soc*. 108: 7872-7873, 1986.

[27] M. E. García Posse, N. E. Katz, L. M. Baraldo, D. Polonuer, C. Colombano, and J. A. Olabe. Comparative Bonding and Photophysical Properties of 2,2'-bipyridine and 2,2'-bipyrazine in Tetracyano Complexes Containing Ruthenium and Osmium. *Inorg. Chem.* 34: 1830- 1835, 1995.

[28] J. V. Caspar, E. M. Kober, B. P. Sullivan, and T. J. Meyer. Application of the energy gap law to the decay of charge-transfer excited states. *J. Am. Chem. Soc.* 104: 630-632, 1982.

Bio

Néstor E. Katz

Néstor E. Katz graduated as Doctor in Chemistry in 1978, with a thesis directed by Dr. Pedro J. Aymonino at UNLP. He completed his postdoctoral studies with Dr. Norman Sutin and Dr. Carol Creutz at BNL, USA, and with Dr. Thomas J. Meyer at UNC at Chapel Hill, USA. He has directed 8 doctoral theses and published 86 papers on the synthesis and properties of new coordination compounds of iron, cobalt, ruthenium, osmium and rhenium that are relevant to energy conversion and chemical sensing. He is Full Professor of Physical Chemistry at UNT, Principal Researcher at CONICET and Director of INQUINOA (CONICET-UNT).

Science Reviews
from the end of the world

Vol. 1, No. 2, March 2020 // pp. 45-65 /

Modulation of Functional Features in Electron Transferring Metalloproteins

Daniel H. Murgida

Instituto de Química Física de los Materiales, Medio Ambiente y Energía (INQUIMAE), Departamento de Química Inorgánica, Analítica y Química Física, Facultad de Ciencias Exactas y Naturales, Universidad de Buenos Aires and CONICET, Buenos Aires, Argentina.
E-mail: dhmurgida@qi.fcen.uba.ar ORCID: 0000-0001-5173-0183

Abstract

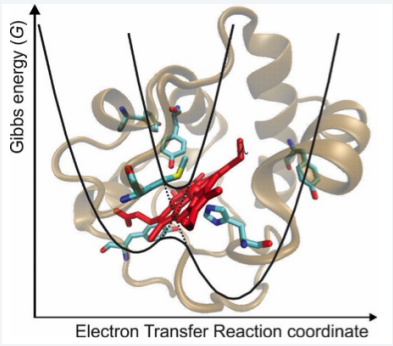

Electron transferring metalloproteins are typically implicated in shuttling electrons between energy transduction chains membrane complexes, such as in (aerobic and anaerobic) respiration and photosynthesis, among other functions. The thermodynamic and kinetic electron transfer parameters of the different metalloproteins need to be adjusted in each case to the specific demands, which can be quite diverse among organisms. Notably, biology utilizes very few metals, essentially iron and copper, to cover this broad range of redox needs imposed by biodiversity. Here, I will describe some crucial structural and dynamical characteristics that modulate the electron transfer parameters (and alternative functions) of two prototypical metalloproteins: the iron protein cytochrome *c* and its redox partner, the Cu_A center of the terminal respiratory enzyme cytochrome *c* oxidase. Specifically, I will focus on summarizing results obtained in recent years in my laboratory.

Keywords:
protein electron transfer, cytochrome *c*, copper A, metalloproteins, bioelectrochemistry, time-resolved SERRS spectroelectrochemistry.

Introduction

Electron transfer (ET) is the most elemental and one of the most ubiquitous chemical reactions in biology. Prototypical examples are the respiratory and photosynthetic ET chains that couple downhill ET reactions with uphill proton translocation across membranes to generate an electrochemical gradient that drives ATP synthesis. These processes often involve redox-active metal ions (and other cofactors) incorporated into a protein matrix (metalloproteins) as electron transporting or catalytic redox centers. The spectacular diversity of eukaryotic and prokaryotic life on Earth anticipates a wide palette of thermodynamic and kinetic redox needs to be covered by ET metalloproteins. Most surprisingly, nature employs very few metals, mainly iron and copper, to fulfill these divergent redox requirements,[1] thus indicating the existence of sophisticated ways of coarse and fine tuning of the relevant ET parameters, other than simply changing the redox active metal.

In this review, I will discuss these modulation mechanisms of thermodynamic and kinetic redox parameters for two specific cases: the (heme)iron protein cytochrome *c* (Cyt-c) and the copper protein Cu_A, which are redox partners in respiratory chains. The discussion is structured in terms of the modulation of individual parameters that, according to Marcus theory, determine ET efficiency.

The classical Marcus model relies on the transition-state theory and, therefore, assumes that reactants and solvent are in thermal equilibrium before the reaction.[2] The description is based on a two-state diagram where reactants and products are represented by intersecting free energy parabolas as a function of nuclear coordinates (Figure 1). Solvent thermal fluctuations eventually equalize reactants and products energy at the crossing point, thus enabling ET to render a product that is not yet equilibrated with the solvent. Note that this concept relies upon the underlying assumption that ET is much faster than solvent reorganization.

The parabolic shape of the two curves arises from the assumption that the medium can be described as an unsaturated dielectric continuum with linear polarization response. Both parabolas have identical curvature but are vertically and horizontally displaced with respect to each other, thus implying the following expression for the free energy of activation:

$$\Delta G^{\#} = \frac{(\Delta G^0+\lambda)^2}{4\lambda} \qquad \text{(Eq. 1)}$$

ΔG^0 is the thermodynamic driving force of the reaction (given by the difference of donor and acceptor reduction potentials, ΔE^0) and λ is the reorganization free energy, defined as the energy required for bringing the reactants from their equilibrium configuration to the equilibrium configuration of the products without actually transferring electrons (Figure 1).

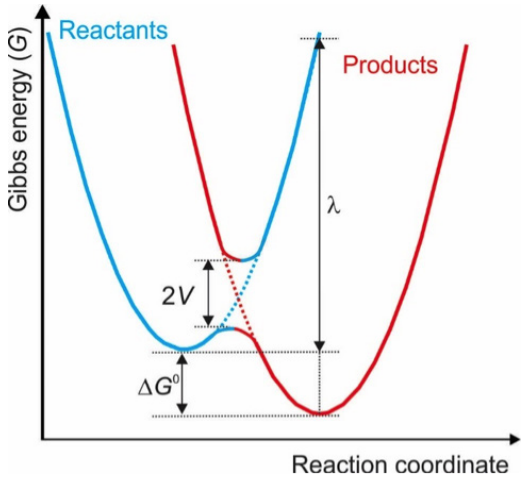

Figure 1. Energy diagram for electron transfer reactions according to Marcus model.

The introduction of quantum mechanical considerations to account for the possibility of classically forbidden electron tunneling leads to the most popular expression in protein ET, i.e. the high temperature limit of Marcus semiclassical expression for non-adiabatic ET reactions:

$$k_{NA} = \frac{2\pi V^2}{\hbar\sqrt{4\pi\lambda k_B T}} exp\left(\frac{-(\lambda+\Delta G^0)^2}{4\lambda k_B T}\right) \qquad \text{(Eq. 2)}$$

The pre-exponential term in Eq. 2 is the result of using Landau-Zerner theory for estimating the ET probability after one passage through the crossing point. Derivation of this expression recognizes that solvent (stochastic) fluctuations can be treated classically as they occur with low frequencies and, therefore, only high frequency vibrational modes of reactants and products need to be treated quantum-mechanically. Thus, assuming spherical ions in a polarizable continuum solvent, the reorganization energy can be separated into two contributions, $\lambda = \lambda_{vib} + \lambda_s$. Here λ_{vib} (also known as λ_{in}) corresponds to the reorganization of the redox active molecules, which can be estimated from the high frequency vibrational modes of reactants and products, whereas λ_s (also known as λ_{out}) accounts for the solvent reorganization and is estimated classically. Note that the dependence of k_{NA} with ΔG^0 leads to different regimes: the so-called normal, barrierless and inverted regions, which correspond to $0 \leq -\Delta G^0 \leq \lambda$, $-\Delta G^0 = \lambda$ and $-\Delta G^0 > \lambda$, respectively. Parameter V is the matrix element for the electronic coupling between reactant and product states, and its magnitude determines whether the ET reaction proceeds adiabatically or non-adiabatically. For sufficiently large V values (> 0.025 eV), the strong interaction

of the two parabolas results in two adiabatic surfaces separated by a magnitude $2V$ at the intersection point (Figure 1). In this case, the reaction evolves adiabatically along the lower surface trough the transition state and, therefore, its rate is independent of the value of V and limited by the probability of reaching the transition state. In the opposite limit of weak coupling (non-adiabatic ET), reaction rate is determined by the electron tunneling probability at the intersection point which, according to Eq. 2, scales with V^2.

In protein ET reactions, donor-acceptor distances are typically very long (> 10 Å), which results in very weak electronic couplings (see below) and, therefore, most experimental studies are rationalized in terms of Marcus semiclassical expression for non-adiabatic ET (Eq. 2). While this is certainly correct for most *in vitro* studies performed with diluted aqueous solutions (viscosity ≈ 1 *cP*), *in vivo* behavior can be drastically different since, for example, intracellular viscosities can be up to 500 times higher; therefore, long-range protein ET reactions are likely to be friction-controlled in spite of the weak coupling.[3,4]

As mentioned above, the electronic coupling matrix element V is a measure of the strength of interactions between reactants and products at the nuclear configuration of the transition state. For a precise description of V in proteins (and macrobiomolecules in general) it is necessary to account for its dependence on the distance between redox centers, on the dielectric properties and atomistic description of the insulating (or conducting) material in between, and on fluctuations of electronic and structural parameters at different levels and time-scales of the multidimensional and hierarchical free energy landscapes that characterize macromolecules. In a zero-order approach, one can approximate the medium that separates donor and acceptor as homogeneous and, therefore, the ET reaction can be treated in terms of a square barrier tunneling model. This assumption leads to an exponential decay of V as a function of the donor-acceptor distance r and of a medium-specific decay constant β:

$$V(r) = V(r_0)exp\left(-\frac{1}{2}\beta(r - r_0)\right) \qquad \text{(Eq. 3)}$$

To account for the structural complexity of proteins, Beratan and coworkers developed an extension of McConnell superexchange model, the so-called tunneling-pathway model.[5] In this approach, the medium between partner redox sites is broken into small subunits connected by covalent bonds, H-bonds and through space jumps, which differ in their ability to mediate coupling. Thus, the total coupling for a given pathway is estimated as a product of the couplings for the individual elements. The dependency expressed in Equation 3 remains valid, but the coupling decay parameter is now determined by the structural elements encountered along the pathway and, thus, the geometric donor-acceptor distance is replaced by an effective tunneling path length distance σ. Subsequent refinements retain some central points of the extended superexchange model, but incorporate more detailed and quantitative descriptions, particularly with regard to ultrafast dynamics.

The expressions discussed above refer to ET reactions between molecular redox partners. The description of electrochemical experiments of redox proteins is somewhat different, since one of the species involved is a solid electrode that can play the role of either donor or acceptor. In the case of redox species immobilized on the surface of metal electrodes, Marcus semiclassical expression needs to be integrated to account for all electronic levels in the metal:

$$k_{NA} = \frac{2\pi}{\hbar}V^2 \int_{-\infty}^{\infty} \frac{1}{1+\exp\left(\frac{\epsilon-\epsilon_f}{k_BT}\right)} \rho(\epsilon) \frac{1}{\sqrt{4\pi\lambda k_BT}} \exp\left[-\frac{(\lambda - e\eta + \epsilon)^2}{4\lambda k_BT}\right] \qquad \text{(Eq. 4)}$$

Note that in this case the reaction driving force can be set to the desired value (and sign) through the overpotential $\eta = E - E^0$, where E and E^0 represent the applied electrode potential and the redox potential of the molecular species, respectively. ρ is the density of electronic states in the electrode, the last term of the integrand is the Fermi-Dirac distribution law, ϵ_f is the energy of the Fermi level, and the remaining symbols have the usual meaning. This expression can be simplified by approximating the Fermi-Dirac distribution law as a step function:

$$k_{NA} \approx \frac{\pi}{\hbar}V^2 \,\mathrm{erfc}\left(\frac{\lambda + e\eta}{\sqrt{4\lambda k_BT}}\right) \qquad \text{(Eq. 5)}$$

In the following sections I will discuss, in relation to the specific cases of Cyt-c and Cu_A, the structural and dynamic features that modulate the relevant parameters that appear in equations 1 to 5, i.e. E^0, V and λ, and thereby the efficiency

of ET reactions in these proteins, as well as the regulation mechanisms that are beyond the scope of Marcus semiclassical theory.

1. Multifunctional cytochrome *c*

Mitochondrial cytochrome *c* (Cyt-c) is a globular and water-soluble monohemic protein that has an average size of 104 ± 10 amino acid residues, i.e. about 13 kDa, depending on the organism. The typical Cyt-c fold consists of five α-helices of different lengths interconnected by extended Ω loops, and a couple of short two-stranded antiparallel β-sheets (Figure 2). The slightly saddled heme group is covalently attached to two cysteine residues and buried into a hydrophobic pocket, with only one edge partially exposed to the solvent. The four N atoms of the porphyrin ring coordinate the iron ion equatorially, while residues His18 and Met80 serve as proximal and distal axial ligands, respectively.[6]

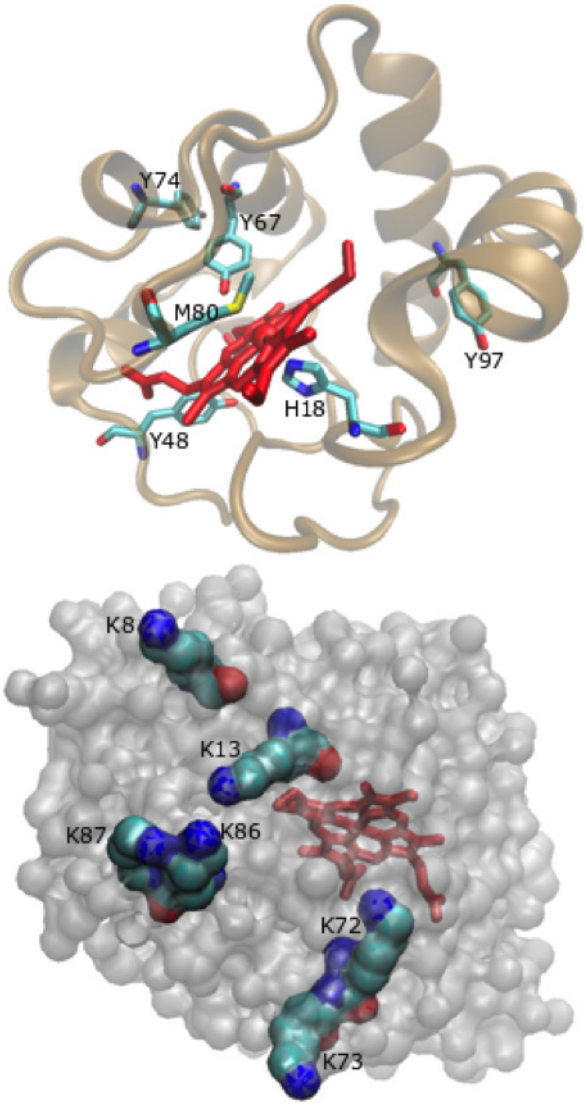

Figure 2. Crystal structure of horse heart ferric cytochrome *c* (PDBid 1HRC).[7] The top view shows the secondary structure elements, the two axial ligands and crucial tyrosine residues. The bottom view shows six surface lysine residues that constitute the binding site to natural redox partners and to negatively charged surfaces in general.

A comparison of crystallographic and NMR structures of the ferric and ferrous forms of Cyt-c indicate only subtle redox-linked conformational changes, which are mainly localized in the hydrogen-bonding network that involves one of the heme propionates, two crystallographic buried water molecules and side chains of several residues mainly on

the distal side. Spectroscopic studies, on the other hand, suggest higher flexibility of the ferric protein, which has been postulated as a key feature for regulating binding and dissociation to redox partners.

The structure described above corresponds to the so-called native conformation of Cyt-c, whose canonical function within the intermembrane space of mitochondria is shuttling electrons from complex III to the terminal respiratory enzyme cytochrome *c* oxidase (CcO), thus critically contributing to sustain cellular life. It should be noted, however, that Cyt-c behaves as a moonlighting protein, meaning that the actual function may change upon intracellular relocalization or post-translational modifications.[8] In response to aggressions such as DNA damage or metabolic stress, cells may activate complex and ordered sequences of cell suicide, known as apoptotic pathways. One of these sequences involves the release of mitochondrial Cyt-c into the cytosol. After the relocalization, Cyt-c forms a complex with the cytosolic protein Apaf-1, which triggers a cascade of caspase activation events that ends up in cellular death. Moreover, once in the cytosol Cyt-c may translocate into the nucleus in response to DNA damage and block cell survival by impeding nucleosome assembly. Interestingly, Cyt-c can be the architect of its own liberation to the cytosol through the permeabilization of the mitochondrial membrane. In this case, the interaction of the protein with the membrane component cardiolipin (CL) induces a conformational transition that results in the gain of peroxidatic activity towards CL.[9] Post-translational modifications of Cyt-c observed under oxidative stress conditions may either favor the gain of peroxidatic activity or interfere with the binding to CL and Apaf-1, suggesting a complex interplay of pro- and antiapoptotic stimuli.[6,8–11] Translocation mechanisms and the conformational details associated to each alternative function of Cyt-c remain largely unknown, but there is certain consensus that the conserved structural flexibility of this protein is central to its tunable functionality.

1.1. Redox thermodynamics of Cyt-c

Redox potentials (E^0) of type *c* cytochromes in general (including eukaryotes, bacteria and archaea) cover a very broad range from ca. -500 mV to 500 mV, thus highlighting the tunability of the common metalloporphyrin redox active site.[6] A careful inspection of the structural differences between cytochromes allows dissecting the main structural determinants and their relative contributions to E^0, as schematically summarized in Figure 3.

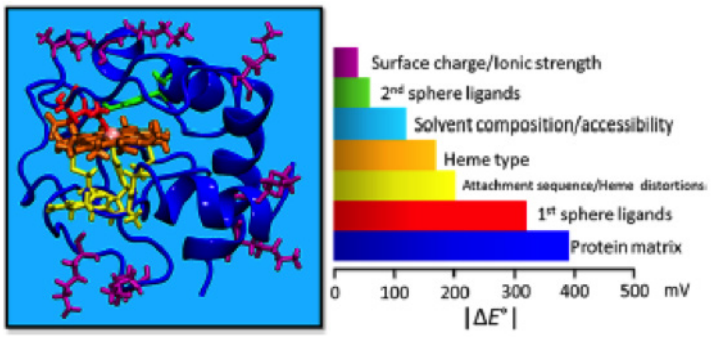

Figure 3. Structural elements that contribute to different extents to tune the redox potential of Cyt-c. Adopted from reference 6 with permission. Copyright 2017, American Chemical Society.

The first coordination sphere of the metal ion is probably the most crucial determinant of E^0. Thus, the tetradentate equatorial ligand has a strong influence on the differential stabilization of Fe^{2+} versus Fe^{3+}, which in turn is syntonized by the electron donation/withdrawing properties of the porphyrin substituents. An even stronger effect is exerted by the axial ligands, Met80 and His18 in native Cyt-c. The π-electron-acceptor character of the thioether sulfur atom in Met80, as well as the burial of the heme within a hydrophobic pocket and its concomitant poor solvent accessibility, stabilizes Fe^{2+} relative to Fe^{3+}. Therefore, the detachment of Met80 and the increased solvent accessibility that characterizes most alternative conformations of Cyt-c results in large downshifts of E^0 of up to 400 mV, which can be partially ascribed to the loss of Fe^{2+} stabilization.[8,12–14] Under these conditions, Cyt-c is unable to efficiently shuttle electrons in the respiratory chain, but instead acquires redox and structural characteristics typical of a peroxidase.

The heme moiety is embedded in a largely fluctuating amino acidic matrix that may dynamically modulate the electronic properties of the site through specific first and second sphere interactions, through the local electrostatic potential, and by imposition of deformation of the tetrapyrrol from planarity. Thus, the thermodynamic and kinetic redox parameters

of Cyt-c are sensitive to changes in a number of structural elements, which in turn can be affected by interactions with redox partners in reactive complexes, by the nature and ionic composition of the solvent as well as by pH and temperature.

1.2. Kinetic electron transfer parameters of Cyt-c

Given that most protein ET reactions occur under very small thermodynamic driving forces (ΔG^0~0), metal redox centers have structurally evolved in order to minimize λ, thereby maximizing the ET rate. In the case of Cyt-c, experimental evidence points out that the same structural features that optimize E^0 (see section 1.1) are also responsible for minimizing λ, as essentially every structural perturbation of the WT protein results in a rise of this parameter. For example, replacement of the axial ligand Met80 by an exogenous pyridinil ligand, or its mutation for a non-coordinating alanine residue, leads to a ca. two-fold increase of λ.[15] A similar effect is observed upon addition of urea due to augmented solvent exposure of the metal site in the partially unfolded protein.

Interestingly, electrostatic interactions of Cyt-c with model systems have also been found to modulate the magnitude of λ.[16,17] Computational and experimental studies demonstrated that Cyt-c utilizes a patch of positively charged Lys residues that surround the partially exposed heme edge for electrostatic binding to partner proteins, such as Cyt-c oxidase, reductase and peroxidase. The same set of Lys residues was found to constitute de binding site to metal electrodes coated with self-assembled monolayers (SAMs) of carboxyl-terminated alkanethiols, thus validating the use of these simplified model systems for assessing the effect of electrostatic interactions on ET parameters.[18,19] The use of these simple SAM/Cyt-c models presents a number of important advantages: (a) the protein adsorbs with the heme edge facing the SAM, which allows for efficient direct electrochemistry; (b) surface confinement prevents diffusional control, thus facilitating the determination of relevant kinetic parameters; (c) the electrode functions as either electron donor or acceptor and the ET driving force can be tuned trough the electrode potential; (d) the electronic coupling can be easily varied though the chain length of the alkanetiols; (e) the interfacial electric field can be systematically varied trough parameters such as electrode potential, chemical composition of the SAM (i.e. density of charged head groups and chain lengths), pH and ionic strength. It has been demonstrated, both theoretically and experimentally, that the interfacial electric fields in these model systems are of the same magnitude as in biological membranes.[12,20–22] Furthermore, if the surfaces of the Au or Ag electrodes are nanostructured previous to the SAM-coating process, these modified surfaces behave as suitable platforms for surface-enhanced (resonance) Raman (SER/SERR) detection of the adsorbed Cyt-c.[13,23] Thus, thermodynamic and kinetic ET parameters can be obtained from spectral deconvolution of stationary or time-resolved potential-dependent SERR measurements, respectively. This methodology has the advantage over conventional electrochemical techniques of providing real time structural information of the immobilized protein under reactive conditions. Moreover, the method allows obtaining a precise determination of λ from the overpotential dependence of the ET rate constant measured by TR-SERR at constant temperature (see Eq. 5). This type of experiments revealed that the reorganization energy of Cyt-c electrostatically adsorbed on COOH-terminated SAMs under conditions that preserve the native structure is only a half of the value determined for the WT protein in solution, i.e. 0.3 and 0.6 eV, respectively. In contrast, the Tyr67Phe mutant, which lacks the native Tyr67-Met80 hydrogen bonding interaction, yields λ = 0.3 eV irrespectively of the interfacial electrostatic field.[17] These results, in combination with molecular dynamic simulations, revealed that the local electrostatic field induces subtle deformations of the flexible Ω loops that contain most of the Lys residues that constitute the protein binding site. Such minor distortions neither represent a measurable change of secondary structure nor affect the first coordination sphere of the heme iron. However, they affect the H-bonding network to some extent, thus altering the interactions between first and second coordination sphere residues. Most notably, electrostatic interactions disrupt the Tyr67-Met80 H-bond in a similar fashion as the Tyr67Phe mutation, which results in the minimization of λ without affecting E^0.[17] Based on these findings, it was proposed that a similar electrostatically driven switch between Cyt-c native forms of high and low λ might also be triggered upon a binding of Cyt-c to the natural redox partners. I will come back to this important point in section 3.

Interestingly, the finding that Cyt-c may exist in two alternative native forms that differ in λ and whose interconversion is driven by the electrostatic field allows rationalizing the large dispersion of λ values reported in the literature for type *c* cytochromes. Indeed, the average λ taken over all values reported for Cyt-c samples from different organisms in solution (i.e. with no field applied) is ca. 0.6 eV. This average number drops to ca. 0.3 eV when taken over electrostatic complexes of Cyt-c. Moreover, the different Cyt-c variants reported so far can be classified into high and low λ forms depending on the presence or absence of the Tyr67−Met80 H-bond, respectively.

Residue Tyr67 is not only crucial for regulating λ, mutation of this residue has also been found to significantly affect the electronic coupling (V) between the heme group and an artificial redox probe. This is true even for the conservative Tyr67Phe mutant, for which simple pathways calculations do not predict significant differences, but quantum mechanical calculations predict that altered dynamics of the aromatic ring translate into lower V due to less favorable orbital overlap

between the aromatic ring of Tyr67 and the heme.[24] Another factor that has been proposed to affect *V* is the heme ruffling, since increasing out-of-plane distortion decreases delocalization of the Fe $3d_{\pi}$-based molecular orbitals onto the β-pyrrole carbons.[25] In addition to these fine-tuning mechanisms, the most important determinants of the electronic coupling between Cyt-c and its redox partners are the structure and dynamics of the inter-protein complexes, as highlighted by electrochemical and spectroelectrochemical experiments of Cyt-c immobilized on SAM-coated electrodes.[18,19,26–30] The electrochemical determination of apparent ET rate constants (k_{ET}^{app}) for Cyt-c and other redox proteins adsorbed on variable thickness SAMs revealed distance dependencies that cannot be explained in terms of Marcus theory.[31] This behavior is characterized by the expected exponential decay of k_{ET}^{app} with the Cyt-c/electrode distance (number of -CH_2- groups in the SAMs) only for alkanethiols with more than 10 -CH_2- groups, with a coupling decay constant consistent with a reaction rate limited by through-bond electron tunneling probability ($\beta \approx 1$ per -CH_2- group). For thinner SAMs, in contrast, k_{ET}^{app} has much softer distance dependence and tends to plateau. This change of ET regime for electrostatically adsorbed Cyt-c was investigated by time-resolved surfaced-enhanced resonance Raman (TR-SERR) spectroelectrochemistry taking advantage of the surface selection rules, which allow for monitoring the coarse reorientation of Cyt-c simultaneously with its redox state and heme pocket structure.[26] The experiments revealed a dynamic behavior (rotational diffusion) of the adsorbed Cyt-c molecules. In thicker SAMs, this motion is four orders of magnitude faster than the redox reaction, thus confirming a non-adiabatic ET mechanism at these tunneling distances. In thinner SAMs, protein reorientation rate is slowed down drastically and becomes similar to k_{ET}^{app}, indicating that the overall redox reaction rate is limited by protein reorientation. Interestingly, molecular dynamics simulations combined with pathways calculations reveal that the most stable orientation of Cyt-c in the electrostatic complex does not provide an efficient pathway for heterogeneous ET (Figure 4), thereby suggesting that protein reorientation is a prerequisite for the reaction.[18,19]

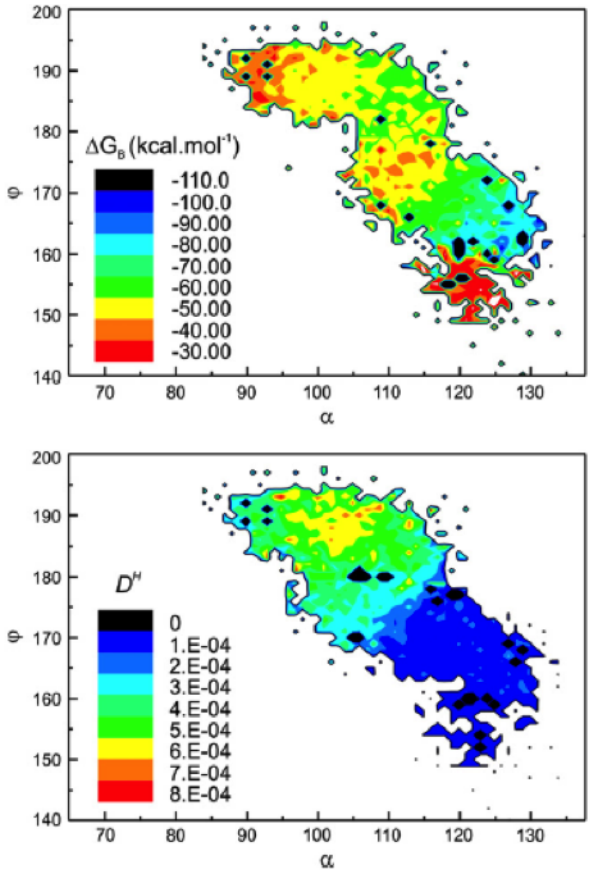

Figure 4. Binding energy (top) and electronic coupling of Cyt-c adsorbed on electrodes coated with COOH-terminated SAMs as a function of angles α and ϕ, which define the orientation of the heme with respect to the electrode surface. Note that optimal binding is achieved for (α, ϕ) values around (128, 165), while optimal coupling requires reorientation to values around (105, 188). Adopted from reference [32] with permission. Copyright 2014, Elsevier B.V.

Thinner SAMs imply higher tunneling probabilities but also higher local electric fields that slow down protein reorientation. Thus, upon shortening the chain length of the SAMs, the redox process becomes kinetically gated by reorientational dynamics. In agreement with this interpretation, mutation of the key amino acid Lys87 (Lys87Cys mutant), which stabilizes low-coupling orientations, results in the recovery of an exponential distance dependence of k_{ET}^{app} for all chain lengths.[30] In addition to coarse protein orientation, subtle fluctuations such as the movement of interfacial water molecules and side-chain rearrangements may also have a deep impact on coupling. Indeed, cross-linking of Cyt-c to the SAMs results in fixed coarse orientation and hindered protein reorientation, but the anomalous distance dependence is still verified, suggesting that both coarse and fine dynamics are strongly affected by interfacial electric fields of biologically relevant magnitude.[28] The potential biological impact of these findings will be discussed in section 3.

A different explanation for the unusual distance-dependence of k_{ET}^{app} consists of a changeover of ET regime from non-adiabatic at long distances to friction control at the thinner SAMs. The experimental signature of the friction control regime is a viscosity-dependent k_{ET}^{app}, which, however, is also expected in the case of a gating step such as protein reorientation. An elegant strategy to suppress reorientation is direct wiring of the heme iron to the electrode by using SAMs that include pyiridinil-terminated alkanethiols, which have been shown to displace the native Met80 ligand.[33] For these systems, a gating step in the plateau region (thinner SAMs) can be safely discarded as the value of k_{ET}^{app} measured at constant temperature by TR-SERR displays a clear dependence with the applied overpotential, yielding λ values above 0.5 eV.[15] This behavior contrasts with the flat overpotential dependence of k_{ET}^{app} for Cyt-c electrostatically adsorbed on thin SAMs with high negative charge density.[13] Thus, the most likely scenario is that both electric-field-modulated large and small amplitude motions (i.e., a reorientation, water rearrangement, etc.) and the onset of friction control may both play a role in regulating the kinetic behavior of Cyt-c depending on the specific conditions.

1.3. Redox coupled conformational changes of Cyt-*c*

In the preceding sections, I have centered the discussion around the canonical electron shuttling function of Cyt-c that is associated with the so-called native protein structure, i.e. the one derived from crystallography at neutral pH. It should be noted, however, that this static picture corresponds to a minimum of a multidimensional free energy landscape that includes other sub-states that are energetically accessible at physiological temperatures. Moreover, a number of environmental conditions may alter either the free energy landscape or the conformational diffusion parameters that determine landscape exploration.[6,8] In the mitochondrial intermembrane space, such conditions include crowding effects, local electric fields and altered local pH values, as well as specific and unspecific protein-protein and protein-lipid interactions. These effects may be crucial in fine-tuning ET parameters, but may also result in alternative Cyt-c conformations with different functionalities. Indeed, it has been extensively demonstrated that these types of perturbations affect Cyt-c structure in different ways, but always including the disruption of the Met80-Fe bond as one of the primary events.[6,8,9,14,34] Additionally, the disruption of this bond under mild perturbation has been found to take place preferentially in ferric Cyt-c, and only rarely in the ferrous protein. This difference has long been ascribed to the lower strength of Fe^{3+}-S(Met) compared to Fe^{2+}-S(Met). Recent resonance inelastic X-ray scattering studies, however, demonstrated the opposite trend in redox state-dependent bond strengths, and indicated that 50% of the bond stabilization in the ferric protein arises from contributions of the protein scaffold, probably involving the network of H-bond interactions.[35,36] Consistent with this, quantum mechanical calculations show that the experimentally observed disruption of the same bond by biologically meaningful external electric fields cannot be ascribed to a field-induced weakening of the bond.[37] Instead, simulations show that exposure to moderate electric fields results in distortion and increased flexibility of crucial protein segments due to polarization and alignment with the field.[38] Moreover, calculations show that the application of electric fields favors the pentacoordinated form both energetically and entropically, and also lowers the activation barrier of the process.

The most thoroughly studied alternative conformation of Cyt-c is the so-called alkaline form, whose main characteristic is the replacement of the axial Met80 ligand by a surface Lys residue to produce a six-coordinated low spin (6cLS) conformation with Lys/His axial coordination pattern.[6,8] For the most studied equine Cyt-c, this transition has a $pK_a = 9.4$ and the distal axial ligand at $pH > pK_a$ can be either Lys79 or Lys73. Structural models show that the largest structural differences of the alkaline conformation with respect to native Cyt-c are localized in the regions that exhibit increased conformational dynamics in the ferric protein with respect to the ferrous one, which may explain why the alkaline transition is only observed for oxidized Cyt-c.[39,40] In the alkaline conformation, the redox potential is downshifted by 300 mV, rendering the protein unable to function as electron shuttle.[14] This change is accompanied by a gain of peroxidase activity, most likely ascribable to a dynamic equilibrium with minor amounts of five-coordinated high-spin species.[10] In this respect, the alkaline transition represents a paradigmatic case of function gaining. The minimal mechanism for the transition includes deprotonation of an unknown triggering residue, followed by ligand exchange.

Recent TR-SERR studies identify Lys73 as the most likely triggering group and show that electrostatic interactions of Cyt-c with biomimetic surfaces shift the pK_a of the transition to even higher values.[14] Thus, the unphysiologically high pK_a of this process makes the alkaline conformation interesting for basic biophysical studies, but unlikely to be biologically relevant. Recent findings, however, show that certain post-translational modifications and naturally occurring mutations of mammalian Cyt-c have the effect of downshifting the pK_a of the alkaline transition towards physiological pH, making this process potentially relevant *in vivo*.[6,8] One of these modifications is naturally occurring Tyr74 nitration, which results in deprotonation of the phenolic ring at neutral pH, concomitant with Met → Lys axial ligand exchange with pK_a values of 7.1 and 8.9 for the protein free in solution and electrostatically adsorbed on SAM-coated electrodes, respectively.[10,41] Computational studies suggest that the change of electrostatic field caused by deprotonation of nitro-Tyr74 as triggering event stabilizes the Lys/His form relative to the intermediate pentacoordinated species, thereby increasing the activation barrier for the inverse Lys → Met ligand exchange,[10] as also experimentally verified by TR-SERR.[14]

The alkaline conformation is only one of many alternative conformations reported for Cyt-c. A large number of studies have demonstrated that, even at neutral pH, electrostatic interactions of Cyt-c with a variety of negatively charged model systems – including phospholipid vesicles, micelles, polyanions, and others – induce conformational changes that involve the disruption of the labile Met80-Fe bond, mainly in the ferric form.[6,34] As a result of these interactions, the distal axial position may remain vacant, leading to a penta-coordinated high-spin species (5cHS; with His18 proximal coordination), or be occupied by either His26 or His33, leading to a hexa-coordinated low-spin form (6cLS; with His23,33/His18). Eventually, and depending on the specific conditions, small amounts of a hexa-coordinate high-spin form with H_2O/His18 axial coordination can also be found.[34] These alternative conformations have very low redox potentials compared to the native form, and are often referred to as B2 conformations.[42] Systematic studies have shown that the amount of B2 forms in equilibrium with the native conformation correlate with the strength of the interfacial electrostatic field in the complexes.[12]

The interaction of Cyt-c with cardiolipin (CL) containing liposomes is particularly relevant, since CL is the only anionic phospholipid present in the inner and outer mitochondrial membranes. Actually, about 15 % of the mitochondrial Cyt-c is bound to CL in healthy cells. The binding of Cyt-c to CL has been extensively studied, but with contradicting results regarding the heme structure in the complexes.[9,43] Recent resonance Raman studies demonstrated that the interaction of native Cyt-c with CL induces a ligand exchange to produce a B2 species with His/His axial coordination pattern, where the proximal position is occupied by the native His18 ligand, and the distal one corresponds to either His33 or His26 (Figure 5).[9] Interestingly, this CL-induced transition is not restricted to native Cyt-c. Alternative conformations of Cyt-c, such as those with Lys/His and OH^-/His axial coordination patterns stabilized by post-translational Tyr74 nitration and Met80 sulfoxidation, respectively,[10,11] also lead to spectroscopically identical His/His species (Figure 5).[9]

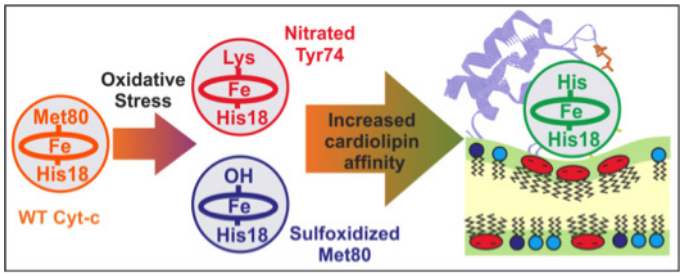

Figure 5. Schematic representation of cardiolipin-induced conformational changes of wild type Cyt-c and post-translationally modified forms of the protein. Adopted from reference[9] with permission. Copyright 2015, American Chemical Society.

The His/His alternative conformation presents an apparent peroxidase activity 15 times higher than the Met/His native form, and twice larger than the Lys/His and OH^-/His conformations. This activity is ascribed to the lability of the distal His ligand in the His/His complex, which is in equilibrium with small but detectable amounts of enzymatically competent high spin species. Moreover, the nitration of Tyr74 and sulfoxidation of Met80 result in a 4-fold enhancement of the binding affinity of Cyt-c to CL, suggesting that these translational modifications amplify the pro-apoptotic signal.[9] Moreover, it was recently shown that inorganic and organic phosphate anions efficiently mediate the binding of Cyt-c to the abundant zwitterionic lipids in membrane phosphatidylcholine and phosphatidylethanolamine. In these complexes, Cyt-c reacts efficiently with H_2O_2 at submillimolar levels, which oxidizes the sulfur atom of the axial ligand Met80.[11] Thus, the rise of H_2O_2 to submillimolar concentrations that characterizes the early stages of apoptosis produces a post-translational

modification of Cyt-c with enhanced affinity for CL and enhanced CL-peroxidase activity, thus facilitating membrane permeabilization as a crucial part of the apoptotic program.

2. Cytochrome *c* oxidase

Cytochrome *c* oxidase (CcO), also known as respiratory complex IV, is an integral membrane protein that serves as terminal electron acceptor in aerobic respiratory chains in mitochondria and bacteria. The enzyme accepts four electrons from Cyt-c and employs their excess free energy to translocate four protons across the membrane, thus contributing to generate the electrochemical gradient that drives ATP synthesis. Finally, electrons are transferred to the sacrificial acceptor O_2, producing H_2O as a by-product. The size and detailed structure of CcO is organism-dependent, but all canonical enzymes contain two copper and two heme centers. A Cu_A site accepts electrons from Cyt-c redirecting them to a heme *a* or *b* cofactor, and from there to the heme a_3 / Cu_B binuclear site, where O_2-reduction is catalyzed. Mammalian CcO enzymes are large and complex structures composed of 13 subunits. In contrast, bacterial enzymes are largely simplified versions that typically contain only 4 subunits, with the three largest subunits (I, II and III) highly homologous to the mitochondrion-encoded components that form the catalytic core of the enzyme. For example, the ba_3-CcO from *Thermus thermophilus* is a 85 kDa membrane integral protein complex that features three subunits forming a bundle of 15 transmembrane helices. From these helices, 13 belong to the large subunit I, which contains hemes *b* and a_3, as well as Cu_B, while subunit II is composed of a transmembrane helix and the Cu_A-containing periplasmic domain (Figure 6). The high homology verified at the levels of subunits I and II renders bacterial complexes as suitable model systems of the more complex eukaryotic enzymes.

In the following sections, I will focus on the primary electron acceptor in CcO, i.e. the Cu_A-containing protein fragment in subunit II, with some emphasis in recent results obtained with the fragment from *Thermus thermophilus* ba_3-CcO (*Tt*-Cu_A hereafter).

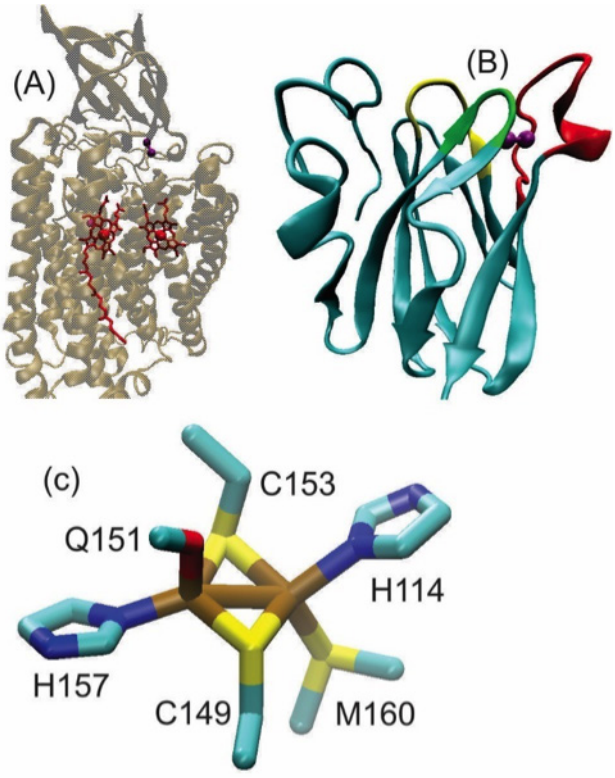

Figure 6. Crystal structures of the ba_3 CcO from *Thermus thermophilus*. (a) Structure of the integral enzyme (PDBid 3EH5).[44] (B) Cu_A-containing soluble fragment in subunit II (PDBid 2CUA). (C) Detailed view of the Cu_A site (PDBid 2CUA).[45]

2.1. Structure and electronic properties of Cu_A

The Cu_A site constitutes the primary electron acceptor of most eukaryotic and prokaryotic CcO enzymes, as well as of N_2O-reductases involved in the nitrogen cycle. It functions as a highly efficient redox hub that redirects the electrons provided by a soluble redox shuttle by nearly 90°, thus linking inter- and intramolecular ET reactions.

The structure of Cu_A is highly conserved and features two copper ions bridged by two Cys ligands forming a nearly planar Cu_2S_2 diamond core structure. Both coppers are further coordinated by one equatorial His strong ligand and by one weak axial ligand, a Met sulfur and a backbone carbonyl, respectively (Figure 6). The metal ions are surrounded by three loops of conserved length that contain the also conserved ligand set and differ among species in the noncoordinating residues only.[45]

Despite containing two copper ions, Cu_A behaves as a one-electron redox couple alternating between a paramagnetic and fully delocalized mixed-valence pair $Cu^{1.5+}$–$Cu^{1.5+}$ and a diamagnetic reduced state, Cu^{+}–Cu^{+}. This property can be ascribed to the unique metal–metal bond found in Cu_A, which has a length of ca. 2.4-2.5 Å. The resulting delocalized unpaired electron in the oxidized center is coupled with two equivalent copper ions with nuclear spin I = 3/2, which produces a characteristic seven-line hyperfine splitting pattern in the EPR spectra.[46]

Oxidized Cu_A is purple as a result of two intense absorbance bands at ca. 480 and 530 nm assigned to S(Cys)→Cu charge transfers, and a broad band at ca. 760–800 nm assigned to intervalence charge transfer. Reduced Cu_A, in contrast, is colorless due to the d^{10} electronic configuration of both copper ions.

The electronic structure of the $Cu^{1.5+}$–$Cu^{1.5+}$ site has been described in terms of an adiabatic double-well potential energy surface as a function of small geometric perturbations such as the Cu-Cu distance. The lower energy well is associated to a molecular orbital description featuring a σ_u* highest occupied molecular orbital (HOMO), and corresponds to the crystallographic Cu-Cu distance of about 2.4 Å. The second well is slightly more energetic but still thermally accessible, and it is associated to an elongated metal-metal bond and to a π_u HOMO symmetry.[47] Because of their thermal interconversion, the two wells are often designated as σ_u* and π_u alternative electronic ground states (GS), and the energy difference between them is the energy gap $\Delta E_{\sigma_u^*/\pi_u}$. Quantum mechanical calculations show that, in addition to Cu-Cu stretching, other perturbations, such as dihedral distortions or the application of biologically meaningful electric fields, may also affect $\Delta E_{\sigma_u^*/\pi_u}$ and, therefore, the relative populations of both GS.[48]

Because of the overlapping spectroscopic features of the multiple metal centers in N_2O-reductases and CcO enzymes, the detailed physicochemical characterization of Cu_A centers requires simplified model systems. Two important strategies along these lines are (i) producing truncates of native CcO proteins containing intact Cu_A sites and (ii) engineering artificial Cu_A sites into small soluble proteins. The most extensively studied examples in each case are the Cu_A-containing soluble fragment of the ba_3-CcO from *Thermus thermophilus* (*Tt*-Cu_A) and the Cu_A site engineered into azurin from *Pseudomonas aeruginosa* (*Pa*-Azu-Cu_A).[1] The first model, *Tt*-Cu_A, is particularly appealing because it is highly stable and, according to the available structural and spectroscopic characterization, it retains all the characteristic features of the Cu_A site in the integral enzyme and, therefore, can be regarded as a native Cu_A center. In recent years, the *Tt*-Cu_A site has been engineered to produce a variety of mutants at different structural levels to introduce perturbations that help elucidating the structural basis of the functional features. The different *Tt*-Cu_A variants produced are summarized in Table 1.

Table 1. Cu_A chimeras constructed by either single or multiple mutations of *Tt*-Cu_A at the level of the three loops that surround the metal site (see Figure 6)

Modification	Name	Loop 1 (86-89)	Loop 2 (110-115)	Loop 3 (149-160)	E^0 (mV)
None (wild type)	*Tt*-Cu_A	FAFG	PDVIHG	CNQYCGLGHQNM	261
1st sphere mutants	M160H	FAFG	PDVIHG	CNQYCGLGHQNH	79
	M160S	FAFG	PDVIHG	CNQYCGLGHQNS	177
	M160Y	FAFG	PDVIHG	CNQYCGLGHQNY	316
	M160L	FAFG	PDVIHG	CNQYCGLGHQNL	314
	M160Q	FAFG	PDVIHG	CNQYCGLGHQNQ	93
2nd sphere mutant	*Tt*-1L-E	HQWY	PDVIHG	CNQYCGLGHQNM	297
	Tt-1L-L	FAFG	PDVIHG	CSEICGANHSNM	226
	Tt-3L-*Hs*	HQWY	QDVLHG	CSEICGANHSNM	242
	Tt-3L-*At*	HQWY	SADVLHG	CSEICGTNHAFM	241
1st + 2nd sphere mutations	*Tt*-3L-M160H	HQWY	QDVLHG	CSEICGANHSNH	74

As modification of the strong Cys and His ligands of the Cu_A site are known to be disruptive, first coordination sphere modifications were restricted to the replacement of the weak axial ligand Met160 by a variety of amino acids.[3,48–54] Second sphere modifications, on the other hand, were accomplished by replacement of either one or the three loops that surround the metal site (Figures 6 and Table 1) by the homologous sequences from *Homo sapiens* and *Arabidopsis thaliana* with preservation of the conserved ligand set.[50,54] Moreover, combined first and second coordination sphere modification was achieved by introducing the Met160His point mutation in the so-called *Tt*-3L-*Hs* chimera.[53] In all cases, the generated proteins were characterized by a variety of spectroscopic methods such as UV-vis, EPR, NMR, RR and EXAFS, which demonstrate that the structure and the mixed valence character of the Cu_A site are preserved in all these variants. Interestingly, a comparison of the UV-vis spectra obtained experimentally and calculated by TD-DFT indicate that the different modifications alter the relative populations of the alternative σ_u^* and π_u ground states, i.e. modulate the size of $\Delta E_{\sigma_u^*/\pi_u}$ and, therefore, the thermal accessibility of the more energetic π_u ground state. In agreement with this interpretation, UV-vis spectra recorded as a function of temperature display changes of relative intensities that are consistent with varying Boltzmann populations. Some of the ^1H and ^{13}C NMR chemical shifts of the oxidized Cu_A centers exhibit an anti-Curie temperature dependence that reflects the Boltzmann-like relative populations of the alternative σ_u^* and π_u ground states. Quantitative treatment of these temperature dependencies in terms of a two-states model yields a measure of $\Delta E_{\sigma_u^*/\pi_u}$. As summarized in Figure 7, first and second sphere perturbations result in strong modulation of $\Delta E_{\sigma_u^*/\pi_u}$ and, moreover, the two effects display some degree of additivity. The $\Delta E_{\sigma_u^*/\pi_u}$ measured for the WT *Tt*-Cu_A site is 600 cm^{-1}, which implies 95:5 relative populations of the σ_u^* and π_u states at room temperature. This gap could be increased up to ca. 900 cm^{-1} to obtain π_u populations of 1% only, and decreased to virtually zero to obtain degenerate σ_u^* and π_u ground states.

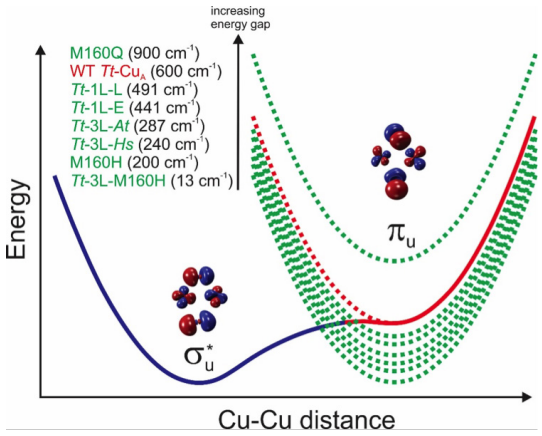

Figure 7. Schematic representation of the two-well potential energy surface of the Cu_A site as a function of the Cu-Cu coordinate. The different modifications summarized in Table 1 tune the energy gap ($\Delta E_{\sigma_u^*/\pi_u}$) between the two wells.

2.2. Redox thermodynamics of Cu_A

Reduction potentials have been experimentally determined for a variety of model Cu_A centers that include: (i) detergent solubilized integral CcO and N_2O-reductase wild type enzymes, (ii) Cu_A-containing soluble fragments of CcO subunit II and (iii) artificial Cu_A sites engineered into the scaffold of small soluble cupredoxins. The average E^0 taken over all values reported so far is 256 ± 80 mV. Given that the ligand set is preserved in all cases, the ±80 mV variability probably reflects differences in the protein milieu, although experimental variability may also play a role.

Interestingly, in the case of the chimeric protein *Pa*-Azu-Cu_A, $E°$ was found to upshift by 180 mV upon lowering pH from 7 to 4. EPR spectra exhibit concomitant drastic changes that suggest either a transition from mixed valence to localized valence or a slight change of wavefunction composition of the mixed valence complex induced by protonation at pH 4.[55,56] These results lead to a novel feedback inhibition mechanism for the activity of CcO. The ET-driven proton pumping activity of CcO is postulated to result in protonation and detachment of this His ligand, thus inducing a drastic upshift of E^0 that impairs ET and, thus, arrests CcO activity until protons are released into the outer membrane space and the His residue is deprotonated. This ground-breaking proposal, however, collides with a later finding that underlines the, until then overlooked, importance of the protein matrix: in the native *Tt*-Cu_A, a similar change of pH results in a modest 15 mV variation of E^0.[57] Moreover, eight different variants of *Tt*-Cu_A, generated either by single point mutation or by loop engineering, display upshifts of only 8-58 mV upon lowering pH from 7 to 3.5.[54] Most likely, the sharp contrast between the two model systems arises from the presence of a protonable residue, His35, in the artificial *Pa*-Azu-Cu_A construct that is not present in the native *Tt*-Cu_A protein.

In addition to the overall protein fold effect, first coordination sphere ligands exert a strong influence on E^0. For example, the thiolate ligands that constitute the Cu_2S_2 diamond strongly stabilize the oxidized form of Cu_A. When compared to T1 mononuclear copper centers this strong stabilization is expected to result in E^0 values lower than the average 256 mV, suggesting that valence delocalization partially compensates this effect relative to a trapped mixed-valence dimer. Also, the strong His equatorial ligands drastically affect E^0 and the electronic description of the center in general, as shown for the His260Asn mutant of the integral CcO from *Rhodobacter sphaeroides*. Mutation of the weak axial ligands, in contrast, is expected to be less disruptive in terms of the electronic structure, which also anticipates weaker modulation of E^0. This has been experimentally verified for the *Pa*-Azu-Cu_A model. On one hand, the esterification of the backbone carbonyl in Glu114 (weak axial ligand) has no effect on E^0.[58] Mutation of the other weak axial ligand Met, on the other hand, results in minor variations of E^0 of about 5 to 16 mV only.[59] However, in sharp contrast with this, equivalent mutations introduced in integral CcOs from *Rhodobacter sphaeroides* and from *Paracoccus denitrificans* shift E^0 by ca. 100-120 mV,[60,61] once again highlighting the importance of the overall protein scaffold in scaling the influence of first sphere ligands. The systematic mutation of the equivalent Met ligand in the soluble *Tt*-Cu_A fragment confirms this view, as it results in strong modulation of E^0 (Table 1) without affecting mixed valence delocalization.[49] Temperature-dependent electrochemical determinations for the different *Tt*-Cu_A variants reveal partial compensation of the enthalpic and entropic contributions that attenuate E^0 variations to some extent. Yet, E^0 values show a good linear correlation with the hydrophobicity of the weak axial ligand that can be associated to coulombic stabilization/destabilization of $Cu^{1.5+}$-$Cu^{1.5+}$ versus Cu^{+}-Cu^{+}.[52,54]

Investigations using the *Pa*-Azu-Cu_A model indicate that E^0 may also be tuned trough second sphere mutation, i.e. by exchanging residues in the vicinity of the site that do not directly interact with the metal ions. Subsequent work based on loop engineering of *Tt*-Cu_A confirmed this observation and provided deeper insight into the determinants of E^0 regulation by outer sphere and coordinating amino acids. In these studies, the outer sphere was modified by replacing either one or the three loops that define the nearby environment of the metal site, but preserving in all cases the set of ligand residues (*Tt*-3L-*Hs*, *Tt*-3L-*At*, *Tt*-1L-E and *Tt*-1L-L chimeras in Table 1).[50,54] These conservative loop permutations impact E^0 in about ±35 mV (Table 1) that, as expected, is an effect significantly smaller than the one achieved with first sphere modifications. The magnitude of this modulation correlates with the hydrophobicity of the metal environment, which is estimated as the sum of hydrophobicity indexes for all residues belonging to the three surrounding loops. Also, in this case the enthalpy and entropy contributions to E^0 partially compensate each other, thereby attenuating the variation of E^0.

Interestingly, the introduction of the Met160His mutation into the *Tt*-3L-*Hs* chimera to produce the *Tt*-3L-M160H variant results in a downshift of E^0 with respect to WT *Tt*-Cu_A, which approximately corresponds to the sum of the downshifts induced by the individual first and second sphere modifications.[53]

As discussed in the preceding section, inner and outer sphere mutations of the *Tt*-Cu_A site result in modulation of $\Delta E_{\sigma_u^*/\pi_u}$, which is expected to have an impact on E^0 other than just coulombic stabilization/destabilization. Indeed, it was found that the reduction entropies of the different *Tt*-Cu_A variants, including first and second sphere modifications,

increase with $\Delta E_{\sigma_u^*/\pi_u}$. To rationalize this dependency, it should be considered that the oxidized Cu_A can be described in terms of two energy wells, the σ_u* and π_u states, both spin doublets. Thereby, the statistical weight of $Cu^{1.5+}$-$Cu^{1.5+}$ is determined by the $\Delta E_{\sigma_u^*/\pi_u}/k_BT$ ratio, with limiting values of 2 and 4 for very large and very small $\Delta E_{\sigma_u^*/\pi_u}$, respectively. The reduced form, on the other hand, is a spin singlet and is represented by a single well potential energy surface of orbital symmetry σ_u*. These simple considerations lead to the following expression for reduction entropy as a function of $\Delta E_{\sigma_u^*/\pi_u}$:

$$\Delta S = -k_B ln\left(2 + 2e^{-}\,\Delta E_{\sigma_u^*/\pi_u}/k_B T\right) + k_B ln(Q^*_{Red}/Q^*_{Ox}) \qquad \text{(Eq. 6)}$$

The first term in equation 6 accounts for changes in the electronic part of the partition function, while the second term corresponds to the non-electronic components. The modulation of the reduction entropy trough the thermal accessibility of the alternative electronic ground state π_u has been found to have an impact of up to 100 mV on the E^0 values of Cu_A variants.[52]

2.3. Electron transfer kinetic parameters of Cu_A

According to the theory (see Introduction), the ET rate constant is determined by electronic coupling and and reorganization energy, in addition to the thermodynamic driving force or redox potential. The coupling, in turn, is determined by the structural and dynamical features of the medium connecting donor and acceptor redox centers. The electronic pathways implicated in the inter- and intra-protein ET reactions of the redox hub Cu_A from CcO have been extensively investigated; yet a consensus description remains elusive.

In the case of bovine CcO, calculations of effective couplings combined with all-atom molecular dynamics of the membrane-embedded enzyme indicated that the most efficient pathway for intramolecular Cu_A→ heme *a* ET starts at the equatorial ligand His204, continues across one H-bond towards either Arg438 or Arg 439, and finally trough another H-bond to reach the heme *a* propionate (Figure 8).[62] An equivalent result was obtained for Cu_A→ heme *b* ET in the ba_3-CcO from *Thermus thermophilus*.[48]

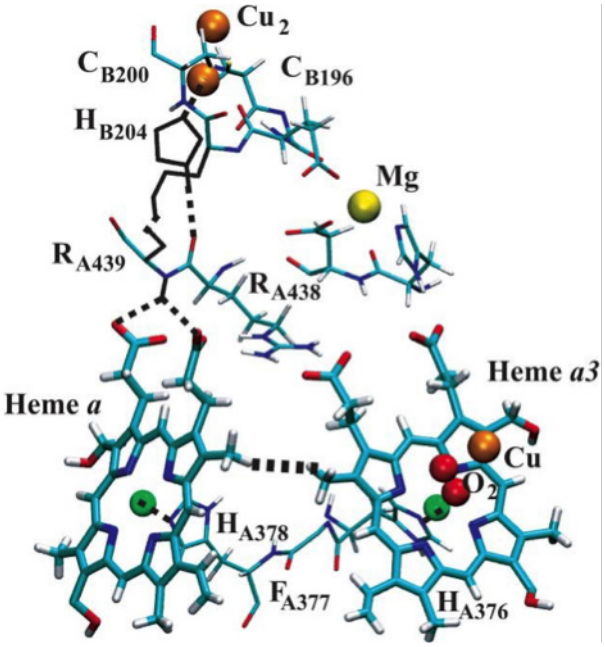

Figure 8. Intramolecular electron transfer pathways of CcO. Adopted from reference[62] with permission. Copyright 2003, Biophysical Society.

For the intermolecular Cyt-c→Cu_A ET reaction, calculations based on model and high resolution structures of the Cyt-c/CcO complex show that the most efficient pathway starts at either Trp104 or Tyr105 as electron entry gate, followed by a trough space jump to the weak axial ligand Met of the Cu_A center.[63] An equivalent route was predicted for the Cyt-c_{552}/*Tt*-Cu_A complex structure based on structures obtained by NMR and docking calculations.[64] Interestingly, quantum mechanical calculations show that the covalency of the Cu-S(Met), although low, is 10 times stronger in the π_u alternative GS relative to σ_u^*, which implies a ca. 100 times faster intermolecular ET reaction in the π_u state.[48] For the subsequent intramolecular ET step, the His pathway is favoured in the σ_u^* GS, as the covalency of the Cu- His bond is doubled compared to the π_u state. Taken together, these results suggest that the alternative π_u and σ_u^* ground states of Cu_A might be involved in effectively coupling upstream and downstream ET and in redirecting electrons by ca. 90°, as required by the geometry of the Cyt-c/CcO complex.[48]

ET reorganization energy has been experimentally determined for a few Cu_A proteins, including *Pa*-Azu-Cu_A, bovine CcO and *Tt*-Cu_A, yielding in all cases values around 0.3-0.4 eV.[1] Interestingly, these values are about a half of those determined for the related mononuclear T1 copper sites. This striking difference has been ascribed to the high electronic delocalization in Cu_A, which distributes redox-linked structural changes among twice the number of chemical bonds compared to mononuclear centers, thus reducing both the inner and outer sphere reorganization energies.

Quantum mechanical calculations performed assuming σ_u^* as the redox active molecular orbital afford λ values around 0.2-0.3 eV. Notably, this value doubles if the reaction proceeds from the alternative π_u GS, probably due to partial localization of the Cu_2S_2 covalence.[47,48]

Electrochemical experiments performed for a set of eight different *Tt*-Cu_A variants, including first and second sphere modifications (Figure 9), show clustering of the results in two groups, with average λ values of 0.53 ± 0.05 eV and 0.27 ± 0.05 eV, respectively.[54] The parameter that appears to determine membership of a particular protein variant to one or the other cluster is the energy gap $\Delta E_{\sigma_u^*/\pi_u}$, with small values around 12-256 cm^{-1} for the first group and significantly larger values around 440-900 cm^{-1} for the second one (Figure 9). Note that the first group includes variants that at room temperature present high populations of the alternative π_u GS, from ca. 25% up to full degeneracy (50 %). Moreover, the average λ obtained for this group closely resembles the QM prediction for the π_u GS. In the second group, in contrast, the average λ is very similar to the QM prediction for the σ_u^* GS, and protein variants included in this cluster have σ_u^* populations above 90 %. This clustering strongly suggest that the electrochemical experiments selectively probe one or the other redox active molecular orbital depending on the size of $\Delta E_{\sigma_u^*/\pi_u}$. Confirming this hypothesis, the M160H mutant falls into one or the other cluster depending on pH, which in turn has been found by UV-vis, EPR, RR and NMR to modulate $\Delta E_{\sigma_u^*/\pi_u}$ while preserving valence delocalization. Thus, experiments and calculations indicate that, for Cu_A variants with $\Delta E_{\sigma_u^*/\pi_u} > \Delta G_{ET}^{\#}$, the ET reaction proceeds from the lower-lying σ_u^* RAMO, while for centers with $\Delta E_{\sigma_u^*/\pi_u} < \Delta G_{ET}^{\#}$, the alternative π_u RAMO is preferentially involved. An important underlying implication of these results is that reaction coordinates for the ET reaction and for the $\sigma_u^* \rightarrow \pi_u$ conversion are strongly coupled. In line with this interpretation, the Cu-Cu distance is the main coordinate for the adiabatic $\sigma_u^* \rightarrow \pi_u$ transition, as demonstrated by QM calculations, and changes slightly with the redox state as determined by EXAFS.[54]

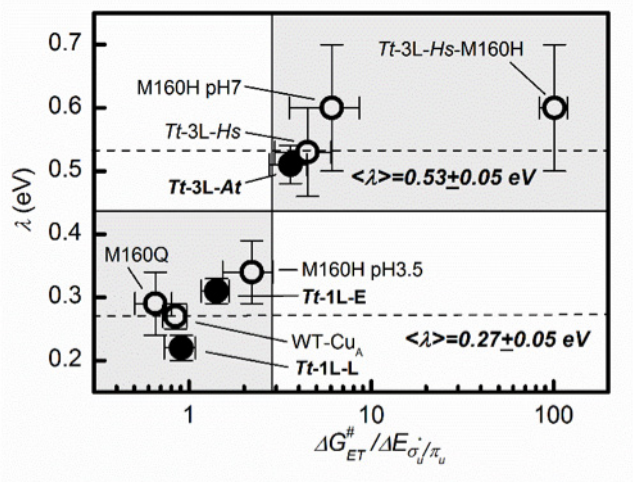

Figure 9. Electron transfer reorganization energy as a function of the ratio of ET activation energy divided by the energy gap between alternative ground states. Adopted with permission from reference [54]. Copyright 2019, American Chemical Society.

3. Regulation of Cyt-c→Cu_A intermolecular electron transfer

In the previous sections, I described some recent findings on the redox properties of Cyt-c and Cu_A metalloproteins. Here, I put these pieces of information together to hypothesize about a possible regulation mechanism of the Cyt-c→CcO ET reaction during electron-proton energy transduction in mitochondria (Figure 10).

When not associated, Cyt-c is in a native conformation of high λ value, which minimizes unwanted side redox reactions. Electrostatic binding to CcO leads to an initial complex that is not necessarily optimized in terms of heme c→Cu_A electron pathway and, therefore, reorientation of Cyt-c in the complex is required to enhance the electronic coupling. The electrostatic contacts in the complex induce subtle conformational distortions of Cyt-c (including disruption of the Met80/Tyr67 H-bond) that drive Cyt-c into a low λ native conformation that enables fast ET.

On the other hand, the idle form of the primary electron acceptor of CcO is largely dominated by the σ_u^* GS. Upon complex formation, subtle distortions of the Cu_A site induced by interaction with Cyt-c lower $\Delta E_{\sigma_u^*/\pi_u}$, favouring the π_u GS. This alternative GS accelerates heme c→Cu_A ET by two orders of magnitude compared to σ_u^* due to a more efficient mediation of the electronic coupling. The subsequent step is intramolecular ET from the reduced Cu_A site to heme a (or heme b, depending on the organism) in CcO. Electrons are redirected at ca. 90° abandoning the Cu_A site trough the His157 equatorial ligand. This pathway is favored by the σ_u^* GS due to a combination of enhanced V and lower λ. Thus, the alternation of electronic GS in Cu_A enable the switching of electron pathways that is required to ensure directionality despite the very low thermodynamic driving forces of the individual ET steps.

A temporary misbalance of proton translocation activity of respiratory complexes and consumption of the resulting electrochemical gradient by ATP-synthase may result in a deleterious hyperpolarization of the membrane. This, however, results in a rise of the local electric fields that may slow down the reorientation dynamics of Cyt-c in the complexes, thus undermining its ability to establish efficient electron pathways. Moreover, higher electric fields increase $\Delta E_{\sigma_u^*/\pi_u}$ in Cu_A, impairing the population of the most favorable electron entry gate, i.e. the π_u GS. Hence, the rise of the local electric field is expected to temporarily block or significantly slow down the proton-coupled ET reactions of the Cyt-c/CcO complex, until the electrochemical gradient is suffciently dissipated by ATP-synthase.

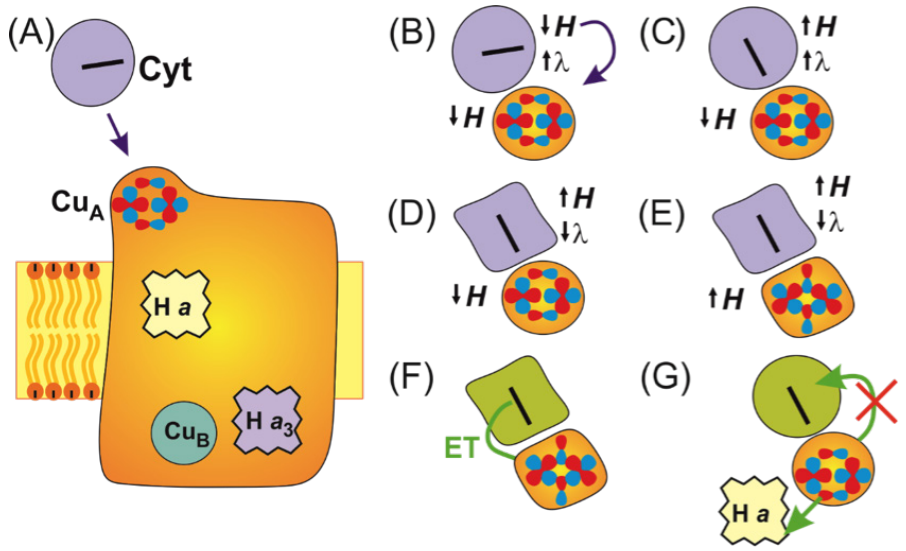

Figure 10. Schematic representation of the regulatory model for the Cyt-c/CcO ET reaction. Adopted from reference [32] with permission. Copyright 2014, Elsevier B.V. Cyt-c shuttles an electron towards the CcO, and docks near the Cu_A site (A). The complex is not optimized for ET so Cyt-c must reorient (B) in order to achieve a higher electronic coupling (C). In the process, more Cyt-c/CcO contacts are established, triggering a conformational transition of Cyt-c towards a lower λ form (D). The Cu_A site is perturbed in such a way that the π_u GS may be favored, thus further optimizing the electronic coupling (E). The ET reaction is then kinetically favored in spite of the low driving force and proceeds (F). Directionality is preserved and back ET is hampered because after the ET reaction the features that optimize the reaction are lost, and so the intramolecular ET towards heme a proceeds (G). Steps (B), (D) and (E) may be negatively affected by the strength of the interfacial electric field that increases because of the proton pumping resulting from the ET reactions. Thus, a regulatory negative feedback may be established due to the interplay between electron and proton transfer reactions. When the electric field lowers due to the activity of the ATP synthase, ET activity may be resumed.

Conclusions

Structural features such as first and second coordination spheres, local electrostatics and water accessibility are crucial determinants for the electronic properties of iron and copper metal sites in proteins, including thermodynamic and kinetic electron transfer parameters. The highly dynamical nature of proteins, in turn, enables the exploration of different structural and electronic configurations driven by thermal fluctuations. Moreover, specific electrostatic interactions, local electric fields and post-translational modifications reshape the free energy surfaces in a manner that may be central for the dynamic regulation of the canonical and alternative functions of metalloproteins. Understanding these complex mechanisms for the modulation of electron-proton energy transduction is essential from a basic biological and physicochemical perspective, but it is also a need for the successful development of metalloprotein-based technological devices such as biosensors, biofuel cells, enzymatic reactors and others.

Acknowledgment

Financial support by ANPCyT, UBACYT and CONICET is gratefully acknowledged.

References

[1] Liu, J.; Chakraborty, S.; Hosseinzadeh, P.; Yu, Y.; Tian, S.; Petrik, I.; Bhagi, A.; Lu, Y. Metalloproteins Containing Cytochrome, Iron-Sulfur, or Copper Redox Centers. *Chem. Rev.* **2014**, *114* (8), 4366–4369. https://doi.org/10.1021/cr400479b.

[2] Marcus, R. A.; Sutin, N. Electron Transfers in Chemistry and Biology. *BBA Rev. Bioenerg.* **1985**, *811* (3), 265–322. https://doi.org/10.1016/0304-4173(85)90014-X.

[3] Zitare, U. A.; Szuster, J.; Scocozza, M. F.; Espinoza-Cara, A.; Leguto, A. J.; Morgada, M. N.; Vila, A. J.; Murgida, D. H. The Role of Molecular Crowding in Long-Range Metalloprotein Electron Transfer: Dissection into Site- and Scaffold-Specific Contributions. *Electrochimica Acta* **2019**, *294*, 117–125. https://doi.org/10.1016/j.electacta.2018.10.069.

[4] Zitare, U. A.; Szuster, J.; Santalla, M. C.; Llases, M. E.; Morgada, M. N.; Vila, A. J.; Murgida, D. H. Fine Tuning of Functional Features of the CuA Site by Loop-Directed Mutagenesis. *Inorg. Chem.* **2019**. https://doi.org/10.1021/acs.inorgchem.8b03244.

[5] Beratan, D. N.; Onuchic, J. N.; Winkler; Gray, H. B. Electron-Tunneling Pathways in Proteins. *Science* **1992**, *258* (5089), 1740–1741. https://doi.org/10.1126/science.1334572.

[6] Alvarez-Paggi, D.; Hannibal, L.; Castro, M. A.; Oviedo-Rouco, S.; Demicheli, V.; Tórtora, V.; Tomasina, F.; Radi, R.; Murgida, D. H. Multifunctional Cytochrome c: Learning New Tricks from an Old Dog. *Chem. Rev.* **2017**, *117* (21), 13382–13460. https://doi.org/10.1021/acs.chemrev.7b00257.

[7] Bushnell, G. W.; Louie, G. V.; Brayer, G. D. High-Resolution Three-Dimensional Structure of Horse Heart Cytochrome c. *J. Mol. Biol.* **1990**, *214* (2), 585–595. https://doi.org/10.1016/0022-2836(90)90200-6.

[8] Hannibal, L.; Tomasina, F.; Capdevila, D. A.; Demicheli, V.; Tórtora, V.; Alvarez-Paggi, D.; Jemmerson, R.; Murgida, D. H.; Radi, R. Alternative Conformations of Cytochrome c: Structure, Function, and Detection. *Biochemistry* **2016**, *55* (3), 407–428. https://doi.org/10.1021/acs.biochem.5b01385.

[9] Capdevila, D. A.; Oviedo, R.; Tomasina, F.; Tortora, V.; Demicheli, V.; Radi, R.; Murgida, D. H. Active Site Structure and Peroxidase Activity of Oxidatively Modified Cytochrome c Species in Complexes with Cardiolipin. *Biochemistry* **2015**, *54* (51), 7491–7504. https://doi.org/10.1021/acs.biochem.5b00922.

[10] Capdevila, D. A.; Álvarez-Paggi, D.; Castro, M. A.; Tórtora, V.; Demicheli, V.; Estrín, D. A.; Radi, R.; Murgida, D. H. Coupling of Tyrosine Deprotonation and Axial Ligand Exchange in Nitrocytochrome c. *Chem. Commun.* **2014**, *50* (20), 2592–2594. https://doi.org/10.1039/C3CC47207H.

[11] Capdevila, D. A.; Marmisollé, W. A.; Tomasina, F.; Demicheli, V.; Portela, M.; Radi, R.; Murgida, D. H. Specific Methionine Oxidation of Cytochrome c in Complexes with Zwitterionic Lipids by Hydrogen Peroxide: Potential Implications for Apoptosis. *Chem. Sci.* **2015**, *6* (1), 705–713. https://doi.org/10.1039/c4sc02181a.

[12] Murgida, D. H.; Hildebrandt, P. Electron-Transfer Processes of Cytochrome c at Interfaces. New Insights by Surface-Enhanced Resonance Raman Spectroscopy. *Acc. Chem. Res.* **2004**, *37* (11), 854–861. https://doi.org/10.1021/ar0400443.

[13] Murgida, D. H.; Hildebrandt, P. Disentangling Interfacial Redox Processes of Proteins by SERR Spectroscopy. *Chem. Soc. Rev.* **2008**, *37* (5), 937–945. https://doi.org/10.1039/b705976k.

[14] Oviedo-Rouco, S.; Castro, M. A.; Alvarez-Paggi, D.; Spedalieri, C.; Tortora, V.; Tomasina, F.; Radi, R.; Murgida, D. H. The Alkaline Transition of Cytochrome c Revisited: Effects of Electrostatic Interactions and Tyrosine Nitration on the Reaction Dynamics. *Arch. Biochem. Biophys.* **2019**, *665*, 96–106. https://doi.org/10.1016/j.abb.2019.02.016.

[15] Yue, H.; Khoshtariya, D.; Waldeck, D. H.; Grochol, J.; Hildebrandt, P.; Murgida, D. H. On the Electron Transfer Mechanism Between Cytochrome c and Metal Electrodes. Evidence for Dynamic Control at Short Distances. *J. Phys. Chem. B* **2006**, *110* (40), 19906–19913. https://doi.org/10.1021/jp0620670.

[16] Murgida, D. H.; Hildebrandt, P. Electrostatic-Field Dependent Activation Energies Modulate Electron Transfer of Cytochrome c. *J. Phys. Chem. B* **2002**, *106* (49), 12814–12819. https://doi.org/10.1021/jp020762b.

[17] Alvarez-Paggi, D.; Castro, M. A.; Tórtora, V.; Castro, L.; Radi, R.; Murgida, D. H. Electrostatically Driven Second-Sphere Ligand Switch between High and Low Reorganization Energy Forms of Native Cytochrome c. *J. Am. Chem. Soc.* **2013**, *135* (11), 4389–4397. https://doi.org/10.1021/ja311786b.

[18] Paggi, D. A.; Martín, D. F.; Kranich, A.; Hildebrandt, P.; Martí, M. A.; Murgida, D. H. Computer Simulation and SERR Detection of Cytochrome c Dynamics at SAM-Coated Electrodes. *Electrochimica Acta* **2009**, *54* (22), 4963–4970. https://doi.org/10.1016/j.electacta.2009.02.050.

[19] Alvarez-Paggi, D.; Martín, D. F.; Debiase, P. M.; Hildebrandt, P.; Martí, M. A.; Murgida, D. H. Molecular Basis of Coupled Protein and Electron Transfer Dynamics of Cytochrome c in Biomimetic Complexes. *J. Am. Chem. Soc.* **2010**, *132* (16), 5769–5778. https://doi.org/10.1021/ja910707r.

[20] Murgida, D. H.; Hildebrandt, P. Heterogeneous Electron Transfer of Cytochrome c on Coated Silver Electrodes. Electric Field Effects on Structure and Redox Potential. *J. Phys. Chem. B* **2001**, *105* (8), 1578–1586.

[21] Khoa, L.; Wisitruangsakul, N.; Sezer, M.; Feng, J.-J.; Kranich, A.; Weidinger, I. M.; Zebger, I.; Murgida, D. H.; Hildebrandt, P. Electric-Field Effects on the Interfacial Electron Transfer and Protein Dynamics of Cytochrome c. *J. Electroanal. Chem.* **2011**, *660* (2), 367–376. https://doi.org/10.1016/j.jelechem.2010.12.020.

[22] Staffa, J. K.; Lorenz, L.; Stolarski, M.; Murgida, D. H.; Zebger, I.; Utesch, T.; Kozuch, J.; Hildebrandt, P. Determination of the Local Electric Field at Au/SAM Interfaces Using the Vibrational Stark Effect. *J. Phys. Chem. C* **2017**, *121* (40), 22274–22285. https://doi.org/10.1021/acs.jpcc.7b08434.

[23] Todorovic, S.; Murgida, D. H. Surface-Enhanced Raman Scattering of Biological Materials. In *Encyclopedia of Analytical Chemistry*; American Cancer Society, 2016; pp 1–29. https://doi.org/10.1002/9780470027318.a9574.

[24] Gu, J.; Yang, S.; Rajic, A. J.; Kurnikov, I. V.; Prytkova, T. R.; Pletneva, E. V. Control of Cytochrome c Redox Reactivity through Off-Pathway Modifications in the Protein Hydrogen-Bonding Network. *Chem. Commun.* **2014**, *50* (40), 5355–5357. https://doi.org/10.1039/C3CC47943A.

[25] Liptak, M. D.; Wen, X.; Bren, K. L. NMR and DFT Investigation of Heme Ruffling: Functional Implications for Cytochrome c. *J. Am. Chem. Soc.* **2010**, *132* (28), 9753–9763. https://doi.org/10.1021/ja102098p.

[26] Kranich, A.; Ly, H. K.; Hildebrandt, P.; Murgida, D. H. Direct Observation of the Gating Step in Protein Electron Transfer: Electric-Field-Controlled Protein Dynamics. *J. Am. Chem. Soc.* **2008**, *130* (30), 9844–9848. https://doi.org/10.1021/ja8016895.

[27] Wisitruangsakul, N.; Zebger, I.; Ly, K. H.; Murgida, D. H.; Ekgasit, S.; Hildebrandt, P. Redox-Linked Protein Dynamics of Cytochrome c Probed by Time-Resolved Surface Enhanced Infrared Absorption Spectroscopy. *Phys. Chem. Chem. Phys.* **2008**, *10* (34), 5276–5286. https://doi.org/10.1039/b806528d.

[28] Ly, H. K.; Marti, M. A.; Martin, D. F.; Alvarez-Paggi, D.; Meister, W.; Kranich, A.; Weidinger, I. M.; Hildebrandt, P.; Murgida, D. H. Thermal Fluctuations Determine the Electron-Transfer Rates of Cytochrome c in Electrostatic and Covalent Complexes. *ChemPhysChem* **2010**, *11* (6), 1225–1235. https://doi.org/10.1002/cphc.200900966.

[29] Capdevila, D. A.; Marmisollé, W. A.; Williams, F. J.; Murgida, D. H. Phosphate Mediated Adsorption and Electron Transfer of Cytochrome c. A Time-Resolved SERR Spectroelectrochemical Study. *Phys. Chem. Chem. Phys.* **2013**, *15* (15), 5386–5394. https://doi.org/10.1039/c2cp42044a.

[30] Alvarez-Paggi, D.; Meister, W.; Kuhlmann, U.; Weidinger, I.; Tenger, K.; Zimányi, L.; Rákhely, G.; Hildebrandt, P.; Murgida, D. H. Disentangling Electron Tunneling and Protein Dynamics of Cytochrome c through a Rationally Designed Surface Mutation. *J. Phys. Chem. B* **2013**, *117* (20), 6061–6068. https://doi.org/10.1021/jp400832m.

[31] Murgida, D. H.; Hildebrandt, P. Redox and Redox-Coupled Processes of Heme Proteins and Enzymes at Electrochemical Interfaces. *Phys. Chem. Chem. Phys.* **2005**, *7* (22), 3773–3784. https://doi.org/10.1039/b507989f.

[32] Alvarez-Paggi, D.; Zitare, U.; Murgida, D. H. The Role of Protein Dynamics and Thermal Fluctuations in Regulating Cytochrome c/Cytochrome c Oxidase Electron Transfer. *Biochim. Biophys. Acta - Bioenerg.* **2014**, *1837* (7), 1196–1207. https://doi.org/10.1016/j.bbabio.2014.01.019.

[33] Murgida, D. H.; Hildebrandt, P.; Wei, J.; He, Y.-F.; Liu, H.; Waldeck, D. H. Surface-Enhanced Resonance Raman Spectroscopic and Electrochemical Study of Cytochrome c Bound on Electrodes through Coordination with Pyridinyl-Terminated Self-Assembled Monolayers. *J. Phys. Chem. B* **2004**, *108* (7), 2261–2269.

[34] Oellerich, S.; Wackerbarth, H.; Hildebrandt, P. Spectroscopic Characterization of Nonnative Conformational States of Cytochrome c. *J. Phys. Chem. B* **2002**, *106* (25), 6566–6580. https://doi.org/10.1021/jp013841g.

[35] Kroll, T.; Hadt, R. G.; Wilson, S. A.; Lundberg, M.; Yan, J. J.; Weng, T.-C.; Sokaras, D.; Alonso-Mori, R.; Casa, D.; Upton, M. H.; et al. Resonant Inelastic X-Ray Scattering on Ferrous and Ferric Bis-Imidazole Porphyrin and Cytochrome c: Nature and Role of the Axial Methionine–Fe Bond. *J. Am. Chem. Soc.* **2014**, *136* (52), 18087–18099. https://doi.org/10.1021/ja5100367.

[36] Mara, M. W.; Hadt, R. G.; Reinhard, M. E.; Kroll, T.; Lim, H.; Hartsock, R. W.; Alonso-Mori, R.; Chollet, M.; Glownia, J. M.; Nelson, S.; et al. Metalloprotein Entatic Control of Ligand-Metal Bonds Quantified by Ultrafast x-Ray Spectroscopy. *Science* **2017**, *356* (6344), 1276–1280. https://doi.org/10.1126/science.aam6203.

[37] De, B.; Doctorovich, F.; Murgida, D. H.; Estrin, D. A. Electric Field Effects on the Reactivity of Heme Model Systems. *Chem. Phys. Lett.* **2007**, *434* (1–3), 121–126. https://doi.org/10.1016/j.cplett.2006.11.104.

[38] De, B.; Paggi, D. A.; Doctorovich, F.; Hildebrandt, P.; Estrin, D. A.; Murgida, D. H.; Marti, M. A. Molecular Basis for the Electric Field Modulation of Cytochrome c Structure and Function. *J. Am. Chem. Soc.* **2009**, *131* (44), 16248–16256. https://doi.org/10.1021/ja906726n.

[39] Assfalg, M.; Bertini, I.; Dolfi, A.; Turano, P.; Mauk, A. G.; Rosell, F. I.; Gray, H. B. Structural Model for an Alkaline Form of Ferricytochrome c. *J. Am. Chem. Soc.* **2003**, *125* (10), 2913–2922. https://doi.org/10.1021/ja027180s.

[40] Amacher, J. F.; Zhong, F.; Lisi, G. P.; Zhu, M. Q.; Alden, S. L.; Hoke, K. R.; Madden, D. R.; Pletneva, E. V. A Compact Structure of Cytochrome c Trapped in a Lysine-Ligated State: Loop Refolding and Functional Implications of a Conformational Switch. *J. Am. Chem. Soc.* **2015**, *137* (26), 8435–8449. https://doi.org/10.1021/jacs.5b01493.

[41] Abriata, L. A.; Cassina, A.; Tórtora, V.; Marín, M.; Souza, J. M.; Castro, L.; Vila, A. J.; Radi, R. Nitration of Solvent-Exposed Tyrosine 74 on Cytochrome c Triggers Heme Iron-Methionine 80 Bond Disruption. Nuclear Magnetic Resonance and Optical Spectroscopy Studies. *J. Biol. Chem.* **2009**, *284* (1), 17–26. https://doi.org/10.1074/jbc.M807203200.

[42] Wackerbarth, H.; Murgida, D. H.; Oellerich, S.; Döpner, S.; Rivas, L.; Hildebrandt, P. Dynamics and Mechanism of the Electron Transfer Process of Cytochrome c Probed by Resonance Raman and Surface Enhanced Resonance Raman Spectroscopy. *J. Mol. Struct.* **2001**, *563–564*, 51–59. https://doi.org/10.1016/S0022-2860(00)00808-5.

[43] Kagan, V. E.; Bayır, H. A.; Belikova, N. A.; Kapralov, O.; Tyurina, Y. Y.; Tyurin, V. A.; Jiang, J.; Stoyanovsky, D. A.; Wipf, P.; Kochanek, P. M.; et al. Cytochrome c/Cardiolipin Relations in Mitochondria: A Kiss of Death. *Free Radic. Biol. Med.* **2009**, *46* (11), 1439–1453. https://doi.org/10.1016/j.freeradbiomed.2009.03.004.

[44] Liu, B.; Chen, Y.; Doukov, T.; Soltis, S. M.; Stout, C. D.; Fee, J. A. Combined Microspectrophotometric and Crystallographic Examination of Chemically Reduced and X-Ray Radiation-Reduced Forms of Cytochrome Ba3 Oxidase from Thermus Thermophilus: Structure of the Reduced Form of the Enzyme. *Biochemistry* **2009**, *48* (5), 820–826. https://doi.org/10.1021/bi801759a.

[45] Williams, P. A.; Blackburn, N. J.; Sanders, D.; Bellamy, H.; Stura, E. A.; Fee, J. A.; McRee, D. E. The Cu_A Domain of *Thermus Thermophilus* Ba_3-Type Cytochrome *c* Oxidase at 1.6 Å Resolution. *Nat. Struct. Mol. Biol.* **1999**, *6* (6), 509–516. https://doi.org/10.1038/9274.

[46] Solomon, E. I.; Heppner, D. E.; Johnston, E. M.; Ginsbach, J. W.; Cirera, J.; Qayyum, M.; Kieber-Emmons, M. T.; Kjaergaard, C. H.; Hadt, R. G.; Tian, L. Copper Active Sites in Biology. *Chem. Rev.* **2014**, *114* (7), 3659–3853. https://doi.org/10.1021/cr400327t.

[47] Gorelsky, S. I.; Xie, X.; Chen, Y.; Fee, J. A.; Solomon, E. I. The Two-State Issue in the Mixed-Valence Binuclear CuA Center in Cytochrome c Oxidase and N2O Reductase. *J. Am. Chem. Soc.* **2006**, *128* (51), 16452–16453. https://doi.org/10.1021/ja067583i.

[48] Abriata, L. A.; Álvarez-Paggi, D.; Ledesma, G. N.; Blackburn, N. J.; Vila, A. J.; Murgida, D. H. Alternative Ground States Enable Pathway Switching in Biological Electron Transfer. *Proc. Natl. Acad. Sci. U. S. A.* **2012**, *109* (43), 17348–17353. https://doi.org/10.1073/pnas.1204251109.

[49] Ledesma, G. N.; Murgida, D. H.; Hoang, K. L.; Wackerbarth, H.; Ulstrup, J.; Costa-Filho, A. J.; Vila, A. J. The Met Axial Ligand Determines the Redox Potential in CuA Sites. *J. Am. Chem. Soc.* **2007**, *129* (39), 11884–11885. https://doi.org/10.1021/ja0731221.

[50] Morgada, M. N.; Abriata, L. A.; Zitare, U.; Alvarez-Paggi, D.; Murgida, D. H.; Vila, A. J. Control of the Electronic Ground State on an Electron-Transfer Copper Site by Second-Sphere Perturbations. *Angew. Chem. - Int. Ed.* **2014**, *53* (24), 6188–6192. https://doi.org/10.1002/anie.201402083.

[51] Zitare, U.; Alvarez-Paggi, D.; Morgada, M. N.; Abriata, L. A.; Vila, A. J.; Murgida, D. H. Reversible Switching of Redox-Active Molecular Orbitals and Electron Transfer Pathways in CuA Sites of Cytochrome c Oxidase. *Angew. Chem. - Int. Ed.* **2015**, *54* (33), 9555–9559. https://doi.org/10.1002/anie.201504188.

[52] Alvarez-Paggi, D.; Zitare, U. A.; Szuster, J.; Morgada, M. N.; Leguto, A. J.; Vila, A. J.; Murgida, D. H. Tuning of Enthalpic/Entropic Parameters of a Protein Redox Center through Manipulation of the Electronic Partition Function. *J. Am. Chem. Soc.* **2017**, *139* (29), 9803–9806. https://doi.org/10.1021/jacs.7b05199.

[53] Leguto, A. J.; Smith, M. A.; Morgada, M. N.; Zitare, U. A.; Murgida, D. H.; Lancaster, K. M.; Vila, A. J. Dramatic Electronic Perturbations of CuA Centers via Subtle Geometric Changes. *J. Am. Chem. Soc.* **2019**, *141* (3), 1373-1381. https://doi.org/10.1021/jacs.8b12335.

[54] Zitare, U. A.; Szuster, J.; Santalla, M. C.; Llases, M. E.; Morgada, M. N.; Vila, A. J.; Murgida, D. H. Fine Tuning of Functional Features of the CuA Site by Loop-Directed Mutagenesis. *Inorg. Chem.* **2019**, *58*, 2149–2157. https://doi.org/10.1021/acs.inorgchem.8b03244.

[55] Hwang, H. J.; Lu, Y. PH-Dependent Transition between Delocalized and Trapped Valence States of a CuA Center and Its Possible Role in Proton-Coupled Electron Transfer. *Proc. Natl. Acad. Sci.* **2004**, *101* (35), 12842–12847. https://doi.org/10.1073/pnas.0403473101.

[56] Xie, X.; Gorelsky, S. I.; Sarangi, R.; Garner, D. K.; Hwang, H. J.; Hodgson, K. O.; Hedman, B.; Lu, Y.; Solomon, E. I. Perturbations to the Geometric and Electronic Structure of the CuA Site: Factors That Influence Delocalization

and Their Contributions to Electron Transfer. *J. Am. Chem. Soc.* **2008**, *130* (15), 5194–5205. https://doi.org/10.1021/ja7102668.

[57] Alvarez-Paggi, D.; Abriata, L. A.; Murgida, D. H.; Vila, A. J. Native CuA Redox Sites Are Largely Resilient to PH Variations within a Physiological Range. *Chem. Commun.* **2013**, *49* (47), 5381–5383. https://doi.org/10.1039/c3cc40457a.

[58] Clark, K. M.; Tian, S.; Donk, W. A. van der; Lu, Y. Probing the Role of the Backbone Carbonyl Interaction with the CuA Center in Azurin by Replacing the Peptide Bond with an Ester Linkage. *Chem. Commun.* **2016**, *53* (1), 224–227. https://doi.org/10.1039/C6CC07274G.

[59] Hwang, H. J.; Berry, S. M.; Nilges, M. J.; Lu, Y. Axial Methionine Has Much Less Influence on Reduction Potentials in a CuA Center than in a Blue Copper Center. *J. Am. Chem. Soc.* **2005**, *127* (20), 7274–7275. https://doi.org/10.1021/ja0501114.

[60] Wang, K.; Geren, L.; Zhen, Y.; Ma, L.; Ferguson-Miller, S.; Durham, B.; Millett, F. Mutants of the CuA Site in Cytochrome c Oxidase of Rhodobacter Sphaeroides: II. Rapid Kinetic Analysis of Electron Transfer. *Biochemistry* **2002**, *41* (7), 2298–2304. https://doi.org/10.1021/bi0114630.

[61] Zickermann, V.; Verkhovsky, M.; Morgan, J.; Wikström, M.; Anemüller, S.; Bill, E.; Steffens, G. C. M.; Ludwig, B. Perturbation of the CuA Site in Cytochrome-c Oxidase of Paracoccus Denitrificans by Replacement of Met227 with Isoleucine. *Eur. J. Biochem.* **1995**, *234* (2), 686–693. https://doi.org/10.1111/j.1432-1033.1995.686_b.x.

[62] Tan, M.-L.; Balabin, I.; Onuchic, J. N. Dynamics of Electron Transfer Pathways in Cytochrome c Oxidase. *Biophys. J.* **2004**, *86* (3), 1813–1819. https://doi.org/10.1016/S0006-3495(04)74248-4.

[63] Shimada, S.; Shinzawa-Itoh, K.; Baba, J.; Aoe, S.; Shimada, A.; Yamashita, E.; Kang, J.; Tateno, M.; Yoshikawa, S.; Tsukihara, T. Complex Structure of Cytochrome c–Cytochrome c Oxidase Reveals a Novel Protein–Protein Interaction Mode. *EMBO J.* **2017**, *36* (3), 291–300. https://doi.org/10.15252/embj.201695021.

[64] Muresanu, L.; Pristovsek, P.; Löhr, F.; Maneg, O.; Mukrasch, M. D.; Rüterjans, H.; Ludwig, B.; Lücke, C. The Electron Transfer Complex between Cytochrome C552 and the CuA Domain of the Thermus Thermophilus ba3 Oxidase A Combined NMR and computational approach. *J. Biol. Chem.* **2006**, *281* (20), 14503–14513. https://doi.org/10.1074/jbc.M601108200.

Bio

Daniel H. Murgida

Daniel H. Murgida received his PhD in Chemistry in 1997 from the School of Sciences of the University of Buenos Aires. He has been Visiting Scientist at the University of Parma, Humboldt Fellow at the Max Planck Institute for Radiation Chemistry, Staff Scientist at the New University of Lisbon, and Assistant Professor at the Technical University of Berlin. Since 2007 he is a Professor and CONICET Researcher at the University of Buenos Aires. His research focuses on structure-dynamics-function relationships that determine redox and alternative functions of metalloproteins, and combines theoretical and experimental approaches, mainly protein electrochemistry, spectroscopy and vibrational spectroelectrochemistry.

Science Reviews
from the end of the world

Vol. 1, No.2, March 2020 // pp. 66-91 /

Morphology-dependent Photophysical Properties of Poly-4-vinylpyridine Polymers Containing –$Re(CO)_3(N^{\wedge}N)^+$ Pendants

Ezequiel Wolcan

Instituto de Investigaciones Fisicoquímicas Teóricas y Aplicadas (INIFTA, UNLP, CCT La Plata--CONICET), Argentina.
Email: ewolcan@inifta.unlp.edu.ar

Abstract

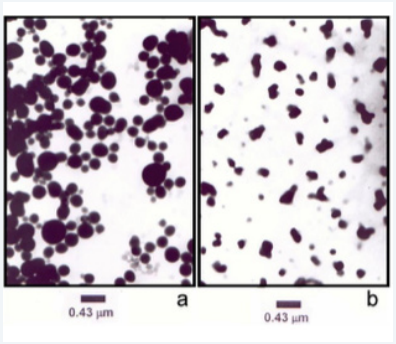

We review the morphological and the photophysical properties of several inorganic polymers that can be prepared from poly-4-vinylpyridine (P4VP). These polymers contain –$Re(CO)_3(N^{\wedge}N)^+$ pendants attached to their backbone with α-diimine ligands ($N^{\wedge}N$) such as 2,2´-bipyridine (bpy), 1,10-phenanthroline (phen), 3,4,7,8-tetramethyl-1,10-phenanthroline (tmphen) and 5-nitro-1,10-phenanthroline (NO_2-phen). These Re(I) polymers, show marked differences in their photophysical properties when compared to single $[pyRe(CO)_3(N^{\wedge}N)]^+$ molecules in diluted solutions. For example, Re→phen charge transfer excited states (MLCT) in the Re(I) polymers undergo a more efficient annihilation and/or secondary photolysis than in $[pyRe(CO)_3phen]^+$ complexes. Depending on solvent and/or cast film conditions, several aggregates of polymer strands with different morphologies were observed by transmission electron microscopy (TEM) and dynamic light scattering (DLS) techniques. Morphological changes derived from media-imposed changes (solvent, temperature) or from polymer backbone chemical modifications (protonation or peralkylation in P4VP uncoordinated pyridines) are responsible for the marked differences observed between the photophysical properties of these Re(I) polymers and those of the single $pyRe(CO)_3(N^{\wedge}N)^+$ molecules. Therefore, these Re(I) polymers can provide a good reaction scenario for other photochemical reactions. Thus, resonance energy transfer between –$Re(CO)_3(tmphen)^+$ and –$Re(CO)_3$ (NO_2-phen)$^+$ pendants was observed in Re(I)-P4VP polymers containing both chromophores attached to their backbone. In addition, in the quenching of the MLCT luminescence of –$Re(CO)_3(N^{\wedge}N)^+$ pendants by amines, we observed a retardation of the molecular motion due to the restricted media that favored the observation of the Marcus *inverted effect* in bimolecular reactions due to the fact that low values of the solvent reorganization energies are achieved within aggregates.

Keywords:
poly-4-vinylpyridine polymers, –Re(CO)3(N^N)+ pendants, Marcus inverted effect

Introduction

From the third row of transition metal compounds, Re(I) complexes have been of considerable research interest during the last four decades. In particular, $Re(I)(CO)_3$ complexes coordinating mono or bidentate azines of the type *fac*-

$LRe(CO)_3(N^N)$ (where L= halide and/or substituted azine and N^N = α-diimine, Scheme 1) show exceptionally rich excited-state behavior and redox chemistry as well as thermal and photochemical stability.[1] Through broad structural variations of the N^N ligand, they can be used in electron transfer studies,[2] solar energy conversion[3-5] and catalysis,[6] as luminescent sensors,[7-9] molecular materials for non-linear optics[10,11] and optical switching.[12] Additionally, the variation of L/N^N ligands allows incorporating these chromophores into several media such as proteins,[13-15] intercalating them into DNA,[16,17] or making them part of supramolecular structures.[18]

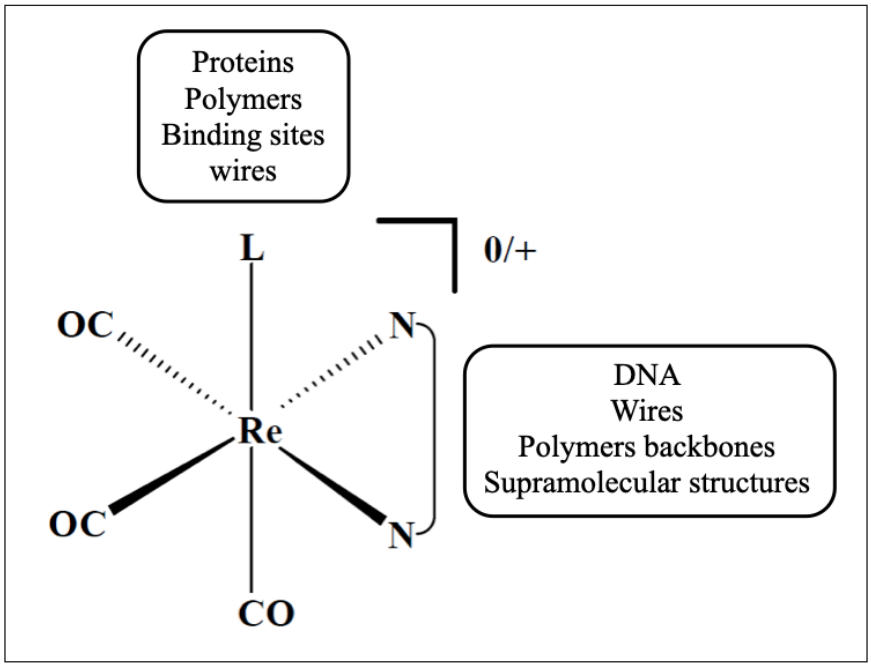

Scheme 1. Structural formulae of *fac*-$LRe(CO)_3(N^N)$ complexes. The complexes are neutral or positively charged for anionic or neutral axial ligands, L, respectively. Broad variations of L and/or equatorial (N^N) ligands allows to incorporate those complexes into several media, such as proteins, DNA, binding sites, wires, polymers and supramolecular structures.

Heterogeneous media such as micelles, organic polymers and microporous materials can provide a good reaction scenario for photochemical reactions. In addition, inorganic polymers present unique properties compared to those of their organic analogues. For instance, with the incorporation of inorganic elements within a polymeric backbone, a rich variety of different coordination numbers and geometries which are inaccessible with carbon-based organic backbones also become available. Moreover, the introduction of metallic elements offers the possibility of redox or catalytic activity and ready access to stable structures that possess unpaired electrons.

When transition metal compounds are attached to organic polymeric backbones, the metallic complexes can be confined within small spaces, and distances as low as 8Å may be encountered between two metallic centers, giving rise to new photochemical pathways that are not observed in diluted solutions of the simple molecules;[19] see Scheme 2. These small distances between metallic centers can be compared to the mean distances encountered in liquid solutions; eq. 1

$$R\ (\text{in } \mathring{A}) = \frac{6.5}{\sqrt[3]{C}} \qquad (1)$$

where C is the concentration in M units. Using a typical value for C in a photochemical experiment (i.e. $C \sim 1x10^{-4}$ M), a value of $R \sim 140$ Å is obtained. It is only at concentrations $C > 0.5$ M that mean distances between metal centers reach values of around 8 Å.

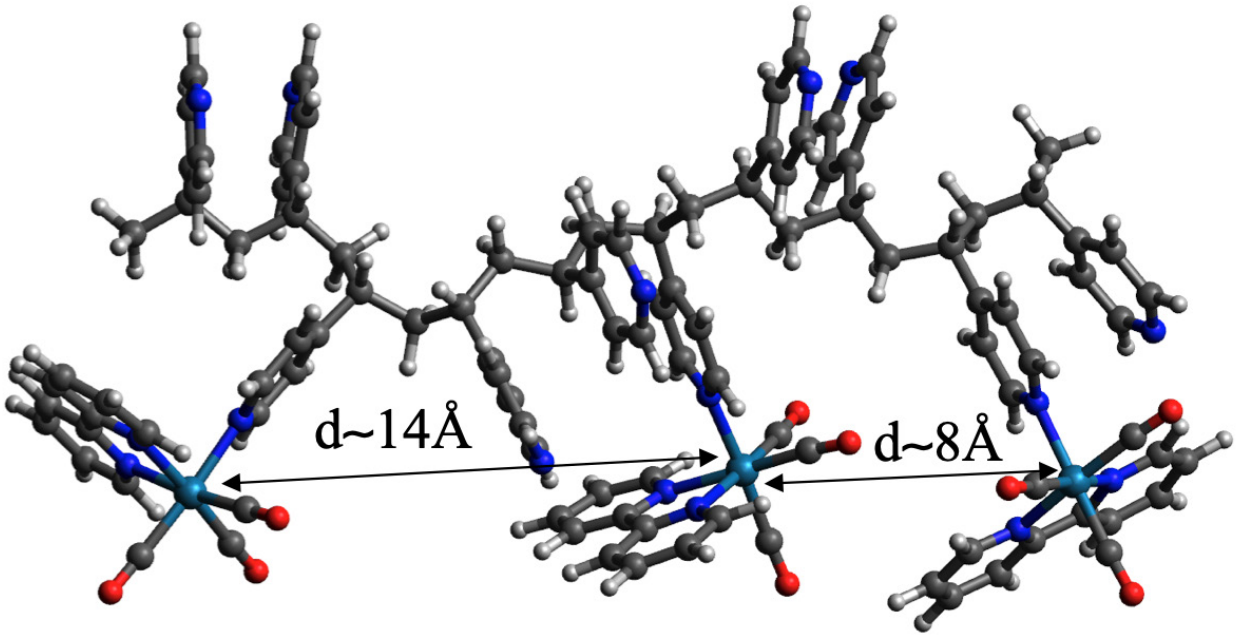

Scheme 2. Representation of a fragment (only three Re(I) chromophores are represented here) of polymer $[(vpy)_2$-vpyRe$(CO)_3(bpy)]_{n\sim200}(CF_3SO_3)_{n\sim200}$ showing mean inter-chromophore distances.

Polymers containing transition metal chromophores have been prepared where group phenomena such as fast, site-to-site energy transfer hopping and photochemically induced electron transfer have been observed.[20] Much of the literature examples involve transition metal ions metalating poly(p-phenylenevinylene) polymers incorporating 2,2-bipyridines,[21-23] polypyridil Ru(II) and/or Os(II) derivatized polystyrene[20,24-33] and some multimetallic oligomeric complexes containing Ru(II) and Os(II) coordinated to 1,10-phenanthroline (phen).[34] However, little attention was paid to Re(I) polymeric complexes, and only a few examples can be found in the literature up to the beginning of the new century.[35] After 2000, however, there has been a huge development in the field, mainly due to our research,[19,36-46] and the work of the research group led by Chan.[47,48]

1. Poly-4-vinylpyridine as a successful scaffold for new photochemical/morphology dependent phenomena

The polymers used in our works have been derived from the poly-4-vinylpyridine (P4VP) backbone and they contain $–Re(CO)_3(N^N)^+$ pendants in their structure. P4VP has a molecular weight of $M_w \sim 6{,}0x10^4$ and, on average, it contains about 600 vinylpyridine (vpy) units per formula. These inorganic polymers are synthesized by attaching pendant chromophores $–Re(CO)_3(N^N)^+$ to one third of the pyridines of the organic backbone (Scheme 3). The polymers can be assigned the formal structure of Scheme 3 where pendant $–Re(CO)_3(N^N)^+$ groups are randomly distributed along the strand of polymer with an average of two uncoordinated 4-vinylpyridine groups for each one coordinated to a Re(I) chromophore. The molecular weights of the final polymers range from 1.7 to $2.0x10^5$ depending on the nature of the ligand (N^N) used in polymer synthesis (Scheme 3).

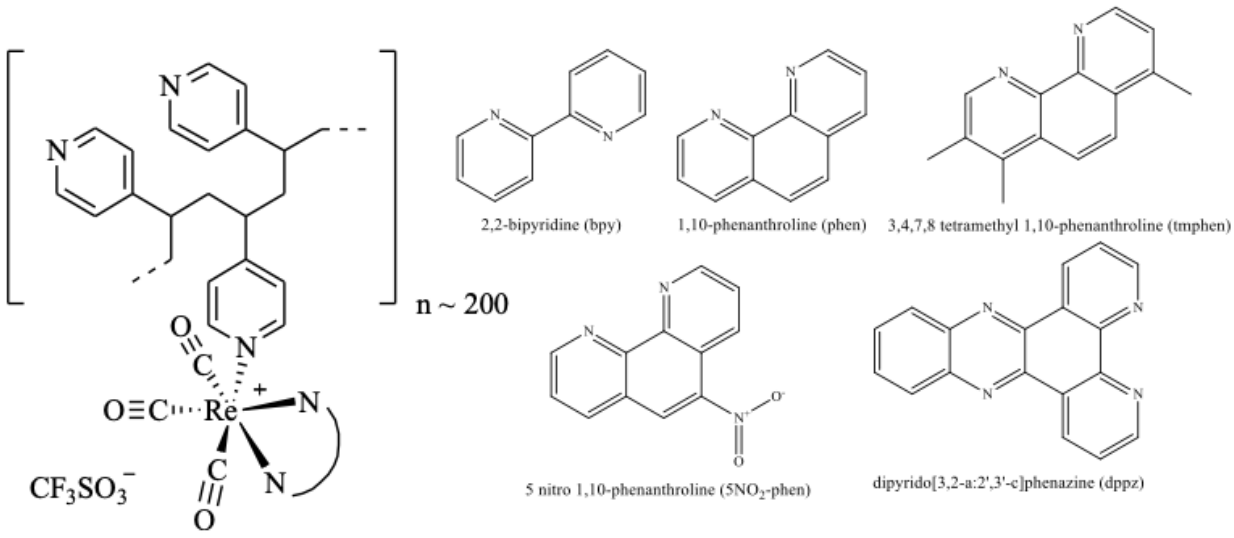

Scheme 3. Structural formulae of polymers derived from poly-4-(vinylpyridine) and $-Re(CO)_3(N^N)^+$ pendants with selected α-diimine ligands and the abbreviations used (in parenthesis).

The polymers were obtained in good yields (>80 %) by direct reaction of their respective $Re(CO)_3(N^N)CF_3SO_3$ complexes with P4VP in dichloromethane reflux under a N_2 blanket according to eq. 2

$$200\ Re(CO)_3(N^N)CF_3SO_3 + P4VP \rightarrow [(vpy)_2\text{-}vpyRe(CO)_3L]_{n\sim200}(CF_3SO_3)_{n\sim200} \quad (2)$$

Thus, the following polymers were obtained:

poly-I: $[(vpy)_2\text{-}vpyRe(CO)_3(phen)]_{n\sim200}(CF_3SO_3)_{n\sim200}$

poly-II: $[(vpy)_2\text{-}vpyRe(CO)_3(bpy)]_{n\sim200}(CF_3SO_3)_{n\sim200}$

poly-III: $[(vpy)_{m\sim338}\text{-}(vpy\text{-}Re(CO)_3(bpy))_{n\sim131}(vpy\text{-}Re(CO)_3(phen)_{p\sim131}](CF_3SO_3)_{n+p\sim262}$

poly-IV: $[(vpy)_{m\sim250}\text{-}(vpy\text{-}Re(CO)_3(bpy))_{n\sim200}(vpy\text{-}Re(CO)_3(phen)_{p\sim150}](CF_3SO_3)_{n+p\sim350}$

poly-V: $[(vpy)_2\text{-}vpyRe(CO)_3(tmphen)]_{n\sim200}(CF_3SO_3)_{n\sim200}$

poly-VI: $[(vpy)_2\text{-}vpyRe(CO)_3(NO_2\text{-}phen)]_{n\sim200}(CF_3SO_3)_{n\sim200}$

poly-VII: $[(vpy)_{m\sim400}\text{-}(vpy\text{-}Re(CO)_3(tmphen))_{n\sim180}(vpy\text{-}Re(CO)_3(NO_2\text{-}phen)_{p\sim20}](CF_3SO_3)_{n+p\sim200}$

poly-VIII: $[(vpy)_{m\sim400}\text{-}(vpy\text{-}Re(CO)_3(tmphen))_{n\sim150}(vpy\text{-}Re(CO)_3(NO_2\text{-}phen)_{p\sim50}](CF_3SO_3)_{n+p\sim200}$

poly-IX: $[(vpy)_{m\sim400}\text{-}(vpy\text{-}Re(CO)_3(tmphen))_{n\sim100}(vpy\text{-}Re(CO)_3(NO_2\text{-}phen)_{p\sim100}](CF_3SO_3)_{n+p\sim200}$

poly-X: $[(vpy\text{-}CH_3^+)_2\text{-}vpyRe(CO)_3(phen)]_{n\sim200}(CF_3SO_3)_{n\sim600}$

poly-XI: $[(vpy)_2\text{-}vpyRe(CO)_3(dppz)]_{n\sim200}(CF_3SO_3)_{n\sim20}$

where poly-X, i.e. $[(vpy\text{-}CH_3^+)_2\text{-}vpyRe(CO)_3(phen)]_{n\sim200}(CF_3SO_3)_{n\sim600}$ was obtained by peralkylation of the free pyridines of poly-I; eqs. 3-4

$$[(vpy)_2\text{-}vpyRe(CO)_3(phen)]_{n\sim200}(CF_3SO_3)_{n\sim200} \xrightarrow{ICH_3}$$

$$[(vpy\text{-}CH_3^+)_2\text{-}vpyRe(CO)_3(phen)]_{n\sim200}(CF_3SO_3)_{n\sim200}(I)_{m\sim400} \quad (3)$$

$$[(vpy\text{-}CH_3^+)_2\text{-}vpyRe(CO)_3(phen)]_{n\sim200}(CF_3SO_3)_{n\sim200}(I)_{m\sim400} \xrightarrow[-AgI]{AgCF_3SO_3}$$

$$[(vpy\text{-}CH_3^+)_2\text{-}vpyRe(CO)_3(phen)]_{n\sim200}(CF_3SO_3)_{n\sim600} \quad (4)$$

These polymers display interesting as well as intriguing features both in photochemistry and in material science, which we will discuss in the following sections. From a historic perspective, however, it should be noted that when we started our research with poly-I,[42] poly-II[40] and poly-X,[44] we were unaware of their morphology and the fact that morphological changes could affect the photochemical properties of these polymers. This initial *unawareness* was mainly because in previous studies that appeared in the literature, i.e. those Ru(II) and Os(II) polymers[20-34] previously mentioned in the introduction, there was a lack of morphological studies. It was not up until the work carried out by Chan's group,[47,48] and almost in parallel by our work,[39] that the morphological properties of those inorganic polymers were taken into account and studied in depth.

2. Contrasting the photophysical properties of poly-I and poly-X with those of $[pyRe(CO)_3phen]^+$ complex

The UV-vis spectra of poly-I and $pyRe(CO)_3phen^+$ exhibited similar features. The extinction coefficients of poly-I, however, by comparison to the extinction coefficients of the molecular complex, corresponded to ~200 chromophores, $–Re(CO)_3phen^+$, per formula weight of polymer. This was in good agreement with the load of Re(I) pendants expected from the calculation from the elemental analysis and with the structures shown in Scheme 3.

Identical band shapes from the emission spectra were observed in N_2-degassed CH_3CN solutions of $[pyRe(CO)_3phen]^+$ and poly-I centered at λ_{max} = 560 and 565 nm, respectively. Flash photolysis experiments irradiating with λ_{exc} = 351 nm to either poly-I or $[pyRe(CO)_3phen]^+$ complex in deaerated CH_3CN produced nearly identical transient absorption spectra, respectively, assigned to the ^{3}MLCT excited states. The ^{3}MLCT excited state spectra, λ_{max} ~ 460 nm and λ_{max} ~ 750 nm, remained the same and did not change with the number n_{hv} of 351 nm photons absorbed by either $[pyRe(CO)_3phen]^+$ or by the $-Re(CO)_3phen^+$ pendant chromophores of poly-II.[42] Conversely, the quantum yield of the MLCT excited state, Φ_{MLCT}, and its lifetime, showed marked dependences on n_{hv} and the photogenerated MLCT excited state concentration. For $[pyRe(CO)_3phen]^+$, despite the fact that Φ_{MLCT} was nearly independent of n_{hv} for n_{hv} values that were below 20% of the total Re(I) concentration, it decreased monotonically above that limit. Similar experiments carried out with solutions of poly-I in CH_3CN or $MeOH/H_2O$ mixed solvent showed that Φ_{MLCT} decreased with n_{hv} and reached the same value of that of $[pyRe(CO)_3phen]^+$ in the limit $n_{hv} \rightarrow 0$ (see Figure 1). In addition, the disappearance of the MLCT excited states in $[pyRe(CO)_3phen]^+$ and in the Re(I) polymer occurred with different reaction kinetics. The decay of the ^{3}MLCT excited states of the pendant chromophores of poly-I exhibited more marked second order behavior than the decay of the ^{3}MLCT excited states of $[pyRe(CO)_3phen]^+$. As shown in Figure 2, the linear dependence of $t_{1/2}$ on the reciprocal of the MLCT concentration demonstrated that the MLCT decay was kinetically of a second order on the MLCT concentration for n_{hv} values larger than 17% of the total Re(I) concentration. A similar study of the MLCT decay kinetics with $[pyRe(CO)_3phen]^+$ established that traces were well fitted to a single exponential and the lifetime exhibited no dependence on MLCT concentration until n_{hv} corresponded to 30% of the Re(I) concentration. These experimental observations showed that the process whose rate was kinetically of a second order in MLCT concentration contributed less to the excited state decay in $[pyRe(CO)_3phen]^+$.[42]

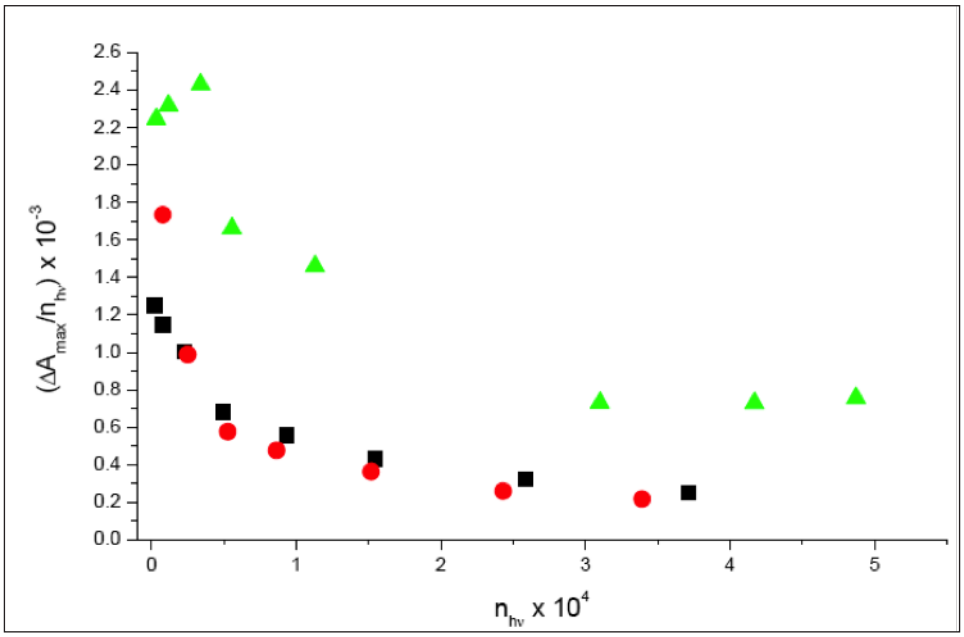

Figure 1. Dependence of the MLCT excited-state quantum yield, φ_{MLCT} (assumed proportional to $\Delta A_{max}/n_{hv}$), on n_{hv} in laser flash photolysis (351 nm) of $[pyRe(CO)_3phen]^+$ and Poly-I. Solutions of the Re(I) complexes in deaereated CH_3CN were used with $[pyRe(CO)_3phen]^+$ (▲) and Poly-I (■). Solutions in deaereated MeOH/H_2O (1:4) of the Re(I) polymer were used in (●) experiments. Reprinted with permission from ref. 42. Copyright 2005 American Chemical Society.

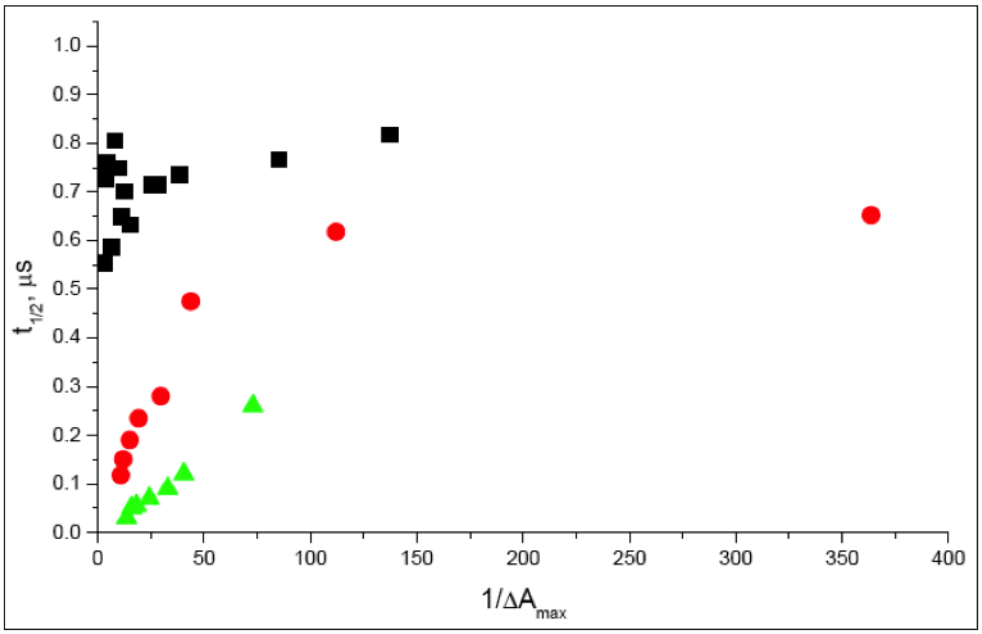

Figure 2. Dependence of MLCT state $t_{1/2}$ on $1/\Delta A_{max}$ for $[pyRe(CO)_3phen]^+$ in CH_3CN (■), for Poly-I in CH_3CN (●) and for Poly-I in MeOH-H_2O (▲).Reprinted with permission from ref. 42. Copyright 2005 American Chemical Society.

From a photochemistry standpoint, these Re(I) polymers, show marked differences in their photophysical properties when compared to single $[pyRe(CO)_3phen]^+$ molecules in diluted solutions. For example, Re→phen charge transfer excited states (MLCT) in the Re(I) polymers undergo a more efficient annihilation and/or secondary photolysis than in $[pyRe(CO)_3phen]^+$ complexes; eq. 5-6.[42]

$$[\text{–Re(CO)}_3\text{phen}]^+ \underset{h\nu_{em}}{\overset{h\nu}{\rightleftharpoons}} {}^3\text{MLCT} \xrightarrow{h\nu} [\text{–Re(CO)}_3\text{phen}]^{+*} \quad (5)$$

$$2\ ({}^3\text{MLCT}) \longrightarrow [\text{–Re(CO)}_3\text{phen}]^+ + [\text{–Re(CO)}_3\text{phen}]^{+*} \quad (6)$$

In these equations, $[\text{–Re(CO)}_3\text{Lphen}]^{+*}$ denotes an excited state higher in energy than the MLCT assigned as an intra-ligand, IL, excited state, generated in the $\text{–Re(CO)}_3\text{phen}^+$ pendant chromophore. In Equation 5, the annihilation of two ^{3}MLCT excited states forms chromophores in the ground state and intra-ligand, IL, excited states. In contrast to the ^{3}MLCT, the ^{3}IL excited states oxidize solvents like CH_3OH.[42]

Absorption of light by MLCT excited states in the polymer to form intraligand excited states, IL, accounts for the functional dependence of Φ_{MLCT} on n_{hv} explaining a decrease of Φ_{MLCT} with n_{hv} at lower n_{hv} values than the decrease of Φ_{MLCT} with n_{hv} observed with $[\text{pyRe(CO)}_3\text{phen}]^+$ molecules. Because the IL excited state is shorter-lived than the MLCT excited state, the decay represented in Equation 5 is faster than the instrument's 20 ns response, and it was manifested only by a smaller photogenerated concentration of MLCT in the polymer than the expected one. A fast intrastrand annihilation of MLCT excited states also provides a good rationale for the functional dependence of Φ_{MLCT} on n_{hv}. In this mechanism, the rapid curvature of Φ_{MLCT} with n_{hv} in Figure 1 requires that a large fraction of photogenerated excited states vanishes within the 20 ns laser pulse. Within the strand of polymer, if excited Re chromophores are close neighbors and have the right spatial orientation, they may undergo a fast annihilation within that period of time. This fast annihilation process can create IL excited states that are placed at higher energies and that are more reactive than the parent MLCT excited state.

The excited chromophores that have not experienced a fast annihilation or secondary photolysis due to being disfavored by reason of their position will be observed at times longer than the 20 ns laser irradiation. Flash photolysis shows that the rate of decay of this remnant excited state population is kinetically of a second order in the overall MLCT concentration. The second-order kinetics indicates that mechanisms by which the energy moves through the strand of polymer are available, since diffusive motions of the polyelectrolyte are much slower than those of the observed decay of excited states. Various mechanisms of intramolecular energy transfer have been proposed for organic polymers.[42] For instance, energy hopping in the strand may form pairs of excited chromophores that undergo annihilations. Experimental observations with poly-X, in which uncomplexed pendant pyridine groups of poly-I are methylated, support this mechanism, as quaternization of the pyridine groups to form poly-X enhanced electron transfer through the strand of the polymer.[44] The process could involve excited states of the uncomplexed pyridine pendants. It is also possible that energy can be transferred between remotely placed excited chromophores. These events will leave, therefore, one chromophore in the ground state and the other in an upper intraligand excited state, IL. This process is in contrast with the intrastrand energy transfers that occur during the irradiation of a P4VP polymer containing pendants $\text{–[Re(CO)}_3\text{(phen)]}^+$ chromophores.[42]

3. Laser power, thermal and solvent effects on the photophysical properties of poly-II

The emission spectra of $[\text{pyRe(CO)}_3\text{bpy}]^+$and that of poly-II showed a distinctive behavior in solvent mixtures. In deoxygenated DMSO-CH_3CN (1 : 9 v/v) mixtures at room temperature, the emission spectra of $[\text{pyRe(CO)}_3\text{bpy}]^+$ and poly-II exhibited unstructured bands with similar band shapes centered at 575 and 577 nm, respectively. For both poly-II and $[\text{pyRe(CO)}_3\text{bpy}]^+$, the emission maximum shifted to 569 nm in DMSO-CH_2Cl_2 (1 : 9 v/v). In DMSO-water (1 : 9 v/v) mixtures, however, the emission maximum for $[\text{pyRe(CO)}_3\text{bpy}]^+$ was observed at 574 nm, while in the case of poly-II, it shifted to λ_{max} = 561 nm.[40]

Emission decays in the mixed solvents DMSO-CH_3CN, DMSO-CH_2Cl_2 and DMSO–water were monoexponential for CF_3SO_3[pyRe(CO)$_3$bpy]. However, for poly-II, monoexponential emission decays were only observed with DMSO-CH_3CN mixtures, while in DMSO–water and DMSO–CH_2Cl_2 mixtures the emission decay became biexponential.[40] Table 1 summarizes steady state luminescence maxima and time resolved luminescence and transient absorbance lifetimes for CF_3SO_3[pyRe(CO)$_3$bpy] and $\{[(\text{vpy})_2\text{-vpyRe(CO)}_3\text{bpy}]\ CF_3SO_3\}_{n\sim200}$ in different experimental conditions.

Table 1. Emission maxima and luminescence (τ_{em}) and transient absorption (τ_{abs}) lifetimes for $[pyRe(CO)_3bpy]^+$ and poly-II in different experimental conditions at room temperature. Data taken from ref. 40

Compound	Solvent	λ_{em} / nm	τ_{em} / ns	τ_{abs} / ns	λ_{exc}/nm
$[pyRe(CO)_3bpy]^+$	CH_3CN	-	260	282	355
	MeOH	-	218	227	355[a]
	CH_3CN		-	225	351[b]
	CH_3CN	-	245	-	337[c]
	DMSO-CH_3CN	575	213	-	337
	DMSO-CH_2Cl_2	569	316	-	337
	DMSO-water	574	133	-	337
poly-II	CH_3CN	-	226, 53	187, <10	355
	MeOH	-	201, 67	185	355
	CH_3CN	-	-	184, 35	351
	CH_3CN	-	203	-	337
	DMSO-CH_3CN	577	137	-	337
	DMSO-CH_2Cl_2	569	143, 31	-	337
	DMSO-water	561	440, 83	-	337

[a]Nd-YAG laser [b]Excimer laser [c]Nitrogen laser

The effect of temperature on luminescence lifetimes also showed a distinctive behavior for $CF_3SO_3[pyRe(CO)_3bpy]$ and poly-II. A monoexponential decay of luminescence in CH_3CN solutions was observed for both $[pyRe(CO)_3bpy]^+$ and poly-II for the entire temperature range (0-65°C) in study. Moreover, the temperature dependence of emission lifetime is nearly the same for the two compounds.[40] In CH_3CN-water (1:4) solutions, however, results were very different for $[pyRe(CO)_3bpy]^+$ and poly-II. The emission decay of $[pyRe(CO)_3bpy]^+$ remains monoexponential between 0°C and 65°C, with nearly the same slope, i.e. $\partial\ln(1/\tau)/\partial T$, as in the case of CH_3CN solutions. However, the polymer showed a biexponential behavior at temperatures below 15°C, with a higher $\partial\ln(1/\tau)/\partial T$ showing a much more marked dependence of τ on temperatures between 15°C and 0°C than between 15°C and 65°C.[40]

When poly-II is irradiated with low photonic fluxes, i.e. in steady state or in laser flash irradiations with $n_{hv} \leq 2$ mJ/pulse, only small differences are discerned when the photophysical processes of the MLCT excited state of $-Re(CO)_3bpy^+$ pendants are compared to the photophysical processes of the MLCT excited state in the $CF_3SO_3[pyRe(CO)_3bpy]$ complex. In fact, emission decay lifetimes of both $CF_3SO_3[pyRe(CO)_3bpy]$ and poly-II in CH_3CN, calculated from 337 nm flash excitations experiments, are monoexponential and very similar. However, a longer lifetime for the $[pyRe(CO)_3bpy]^+$ (τ_{em} = 245 ns), compared to poly-II, (τ_{em} = 203 ns) could be associated to the availability of new deactivation pathways for the MLCT in the polymer due to vibration modes present in the P4VP backbone. This experimental observation and the similarity of $[pyRe(CO)_3bpy]^+$ and the polymer absorption and emission spectra suggest that electronic interactions between Re(I) chromophores in the polymer are negligible in solvents like CH_3CN or DMSO-CH_3CN mixtures. However, this would not be the case for solvents of very low or very high polarity, as in DMSO-CH_2Cl_2 and DMSO-water mixtures, respectively. Even though the shape and maxima of emission spectra in DMSO-CH_2Cl_2 are nearly the same for $[pyRe(CO)_3bpy]^+$ and the polymer, the polymer experiences a biexponential emission being τ_1 = 143 ns and τ_2 = 31 ns, respectively. Those lifetimes are considerably shorter than that for $[pyRe(CO)_3bpy]^+$, τ = 316 ns. Moreover, the polymer emission spectrum in DMSO-water is blue-shifted (~ 13 nm) compared to the one of $[pyRe(CO)_3bpy]^+$, and the emission

decay is also biexponential. These photophysical disparities suggest (*vide infra*) that conformational and morphology changes are affecting the photophysical properties of Poly-II, like in the solvent-dependent aggregation observed in a similar polymer, i.e. polystyrene-block-poly(4-vinylpyridine) (PS-b-PVP) functionalized with pendants -$Re(CO)_3(bpy)^+$ groups.[35]

Laser flash irradiations with $n_{hv} \geq 12$ mJ/pulse at $\lambda_{ex} = 351$ nm or 355 nm show a very different photophysical behavior for poly-II and $CF_3SO_3[pyRe(CO)_3bpy]$, respectively. Φ_{MLCT} is nearly three times higher for $[pyRe(CO)_3bpy]^+$ than for the polymer.[40] Besides, emission decay for $[pyRe(CO)_3bpy]^+$ is monoexponential with a lifetime that is nearly the same as that observed at irradiations with $n_{hv} \leq 2$ mJ/pulse at $\lambda_{ex} = 337$ nm. However, for poly-II, emission decay could only be fitted with two exponentials and the transient generated also experiences a biexponential decay. A fast intrastrand annihilation of MLCT excited states can provide a good explanation for the lower amount of MLCT excited states observed in flash photolysis experiments with the polymer compared to that of the $[pyRe(CO)_3bpy]^+$. As in the case of poly-I, this mechanism requires that a large fraction of the photogenerated excited states vanishes within the 20 ns laser pulse. If excited $–Re(CO)_3bpy^+$ chromophores are close neighbors and have the correct spatial orientation within the polymer strand, they may undergo a fast annihilation within that period of time. However, using high intensity pulses, a secondary photolysis of the MLCT in the polymer to form intraligand excited states, as discussed above for poly-I, cannot be discarded in this rationalization. Excited chromophores that are disfavored by reason of their position for a fast annihilation or because they do not undergo secondary photolysis will be observed decaying at times longer than 20 ns. The number of these excited chromophores will be higher in flash photolysis experiments with high laser powers (i.e. $\lambda_{ex} = 351$ nm or 355 nm) than in flash photolysis experiments with the low power N_2 laser ($\lambda_{ex} = 337$ nm), explaining why 351 nm excitation produces a transient that decays biexponentially and the transient produced after 337 nm excitation decays by first order kinetics. In poly-I, a second order process was observed in addition to the MLCT first order decay (*vide supra*). It should be noted (see Table I) that the longer luminescence lifetime observed after 355 nm or 351 nm excitation is nearly the same as that observed after 337 nm photolysis. The shorter lifetime in 351 nm experiments could be ascribed to the second order processes mentioned before.

4. Morphological properties of the polymers

Poly-II. The morphologies of poly-**(**II) were studied by transmission electron microscopy (TEM), dynamic light scattering (DLS) and static light scattering (SLS). In TEM studies, the polymer films were obtained by room temperature solvent evaporation of CH_3CN solutions of poly-II. When taking photos, the polymer films were not stained with any chemicals, and the contrast of the image in the TEM photos can only originate from the rhenium complexes incorporated to the polymers. The $–Re(CO)_3bpy^+$ chromophores in poly-II aggregate and form isolated nanodomains that are dispersed in the polymer matrix film. The dimensions of the nanodomains are between 90 and 430 nm, and they are mainly spherical in shape (Figure 3 a). It should be noted that the dimensions of these nanodomains are considerably larger than the full stretch length of the polymers. As a result, it is likely that the nanodomains contain a considerable number of polymer molecules. Assuming that the mean density of a given nanodomain is the same as that of an isolated poly-II random coil polymer and, neglecting solvation contributions to the hydrodynamic radii, a ratio of around 400 polymer strands constituting a single nanodomain was estimated.[39] When the free pyridines of poly-II are coordinated to $CuCl_2$, the poly-II/$CuCl_2$ polymers aggregate in nanodomains that are distorted from the spherical shape and whose dimensions are smaller than those nanodomains formed by the poly-II (see Figure 3 b). TEM images obtained for poly-II and poly-II/$CuCl_2$ polymers are comparable to the calculated hydrodynamic radii of 156 ± 6 nm and 96 ± 11 nm from DLS experiments for the aggregates of the poly-II and poly-II/$CuCl_2$ polymers, respectively.[39]

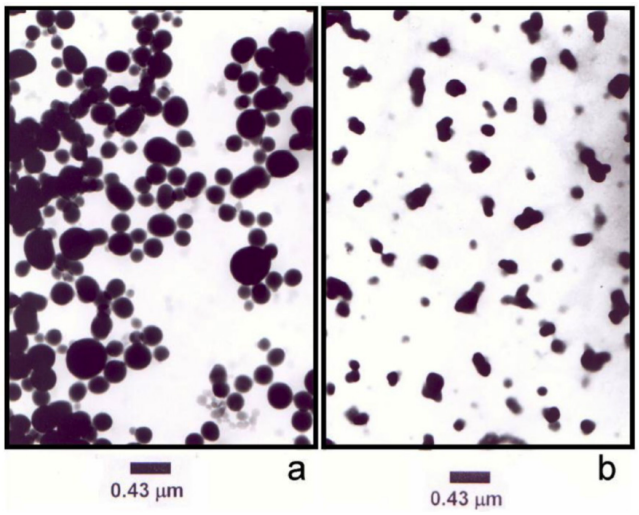

Figure 3. Distortion and shrinkage of spherical nanodomains in poly-II polymers after the binding of $CuCl_2$ to the free pyridines of the Re(I) polymer. The Figure shows transmission electron micrographs in solvent cast films of polymers (a) poly-II and (b) poly-II after saturation of the free pyridines with $CuCl_2$. Reprinted with permission from ref. 39. Copyright 2005 American Chemical Society.

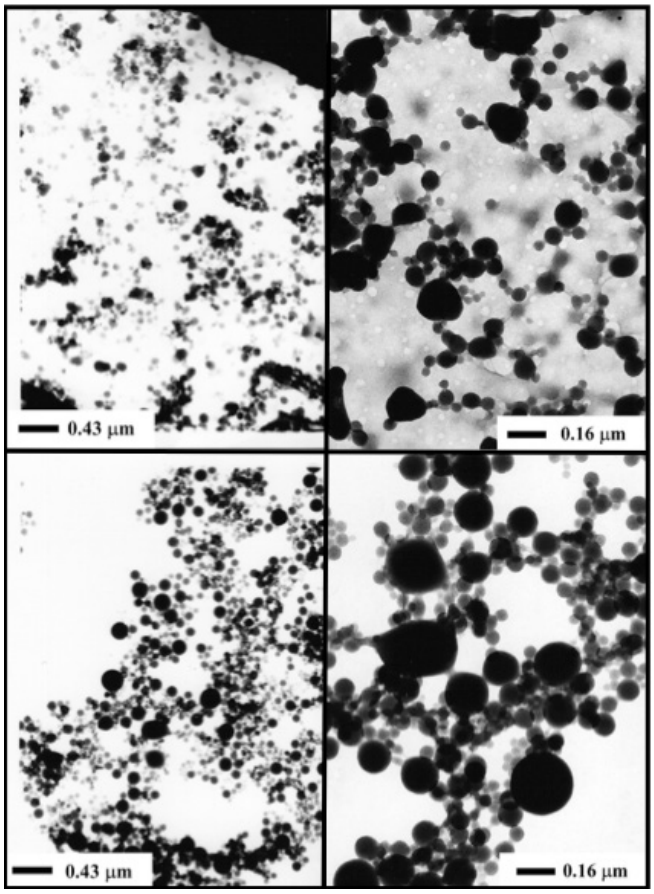

Figure 4. Transmission electron micrographs in ACN cast films of poly-(III) (top, right and left panels) and poly-(IV) (bottom, right and left panels). Reprinted with permission from ref. 42. Copyright 2006 American Chemical Society.

Polymers containing mixed pendants. Poly-III and poly-IV, which contain two different pendants in the strand, i.e., –$Re(CO)_3(phen)^+$ and –$Re(CO)_3(bpy)^+$, form nanometric aggregates in solution phase. The bimodal relaxation time spectra registered in DLS experiments with poly-III and poly-IV reveal the existence of particle sizes between 3 and 14 nm in equilibrium, with bigger particles with radii between 40 and 300 nm. Given the hydrodynamic radius, 221 ± 9 nm for poly-III and 294 ± 5 for poly-IV, the aggregates must be bigger in poly-IV than in poly-III. It appears that the larger the Re(I) load in the polymer, the bigger is the size of the aggregates. TEM images obtained for poly-III and poly-IV also show that the aggregates of poly-IV are larger than those of poly-III. Radii obtained from the DLS experiments are larger than those observed in the TEM micrographs. Similar differences were observed between the DLS hydrodynamic radii and those extracted from the TEM images of poly-II. However, these differences in poly-III and poly-IV are much larger, making the radii determined from TEM images a factor 2 smaller.[41]

Solvent effects on morphologies: nanoaggregation on polymers poly-V - poly-IX. The morphologies of poly-V - poly-IX were also studied by TEM.[19] Multiple morphologies of aggregates from these Re(I) polymers were obtained by using different solvents. TEM images of CH_3CN and CH_2Cl_2-cast films of the polymers are shown in Figure 5 and Figure 6, respectively. Polymer morphologies differed when the cast films were obtained either from CH_3CN or CH_2Cl_2 solutions. When the solvent was CH_3CN (Figure 6), poly-VI in the solid phase, Re(I) complexes aggregate and form isolated nanodomains that are dispersed in the P4VP backbone. Aggregate dimensions range between 80 and 160 nm, and aggregates are mainly spherical in shape. However, poly-V does not aggregate to form large nanodomains, and only small spherical objects with diameter between 5 and 30 nm are observed. TEM images suggest the formation of aggregates of increasing size when comparing TEM images from poly-VII to poly-IX. The situation is completely different in CH_2Cl_2. Figure 6 shows TEM images of CH_2Cl_2-cast films of polymers poly-V - poly-IX. Vesicles were obtained for poly-V, poly-

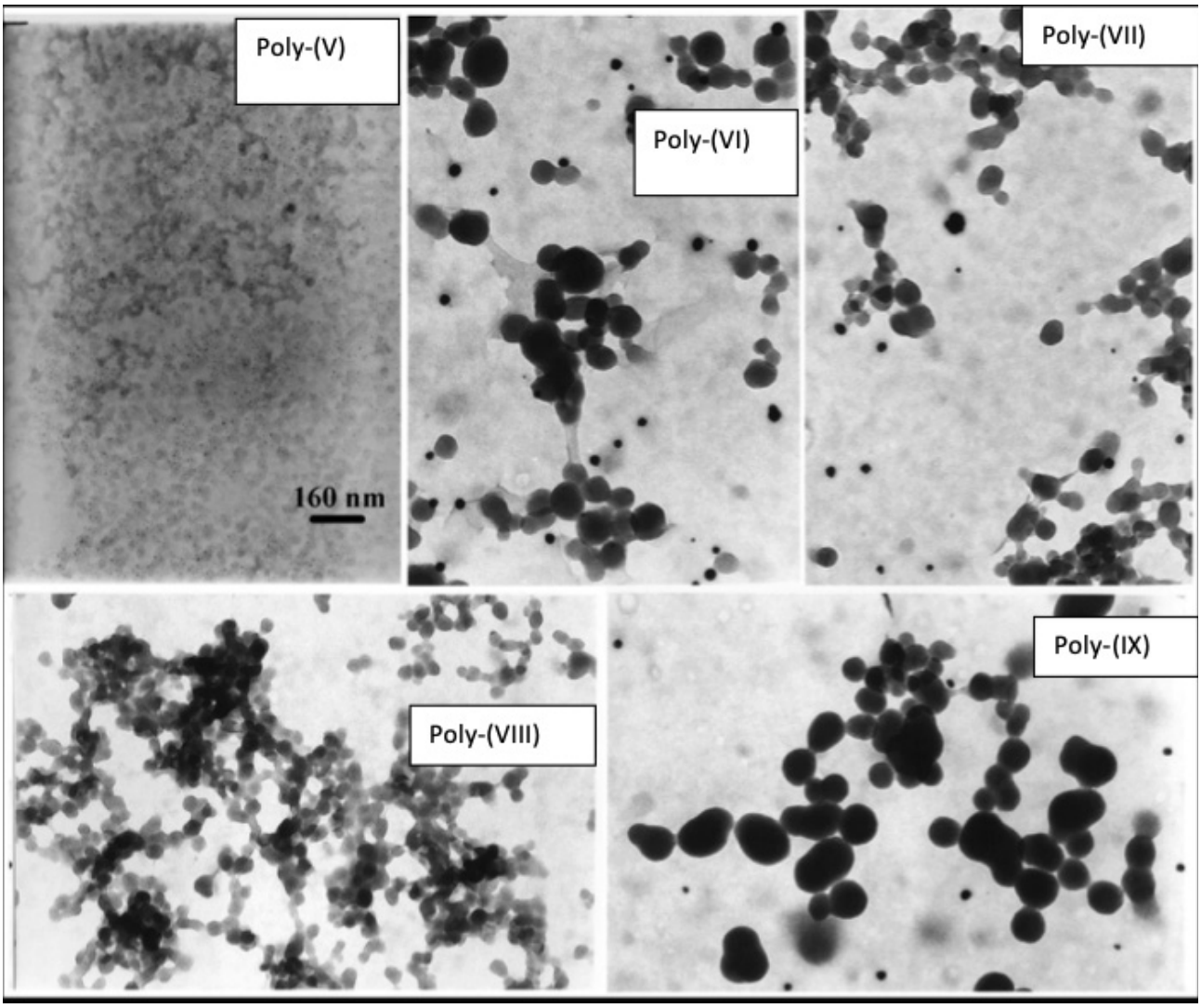

Figure 5. Acetonitrile-cast films in polymers poly-(V), poly-(VI), poly-(VII), poly-(VIII) and poly-(IX). The same scale bar applies to all films in the Figure. Reprinted with permission from ref. 19. Copyright 2008 American Chemical Society.

VII, and poly-VIII. The vesicular nature is evidenced by a higher transmission in the center of the aggregates than around their periphery in the TEM pictures. Vescicle sizes are very polydisperse, with outer diameters ranging from 140 nm to large compound vesicles with diameters of up to 1.4 μm. More interestingly, poly-VI formed branched tubular structures intertwined in a net. The morphologies shown for poly-IX are the intermediate shape of vesicles and tubules. We can rationalize the solvent effect upon aggregation of Re(I) polymers as follows. P4VP is nearly insoluble in CH_3CN, but this solvent is a good one for the Re(I) polymers. Then, it is possible that the inner core of the nanodomains present in CH_3CN is formed mainly by the free pyridines of the Re(I) polymers and the outer part is mainly constituted by the solvated Re(I) pendants. The situation is reversed in CH_2Cl_2, as this is a good solvent for P4VP. Moreover, poly-(I) and poly-(II) cannot be dissolved in CH_2Cl_2, while the solubility of polymers poly-V - poly-IX in this solvent is considerably lower than in CH_3CN. In vesicles, however, a pool of CH_2Cl_2 molecules may be solvating the uncoordinated pyridines of the polymer in the inner and outer regions of the vesicle, while the Re(I) pendants might be mainly remaining inside the membrane of the vesicle.

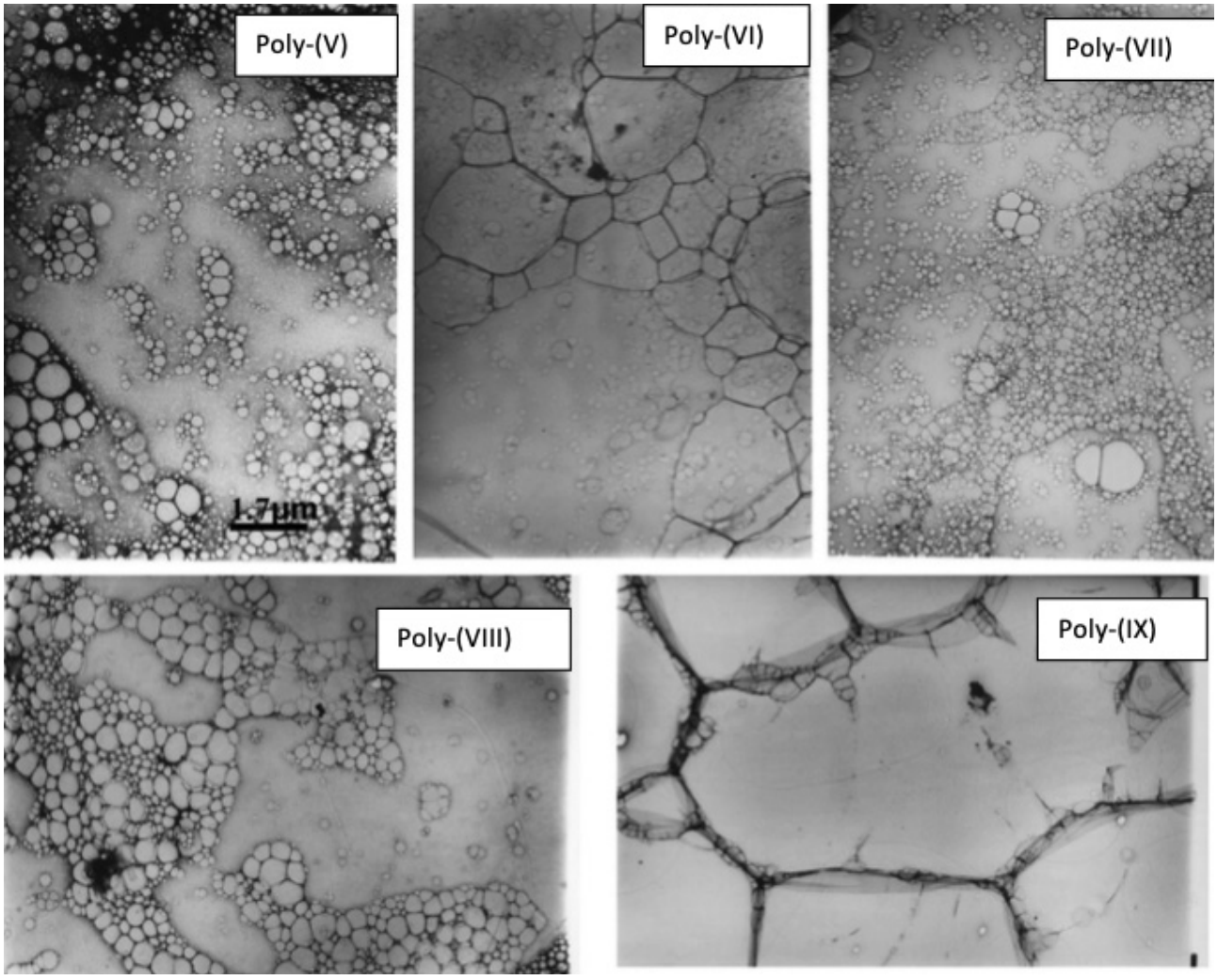

Figure 6. Dichloromethane-cast films in poly-(V), poly-(VI), poly-(VII), poly-(VIII) and poly-(IX). The same scale bar applies to all films in the Figure. Reprinted with permission from ref. 19. Copyright 2008 American Chemical Society.

5. A correlation between backbone photophysical properties and morphological changes in poly-I

When a deaerated solution of poly-I in CH_3CN is irradiated at λ_{exc} = 350 nm, the characteristic luminescence of pendants –$Re(CO)_3phen^+$ chromophores showing a broad unstructured band centered at λ_{max} = 550 nm is observed. In this work,[45] a

complementary study to the previous one in the literature,[42] it has been established that the luminescence lifetime of excited –$Re(CO)_3phen^+$ pendant chromophores in poly-I is dependent on the polymer concentration. Luminescence lifetimes were calculated from traces obtained with polymer concentrations corresponding to a total chromophore concentration varying from [Re] = 2 x 10^{-5}M to 4 x 10^{-4}M. In the range of [Re] = 2 x 10^{-5}M to 1 x 10^{-4}M, a sum of two exponential functions was needed, with lifetimes $\tau_{em,1}$ and $\tau_{em,2}$ to fit the luminescence decay profiles. The dependences of $\tau_{em,1}$ and $\tau_{em,2}$ on the Re chromophore concentration between 2 x 10^{-5}M and 4 x 10^{-4}M is shown in Figure 7. The shorter lifetime, $\tau_{em,1}$ = 55 ± 7 ns, remains essentially constant between 2 x 10^{-5}M and 1 x 10^{-4}M, while the longer lifetime, $\tau_{em,2}$, increased monotonically from 240 to 490 ns. When [Re] > 1 x 10^{-4}M, the luminescence decay was fitted without deviation to a single exponential with a lifetime τ_{em} = 581 ± 10 ns, which is independent of polymer concentration in the concentration range 1 x 10^{-4}M < [Re] < 4 x 10^{-4}M.

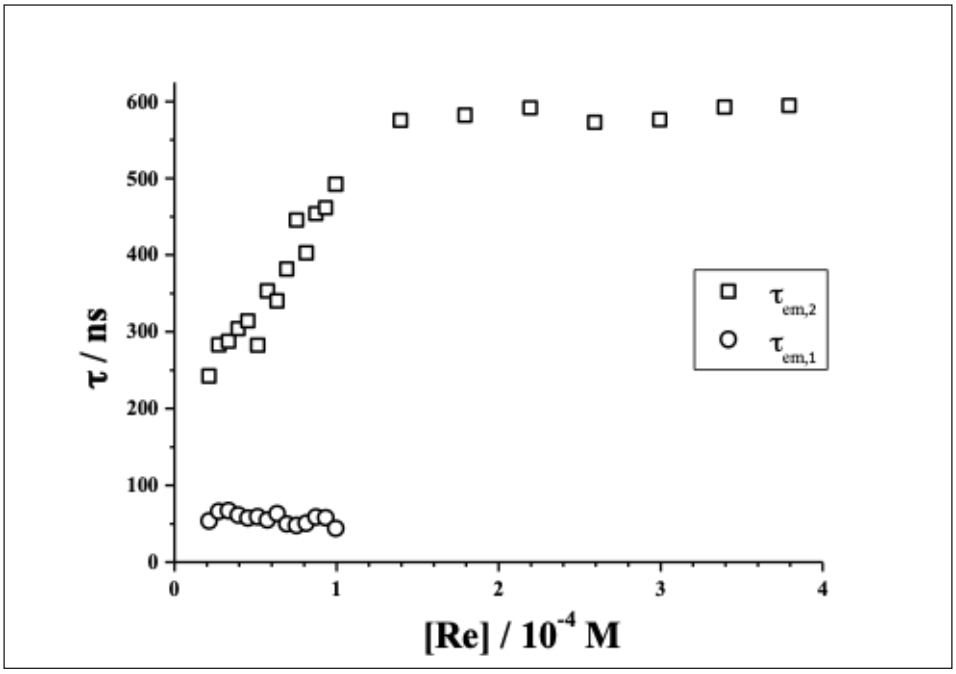

Figure 7. Dependence of poly-I luminescence lifetimes, $\tau_{em,1}$ and $\tau_{em,2}$, on Re(I) chromophores concentration.

The degree of polymer protonation at different [$HClO_4$]/[py] ratios was followed by spectrofluorometric techniques. In the steady-state experiments, the total chromophore concentration, [Re] = 2 x 10^{-5}M, was kept constant and the deaerated solutions were irradiated at 350 nm. A large increase in the luminescence of poly-I was observed when Re-free pyridines in poly-I were protonated with $HClO_4$ (Fig. 8), with more than an 8-fold increase in total luminescence. Neither the changes on the band shape nor a band shift accompanied the increase in luminescence quantum yield. The effect of pyridine protonation on poly-I luminescence lifetime was studied at two poly-I concentrations, i.e., [Re] = 4 x 10^{-5}M and 1.6 x 10^{-4}M, with [$HClO_4$]/[py] ratios varying from 0.1 to 1.5. Photophysical observations have shown that these poly-I concentrations are those where the decay of luminescence exhibits biexponential and monoexponential kinetics, respectively. In solutions where [Re] = 4 x 10^{-5}M, luminescence decay kinetics changes from a biexponential regime (when no acid is present) to a mono-exponential law over the whole [$HClO_4$]/[py] range. A lifetime, τ_{em} = 450 ± 10 ns, was calculated for the monoexponential decay of the luminescence. When the total concentration of pendants is 1.6 x 10^{-4}M, a longer lifetime, τ_{em} = 560 ± 10 ns, was obtained for luminescence monoexponential decay over the whole range of [$HClO_4$]/[py] values.

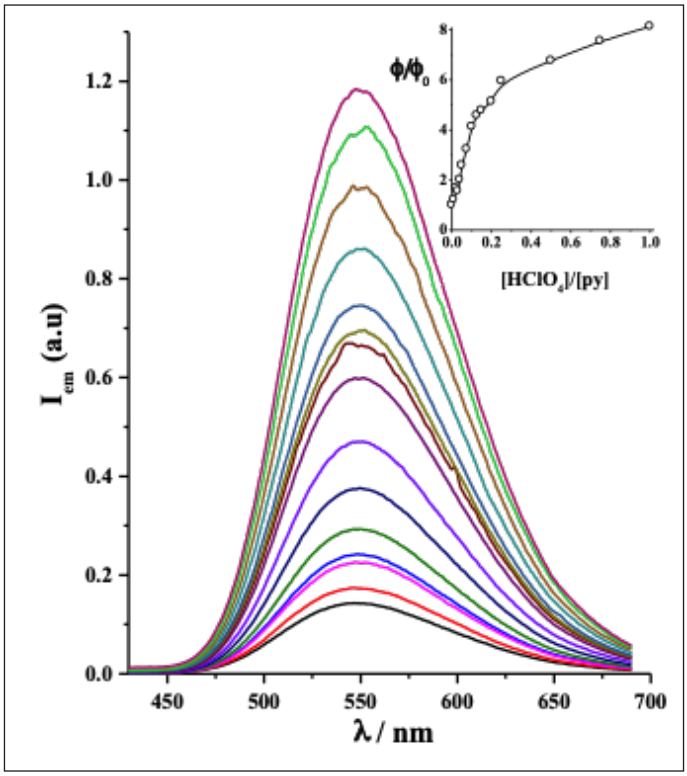

Figure 8. Re-P4VP luminescence spectra at different $[HClO_4]/[py]$ ratios.
Inset shows the relative increase in luminescence quantum yield as a function of the $[HClO_4]/[py]$ ratio. $[HClO_4]/[py]$ = 0; 0.01; 0.02; 0.03; 0.04; 0.05; 0.075; 0.10; 0.125; 0.15; 0.20; 0.25; 0.50; 0.75; 1.00.

TEM and AFM studies[45] on poly-I and its protonated form, poly-IH_n^{n+}, have shown that (i) the morphology of Re-P4VP polymers is concentration-dependent and (ii) protonation of poly-I polymers alters strongly their morphology. Hereafter, the polymer concentration will be expressed in chromophore units, i.e. [Re]. The morphology of the poly-I at low concentrations ([Re] between 2 x 10^{-7} and 2 x 10^{-5} M, can be described by the coexistence of small objects at polymer scales (diameters below 10 nm) with larger nano aggregates (diameters between 200 and 1000 nm) as well as long fibers at the micrometer scales in a non-homogeneous distribution of aggregate sizes. When polymer concentration is higher ([Re] = 2 x 10^{-5} M), TEM experiments show that poly-I morphology is characterized by nearly spherical nano-domains exhibiting a homogeneous distribution centered at about 25 nm in diameter. After protonation of poly-I, its morphology is strongly affected – at low concentration of the Re(I) polymers, small objects at polymer scales are clearly observed and the fiber-structure is evident; at higher concentration of the Re(I) polymers, polymer morphology shifts after protonation from a homogeneous distribution of spherical nanodomains to a bicontinuous bilayer with attached small objects at polymer scales sizes.[45] Figure 9 shows an example of the morphological changes experienced by poly-I after protonation observed by TEM.

The results have shown that the photophysical and photochemical properties of poly-I and its protonated form are intrinsically associated with medium-imposed polymer morphologies. Those morphological changes have direct impact on the photophysical properties of poly-I polymers and are responsible of (i) the enhancement of luminescence lifetime when increasing polymer concentration and (ii) the nearly 8-fold increase of luminescence quantum yield after protonation of the Re(I) polymer.

The dependence of $\tau_{em,2}$ on polymer concentration, Fig. 7, is another manifestation of the different environments where the luminescent ^{3}MLCT excited state is formed. Accordingly, the luminescence decay of poly-I is bi-exponential at [Re] < 1 x 10^{-4}M, but it becomes mono-exponential when [Re] > 1 x 10^{-4}. Observations made via TEM and AFM show that these environments are the result of a concentration-dependent morphology. Photophysical observations are interpreted, therefore, in terms of medium-destabilized charge-transfer excited states, labeled $^3MLCT_{md}$, present in some chromophores within a strand of polymer. $^3MLCT_{md}$ excited states may decay to the ground state or they can transfer their excess electronic energy to other chromophores producing medium-stabilized charge-transfer excited states, $^3MLCT_{ms}$. The multiple types of aggregates observed with TEM and AFM in poly-I diluted solutions are consistent with the coexistence of $^3MLCT_{md}$ and $^3MLCT_{ms}$ excited states. By contrast, at higher polymer concentrations, e.g., [Re] = 2 x 10^{-4}M, sample inspection using TEM reveals the presence of nearly spherical aggregates with ~25 nm diameters. Therefore,

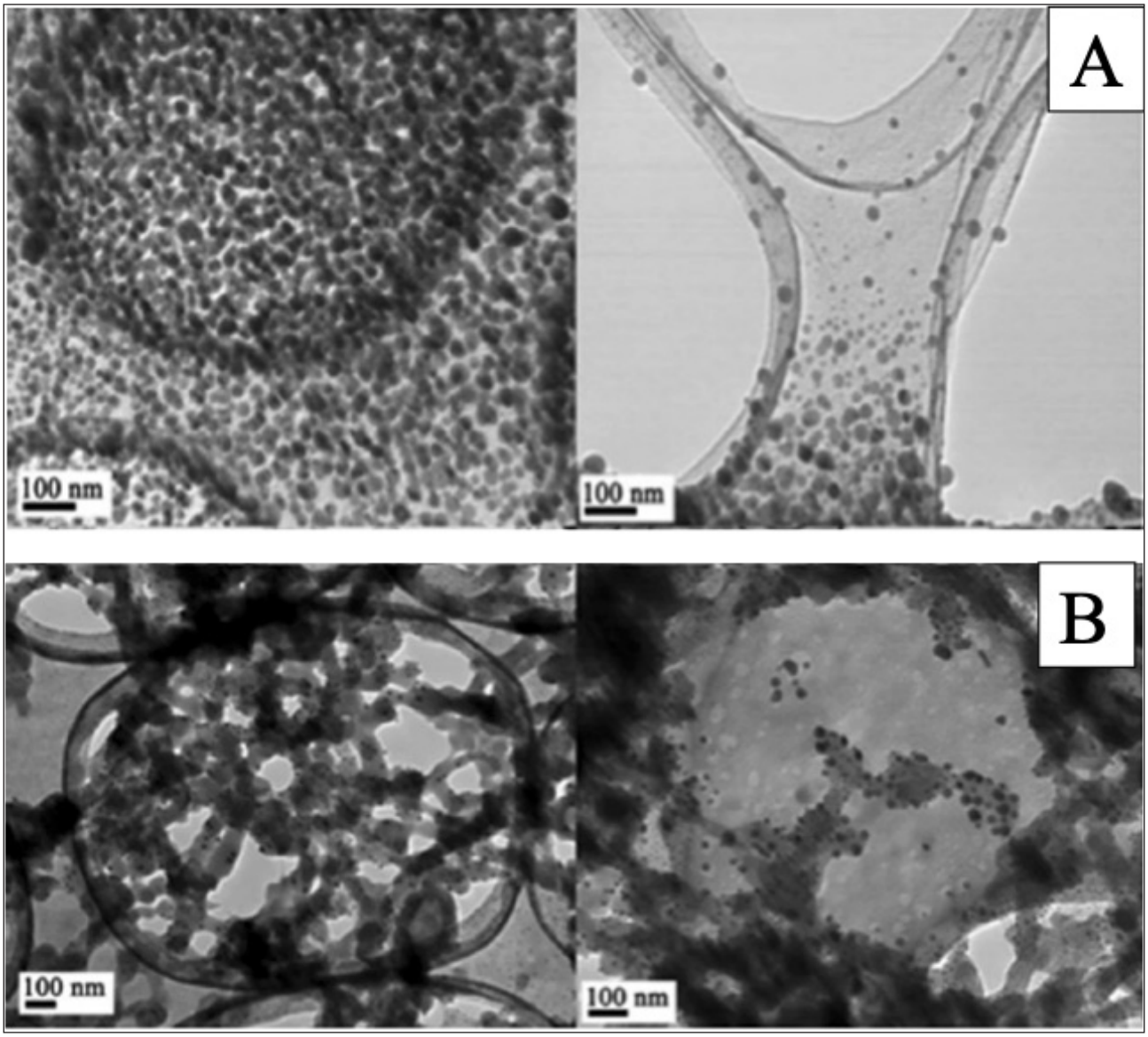

Figure 9. (A) TEM images for poly-I. (B) TEM image for poly-IH_n^{n+}. Both TEM images were taken from CH_3CN cast films of the polymers prepared with [Re] = 2 x 10^{-4}. In (B), $HClO_4$ was added to the solution of poly-I with [$HClO_4$]/[py] = 1.5.

some critical mass of polymer between [Re] < 1 x 10^{-4}M and [Re] = 2 x 10^{-4}M must provide enough material to form the spherical aggregates. Based on the change in the mechanism of the luminescence decay accompanying the formation of spherical aggregates, it can be concluded that the distribution of oligomers when [Re] = 2 x 10^{-4}M is more homogeneous than when [Re] = 2 x 10^{-5}M. Accordingly, the regime change from a bi-exponential decay to a mono-exponential decay of luminescence is tuned by the concentration-dependent morphology of poly-I. The protonation of the Re(I) polymer induces an 8-fold increase in luminescence quantum yield and a significant increase in $\tau_{em,2}$, from 300 ns to 450 ns for [Re] = 4 x 10^{-5}M. Moreover, nearly identical luminescence lifetimes were obtained for the mostly protonated Re(I) polymer and poly-I in the absence of $HClO_4$ acid with solutions having in both cases [Re] = 1.6 x 10^{-4}M. These facts suggest that the increase in luminescence quantum yield and lifetime lengthening are the result of morphological changes caused by poly-I protonation in diluted solutions. To some extent, the morphologies of poly-I in concentrated solutions and in diluted acid solutions must be alike or, if they are different, they exert similar perturbations on chromophore photophysics.

Binding of Cu(II) species and luminescence quenching in poly-II nanoaggregates. The addition of an acetonitrile solution of CuX_2 (X = Cl or CF_3SO_3) to an acetonitrile solution of the polymer poly-II ([Re] = 8 x10^{-4} M, $[py]_{uncoordinated}$ = 1.5x10^{-3}M) produces a rapid coordination of the Cu(II) species to the uncoordinated pyridines poly-II. Binding constant

values of K_b = 2 x 10^4 M^{-1} and n= 1.8 and K_b =1 x 10^5 M^{-1} and n = 3.0 were obtained for the binding of $CuCl_2$ or $Cu(CF_3SO_3)_2$ to the Re(I) polymer, respectively, n being the average size of a binding site.[39] It can be assumed, then, that the complexation of $CuCl_2$ to poly-II proceeds with a lower average coordination number than the complexation of $Cu(CF_3SO_3)_2$ to the Re(I) polymer, with approximate coordination numbers being 2 and 3, respectively. As noted above (*vide supra*), the binding of Cu(II) to poly-II produces the breakage of the nanoaggregates and yields a wide distribution of particle sizes ranging from a few nanometers at polymer scales to a few hundreds of nanometers covering micelle scales.[39]

The coordination of Cu(II) species to poly-II produces the quenching of the ^{3}MLCT excited state by energy transfer processes that are more efficient than those in the quenching of the luminescence of $[pyRe(CO)_3bpy]^+$ by Cu(II). Additionally, with poly-II, the kinetics of the quenching by Cu(II) does not follow a Stern-Volmer behavior. Moreover, although in the quenching poly-II luminescence by $Cu(CF_3SO_3)_2$, the Φ_0/Φ ratio shows a sigmoid dependence on $Cu(CF_3SO_3)_2$ concentration with a limiting value of $\Phi_0/\Phi \sim 6$, the quenching by $CuCl_2$ does not show a plateau on Φ_0/Φ.[39] Conversely, the reductive redox quenching of the Re(I) polymer's MLCT excited state by TEOA follows a Stern-Volmer kinetics. The striking differences found in the quenching mechanisms with Cu(II) or TEOA are a consequence of the strong chemical interaction (binding) of Cu(II) to the P4VP backbone of the Re(I)-polymer. All quenching processes, either by Cu(II) or TEOA, are more efficient in the polymer than in $[pyRe(CO)_3bpy]^+$.[39]

6. Resonance energy transfer between $–Re(CO)_3(tmphen)^+$ and $–Re(CO)_3(NO_2\text{-phen})^+$ pendants in the solution phase photophysics of poly-V, poly-VI, poly-VII, poly-VIII and poly-IX

We have applied ligand substitution reactions of the Re(I) complexes to the derivatization of polymers poly-V, poly-VI, poly-VII, poly-VIII and poly-IX. These polymers consist of a poly-4-vinylpyridine backbone with pendant chromophores $–Re(CO)_3(NO_2\text{-phen})^+$ and $–Re(CO)_3(tmphen)^+$, with a general formula of $\{[(vpy)_2vpyRe(CO)_3(tmphen)^+]\}_n\{[(vpy)_2vpyRe(CO)_3(NO_2\text{-phen})^+]\}_m$. The n/m ratio was changed from 9 to 1, maintaining n + m ~ 200. We further studied energy transfer processes between pendant chromophores in these polymers.

Steady State Photophysics. Deaerated solutions of polymers poly-V, poly-VI, poly-VII, poly-VIII and poly-IX with total concentration of the Re(I) chromophores equal to or less than 1×10^{-4} M in CH_3CN were irradiated at 380 nm to record their emission spectrum. The emission spectrum of poly-V in deoxygenated CH_3CN at room temperature exhibited an unstructured band centered at 520 nm. Poly-VI is non-luminescent. Polymers poly-VII, poly-VIII and poly-IX have luminescence spectra, which are the same in shape as that of poly-V. The luminescence quantum yield (Φ_{em}) of poly-V is ~ 0.03. Poly-VII has a Φ_{em} that is nearly $^1/_3$ lower than that of poly-V. Φ_{em} decreases monotonically from poly-VII to poly-IX. Table 2 summarizes all measured values for Φ_{em}. It shows also the values measured for Φ_{em} with molar mixtures of polymers poly-V and poly-VI, i.e., to obtain the same $m/(n + m)$ in the mixture as there is in polymers poly-VII, poly-VIII and poly-IX. The values of Φ_{em} determined for mixtures 90% poly-V + 10% poly-VI, 75% poly-V + 25% poly-VI, and 50% poly-V + 50% poly-VI are noticeably higher than those of poly-VII, poly-VIII and poly-IX, respectively. For instance, while Φ_{em} for the mixture 50% poly-V + 50% poly-VI is nearly ½ Φ_{em} for poly-V , Φ_{em} for polymer poly-IX is nearly 2 orders of magnitude lower than that corresponding to poly-V.[19]

Table 2. Photophysical properties of polymers poly-V, poly-VI poly-VII, poly-VIII and poly-IX in acetonitrile at room temperature. Data taken from ref. 19

	ϕ_D [a, b]	τ_{fast}, ns[c]	τ_{slow}, µs[c]	Energy transfer efficiency $E_T^j = 1 - \frac{\phi_D^j}{\phi_{mb}^j}$
Polymers				
poly-V	0.035	(7.4 ± 0.9)x10^2	3.4 ± 0.5	
poly-VI	< 10^{-4}	0.23 ± 0.01[d]	--	
poly-VII	0.013	(1.1 ± 0.2)x10^2	1.13 ± 0.07	0.58
poly-VIII	0.0038	50 ± 10	0.59 ± 0.07	0.85
poly-IX	0.0007	< 10	0.047 ± 0.006	0.94
Molar blends				
90% poly-V + 10% poly-VI	0.031			
75% poly-V + 25% poly-VI	0.026			
50% poly-V + 50% poly-VI	0.0125			

[a] Emission quantum yields of poly-V, poly-VI, poly-VII, poly-VIII and poly-IX. Error ± 10%.
[b] Emission quantum yields, φ_D, measured with molar blends of poly-V and poly-VI in order to obtain the same m/(n+m) in the blend as there is in polymers poly-VII, poly-VIII and poly-IX. Error ± 10%. See text for details.
[c] Obtained from a curve fit analysis with two exponentials from transient absorbance decays in flash photolysis experiments (λ_{ex}= 351 nm).
[d] Obtained from a transient absorbance monoexponential decay in femtosecond laser photolysis experiments (λ_{ex}= 387 nm).

Time-Resolved Absorption Spectroscopy of poly-V, poly-VI, poly-VII, poly-VIII and poly-IX. Optical excitation of the MLCT absorption bands of the polymers was carried out with a 351 nm excimer laser flash photolysis set-up to record the transient absorption spectra in the 15 ns to microsecond time domain. The transient spectra observed after the 10 ns irradiation of poly-V, poly-VII, poly-VIII and poly-IX solutions in N_2-deaerated CH_3CN decayed over a period of several microseconds. A sum of two exponential functions was needed to fit the oscillographic traces with lifetimes τ_{fast} and $\tau_{slow;}$ see Table 2. Transient spectra recorded with either polymer at times immediately after the laser pulse decay, i.e. 20 ns, showed the spectra of the $^3MLCT_{Re\text{-}tmphen}$ excited states decaying by radiative and non-radiative processes.[19] The same spectral features were observed in the generated transients of poly-V, poly-VII, poly-VIII and poly- IX. However, the initial intensity of the spectrum decreases from poly-V, poly-VII, poly-VIII and poly-IX. Since the excited states of poly-VI decayed much faster than the ones of poly-V, poly-VII, poly-VIII or poly- IX, femtosecond techniques were used to record the femtosecond to nanosecond time domain transient absorption spectra of poly-VI. The spectra of the excited states produced ~4 ps after the 387 nm flash irradiation of this polymer consist of three absorption bands, two with maxima at 450 and 600 nm, respectively, and a third one with λ_{max} > 750 nm.[19] It decays monoexponentially over a period of 1600 picoseconds with a lifetime of 230 ps.[19]

Polymer luminescence decays were also measured in N_2-deaerated CH_3CN solutions of poly-V, poly-VII, poly-VIII and poly-IX with λ_{exc} = 337 nm. The luminescent profiles of poly-V could be fitted by a single exponential function with a lifetime of τ_{em} = 5.12 µs. However, the decay of the luminescent profiles for poly-VII, poly-VIII and poly-IX were non-exponential and were fitted following a modification of the Förster treatment, eq. 7:[19]

$$N_t = N_0 \exp\left[-\frac{t}{\tau_D} - a\sqrt{t/\tau_D}\right] \quad (7)$$

where N_t is the number of molecules that survived excitation at time t, and τ_D is the excited state lifetime of the donor in the absence of transfer. a is a parameter proportional to the density of acceptor quenching sites which can be calculated according to $a = \frac{4}{3}\pi^{3/2}\rho R_F^3$ where ρ stands for the number of quenching sites per volume and R_F is the Förster critical radius. N_t relates the form of the decay curve to a certain quenching mechanism (in our case Forster's dipole-dipole energy transfer) and two structural quantities, namely quenching site density and critical radius R_F. The number of quenching sites within the critical radius is given by $N = \frac{a}{\sqrt{\pi}}$.

Poly-VII, poly-VIII and poly-IX luminescence decay profiles were fitted using Equation 7 with the values of a = 1.90, 4.6 and 19.3, respectively, and τ_D = 5.12 μs.[19] Values of $N \approx 1.1$; 2.6 and 11 can be calculated for poly-VII, poly-VIII and poly-IX using the vales of a = 1.90, 4.6 and 19.3, respectively. A calculation of R_F for the present system gives a value of 10.7 Å.[19] Using this value of R_F and the values of a obtained above from the luminescence decay fitting, values of ρ = 2.1x 10^{-4}, 5.05 x 10^{-4} and 2.1 x 10^{-3} $N_{acceptors}$/Å^3 can be calculated for polymers poly-VII, poly-VIII and poly-IX, respectively. These numbers compared well with the number of quenching neighbors estimated roughly from a molecular modeling of the polymers.[19]

From the comparison of Φ_{em} values for polymers poly-VII, poly-VIII and poly-IX with the corresponding Φ_{em} of the molar blends 90% poly-V + 10% poly-VI, 75% poly-V + 25% poly-VI, and 50% poly-V + 50% poly-VI, it can be inferred that the substitution of pendants $Re(CO)_3(tmphen)^+$ by pendants $Re(CO)_3(NO_2\text{-phen})^+$ in the P4VP backbone produces a decrease in Φ_{em} that is in proportion to the number of $Re(CO)_3(NO_2\text{-phen})^+$ pendants relative to that of $Re(CO)_3(tmphen)^+$ pendants due to an energy transfer process that involves the excited states $MLCT_{Re\rightarrow tmphen}$ and $MLCT_{Re\rightarrow NO2\text{-phen.}}$

Φ_{em} of the molar blends 90% poly-V + 10% poly-VI, 75% poly-V + 25% poly-VI, and 50% poly-V + 50% poly-VI can be compared to the Φ_{em} values that would have been expected for polymers poly-VII, poly-VIII and poly-IX if no energy transfer between $-[Re(CO)_3(tmphen)^+]^*$ and $-Re(CO)_3(NO_2\text{-phen})^+$ pendants had occurred, eqs. 10-11:

$$\Phi_D = \left(\frac{A}{A_T}\right)\Phi_D{}^0 \qquad (10)$$

$$\frac{A}{A_T} = \frac{n\varepsilon_{\lambda,n}}{n\varepsilon_{\lambda,n} + m\varepsilon_{\lambda,m}} \qquad (11)$$

Where A is the absorbance of donor $-Re(CO)_3(tmphen)^+$ at wavelength λ, A_T is the total absorbance of the solution, and $\varepsilon_{\lambda,n}$ and $\varepsilon_{\lambda,n}$ are the molar extinction coefficients of donor $-Re(CO)_3(tmphen)^+$ and acceptor $-Re(CO)_3(NO_2\text{-phen})^+$ at wavelength λ, respectively, and $\Phi_D{}^0$ is the emission quantum yield of the donor, i.e. 0.0347 for poly-V. Given the values of 5.5x10^5 and 7.8x10^5 $M^{-1}cm^{-1}$ for the extinction coefficients of poly-V and poly-VI at 380 nm, Φ_D values of 0.0298, 0.0236 and 0.0142 can be calculated for poly-VII, poly-VIII and poly-IX, respectively. Those Φ_D values are similar to the experimental values measured for the molar blends 90% poly-V + 10% poly-VI, 75% poly-V + 25% poly-VI, and 50% poly-V + 50% poly-VI, which are 0.031, 0.026 and 0.0125, respectively (see Table 2). Therefore, it can be concluded that there is no bimolecular (i.e. intermolecular) quenching between excited $-Re(CO)_3(tmphen)^+$chromophores in polymers poly-V and acceptors $-Re(CO)_3(NO_2\text{-phen})^+$ in polymers poly-VI in the blends.

Regarding the energy transfer process that quenches progressively the emission of the excited $-Re(CO)_3(tmphen)^+$ (donor D) pendants with the increasing number of $-Re(CO)_3(NO_2\text{-phen})^+$ (acceptor A) pendants in polymers poly-VII, poly-VIII and poly-IX, the crucial point is that, when passing from polymer poly-VII to poly-VIII and then to poly-IX, the probability of a donor D to be in the vicinity of an acceptor A increases.

Energy transfer efficiency between D and A in polymers poly-VII, poly-VIII and poly-IX can be calculated according to:

$$E_T^j = 1 - \frac{\Phi_D^j}{\Phi_{mb}^j} \qquad (12)$$

where E_T^j represents energy transfer efficiency in polymer j [j = poly-VII, poly-VIII and poly-IX], Φ_D^j represents emission quantum yields for polymers poly-VII, poly-VIII and poly-IX, and Φ_{mb}^j are the emission quantum yields of the molar blends 90% poly-V + 10% poly-VI, 75% poly-V + 25% poly-VI, and 50% poly-V + 50% poly-VI**,** respectively. The experimental E_T^j values for polymers poly-VII, poly-VIII and poly-IX are 0.58, 0.85 and 0.94 respectively (Table 2).

Taking the E_T^j calculated above for polymers poly-VII, poly-VIII and poly-IX, mean values for the energy transfer rate constant between $MLCT_{Re\rightarrow tmphen}$ and $MLCT_{Re\rightarrow NO2\text{-}phen}$ can be calculated in these polymers with the aid of Equation 13:

$$\overline{k_{ET}} = \frac{1}{\tau_D}\left(\frac{E_T^j}{1-E_T^j}\right) \qquad (13)$$

The values of $\overline{k_{ET}}$ obtained for polymers poly-VII, poly-VIII and poly-IX are $2.7x10^5$, $1.1x10^6$ and $3.1x10^6$ s^{-1}, respectively. It should be noted that those $\overline{k_{ET}}$ values are only average contributions in the polymers.[19]

7. MLCT luminescence quenching by amines: aggregation decreases the reorganization energy favoring the observation of the Marcus inverted effect

Understanding the factors that determine electron-transfer (*ET*) rates is of considerable importance, due to *ET* ubiquity and the essential roles it plays in many physical, chemical and biological processes. Different factors govern the kinetics of *ET* reactions, such as solvent environment, free energy of reaction (ΔG) and electronic coupling. *ET* rates should follow a parabolic dependence on ΔG according to the remarkable prediction of Marcus theory. In the classical limit, the theory predicts a bell-shaped Gibbs energy-rate relationship for reactions in condensed media: rate constants are expected to be small for weakly exothermic reactions, increase to a maximum for moderately exothermic reactions (the *normal region*), and decrease for highly exothermic electron transfer reactions in the so-called *inverted region*. Due to the lack of the experimental evidence, a lot of controversy was generated by the theoretical prediction of this *inverted region*. In fact, the confirmation of the *inverted effect* took a lapse of about 25 years after its postulation. After that, the *inverted region* has been observed experimentally in many electron transfer systems.[37] Experimental evidence for the Marcus *inverted region* in the bimolecular *ET* reactions is, however, very rare.[49] In most bimolecular *ET* reactions, mainly due to the influence of the diffusional rate of the reactants on the effective reaction rates, the variation in the *ET* rates with the ΔG of the reactions follows the Rehm-Weller type of behavior.[50] There are two main obstructions to observing the Marcus inverted region in bimolecular ET reactions, namely, (i) diffusion of the reactants and (ii) lack of availability of suitable donor–acceptor series to achieve very high reaction exothermicities. The first shortcoming may be reduced if *ET* is carried out in systems where reactants are confined into micelles and/or nano aggregates where their movements may be highly restricted. We decided to test the ability of our polymers in their aggregates to overcome the first drawback. Thus, we decided to compare ^{3}MLCT luminescence quenching of $–Re(CO)_3bpy^+$ chromophores by amines in poly-II with the ^{3}MLCT luminescence quenching of $[pyRe(CO)_3bpy]^+$ chromophores by the same amines, in order to see if the formation of nano aggregates in poly-II (*vide supra*) could have any effect on quenching kinetics behavior.

Forward electron transfer. The reductive quenching of the ^{3}MLCT excited state of $[pyRe(CO)_3bpy]CF_3SO_3$ and poly-II by amines produces the oxidized form of the amine and the reduced radical of the rhenium complex; eqs. 14,15

$$[pyRe(CO)_3bpy^+]^* + NR_3 \xrightarrow{k_{q,1}} pyRe(CO)_3bpy^\bullet + NR_3^{\bullet+} \qquad (14)$$

$$–[pyRe(CO)_3bpy^+]^* + NR_3 \xrightarrow{k_{q,2}} -Re(CO)_3bpy^\bullet + NR_3^{\bullet+} \qquad (15)$$

where $[pyRe(CO)_3bpy^+]^*$ and $–[Re(CO)_3bpy^+]^*$ denote the MLCT excited states in $pyRe(CO)_3bpy^+$ and in a pendant $–Re(CO)_3bpy^+$ chromophore of poly-II, and $k_{q,1}$ and $k_{q,2}$ denote the bimolecular rate constants for $pyRe(CO)_3bpy^+$ and poly-II, respectively.

The results of the quenching experiments are shown in Table 3. The data were plotted according to the Stern-Volmer equation; eq. 16

$$\frac{\tau_0}{\tau} = 1 + k_q\tau_0[NR_3] \qquad (16)$$

where τ_0 is the excited state lifetime in the absence of quencher and τ is the luminescence lifetime in the presence

of quencher. The plots were linear over the range of quencher concentrations used and the intercepts were unity as expected.[37] k_q values, collected in Table 3, were determined from the slopes of the lines using τ_0 = 245 and 203 ns for $[pyRe(CO)_3bpy]CF_3SO_3$ and poly-II, respectively.[37]

Table 3. Quenching rate constants (k_q ± 2 SE) of MLCT excited states of poly-II and $pyRe(CO)_3(bpy)^+$ in acetonitrile by aliphatic and aromatic amines. Data taken from ref. 37

			Poly-II	$pyRe(CO)_3(bpy)^+$
Quencher	$E_{1/2}$, V(vs. SCE)	ΔG/eV	$k_q/M^{-1}s^{-1}$	$k_q/M^{-1}s^{-1}$
N,N,N',N'-tetramethyl 1,4-phenylenediamine	0.12	-1.16	(4.8±0.8) x10^9	(2.0±0.2) x 10^{10}
1,4-phenylenediamine	0.26	-1.02	(1.1±0.6) x10^{10}	(1.3±0.1) x 10^{10}
1,2-phenylenediamine	0.40	-0.88	(1.5±0.1) x10^{10}	(1.30±0.04) x 10^{10}
DABCO	0.56	-0.72	(7.8±0.8) x10^9	(1.02±0.02) x 10^{10}
N,N,N',N'-tetramethylethylenediamine	0.87	-0.41	(2.1±0.6) x10^9	(1.0±0.2) x 10^9
N,N di-isopropyl-ethylamine	0.89	-0.39	(6±1) x10^9	(5±1) x10^9
Aniline	0.93	-0.35	(6.7±0.4)x 10^9	(5.5±0.4) x 10^9
Triethylamine	0.99	-0.29	(2.1±0.2) x10^9	(1.00±0.06) x 10^9
N,N,N',N'-tetramethyl-diaminomethane	1.06	-0.22	(5±1) x 10^8	(2.45±0.06) x 10^8
Diethylamine	1.14	-0.14	(1.3±0.2) x 10^8	(1.4±0.2) x 10^8
Di-isopropylamine	1.31	0.03	(1.1±0.2) x 10^8	(2.6±0.2)x10^7
Dibencylamine	1.36	0.08	(8±1) x 10^6	(8±1) x 10^6
n-butylamine	1.39	0.11	(1.3±0.1) x 10^7	(6±1) x 10^6

Electron transfer mechanism. The following kinetic scheme may be considered for the forward electron transfer reaction:[37]

$$(A^+)^* + D \underset{k_{-d}}{\overset{k_d}{\rightleftharpoons}} [(A^+)^*, D] \underset{k_{-e}}{\overset{k_e}{\rightleftharpoons}} [(A^\bullet), D^{\bullet+}] \xrightarrow{k_p} A^\bullet + D^{\bullet+} \qquad (17)$$

where k_d is the diffusion rate constant, k_{-d} is the dissociation rate constant, k_e and k_{-e} are the forward and backward electron transfer rate constants, and k_p is the rate constant for pair separation. $(A^+)^*$ that represents the acceptor (i.e. $pyRe(CO)_3(bpy)^+$ and/or pendants $-Re^I(CO)_3(bpy)^+$ in poly-II) in its MLCT excited state and D the amine donor.

Under the assumption that k_p is much larger than k_{-e}, which is supported by the observation of the $-Re^I(CO)_3(bpy)^-$ radical species by flash photolysis experiments,[37] the overall rate constant may be approximately written as:

$$k_q = \frac{k_d}{1 + \frac{k_{-d}}{\kappa \nu_N} \exp\left(\frac{\Delta G^*}{RT}\right)} \qquad (18)$$

where κ is the transmission coefficient of electron transfer, which is 1 in the classical limit, and ν_N is the frequency factor, which varies from the order of 10^{12} to 10^{14} s^{-1} and can be approximated to be of the order of $10^{13}s^{-1}$. ΔG^* is the activation free energy for the electron-transfer step.

Several relationships between ΔG^* and ΔG have been proposed. In the classical parabolic Marcus equation, ΔG^* becomes (eq. 19):

$$\Delta G^* = \frac{(\lambda + \Delta G)^2}{4\lambda} \qquad (19)$$

where λ/4 is the activation free energy when $\Delta G = 0$ (intrinsic barrier). Here λ, the total reorganization energy, is considered to be the sum of the inner-sphere (λ_{in}) and solvent (λ_{out}) contributions:

$$\lambda = \lambda_{in} + \lambda_{out} \quad (20)$$

The solvent reorganization energy may be estimated by:

$$\lambda_{out} = e^2\left(\frac{1}{2r_D} + \frac{1}{2r_A} - \frac{1}{r_{DA}}\right)\left(\frac{1}{n^2} - \frac{1}{\varepsilon}\right) \quad (21)$$

where r_D and r_A are the radii of the donor and acceptor, r_{DA} is the distance between donor and acceptor in the encounter complex, n is the refractive index of the solvent, and ε is the solvent dielectric constant. Using a mean value of r_D for all amines and a value of r_A = 8Å for $pyRe(CO)_3(bpy)^+$ from interatomic distances obtained from similar related Re(I) compounds, a value of 0.7 eV may be estimated for λ_{out}.[37]

The diffusion rate constant (k_d), calculated according to Smoluchowski for non-charged molecules, has a value of 2.0×10^{10} $M^{-1}s^{-1}$ in acetonitrile.[37] Following the Fuoss and Eigen equation, K_d, i.e., the equilibrium constant of the encounter complex ($K_d = k_d/k_{-d}$), may be estimated as 5.4 M^{-1} and hence $k_{-d} = 3.7x10^9 s^{-1}$.

However, in order to fit the experimental results for bimolecular charge separation reactions where the inverted effect predicted by the parabolic Marcus expression is not observed and asymptotic behavior is obtained for k_q at higher exoergonic reactions, an expression of ΔG^* that tends asymptotically toward zero for highly negative values of ΔG is necessary. The Rehm-Weller relationship, eq. 22, meets this requirement.

$$\Delta G^* = \frac{\Delta G}{2} + \left[\left(\frac{\Delta G}{2}\right)^2 + \left(\frac{\lambda}{4}\right)^2\right]^{1/2} \quad (22)$$

Relationship between rate constants and Δ*G*. The experimental values of $k_{q,1}$ and $k_{q,2}$ are plotted against ΔG in Figure 10. The rate constant for luminescence quenching of $pyRe(CO)_3(bpy)^+$, $k_{q,1}$, increases as the driving force becomes less positive, i.e. -0.6 eV < ΔG < 0.2 eV. Eventually, it reaches the diffusional value, k_d, when -1.2 eV < ΔG < -0.7, and for more negative values of ΔG, an asymptotic plateau is obtained. Luminescence quenching of poly-II shows a similar behavior: $k_{q,2}$ increases as ΔG varies between 0.2 and -0.7 eV and it reaches the diffusional value at $\Delta G \sim$ -0.9 eV. However, at more negative values, it shows "vestiges" of inverted region behavior. At ΔG = -1.15 eV, $k_{q,2}$ is 4.8 $x10^9$ $M^{-1}s^{-1}$, i.e. slightly lower than k_d. This is a situation that is often encountered in studies of bimolecular electron transfer reactions at high exoergonic reactions. A comparison of the values of $k_{q,1}$ and $k_{q,2}$ shown in Table 3 indicates that, in general, $k_{q,2}$ is slightly higher than $k_{q,1}$ for values of -0.6 eV < ΔG < 0.2 eV. For ΔG < -0.7 eV, this situation is reversed and $k_{q,1}$ becomes higher than $k_{q,2}$. In fitting experimental k_q values with either Marcus and/or Rehm-Weller model for ΔG^*, it was observed that $k_{q,1}$ values were better fitted by the Rehm-Weller model (Figure 10d), while $k_{q,2}$ values were better represented by the Marcus model (Figure 10a) for ΔG^*, as it is suggested by the correlation coefficients shown in Table 4 and Figure 10. Figures 10a, b, c and d show the best fitting of experimental data points to the Marcus and Rehm-Weller expression of ΔG using eqs. 18, 19 and eqs. 18, 22, respectively. The best fit was obtained using a $k_d = 2 \times 10^{10}$ $M^{-1}s^{-1}$ and the values of κ and λ collected in Table 4.

Table 4. Transmission electron coefficients (κ) and total reorganization energy (λ) for MLCT luminescence quenching of $pyRe(CO)_3(bpy)^+$ and poly-II by amines. R stands for the correlation coefficient for each fit of the experimental values of k_q for $pyRe(CO)_3(bpy)^+$/ poly-II with Marcus and/or Rehm-Weller models of ΔG*. Data taken from ref. 37

System	Model for ΔG^*	κ	λ/eV	*R*
$pyRe(CO)_3(bpy)^+$	Marcus	(2 ± 1) x 10^{-2}	1.2 ± 0.1	0.94
	Rehm-Weller	(2 ± 1) x 10^{-2}	1.1 ± 0.2	0.96
Poly-II	Marcus	(7 ± 1) x 10^{-4}	0.80 ± 0.03	0.89
	Rehm-Weller	(9 ± 5) x 10^{-4}	0.6 ± 0.2	0.83

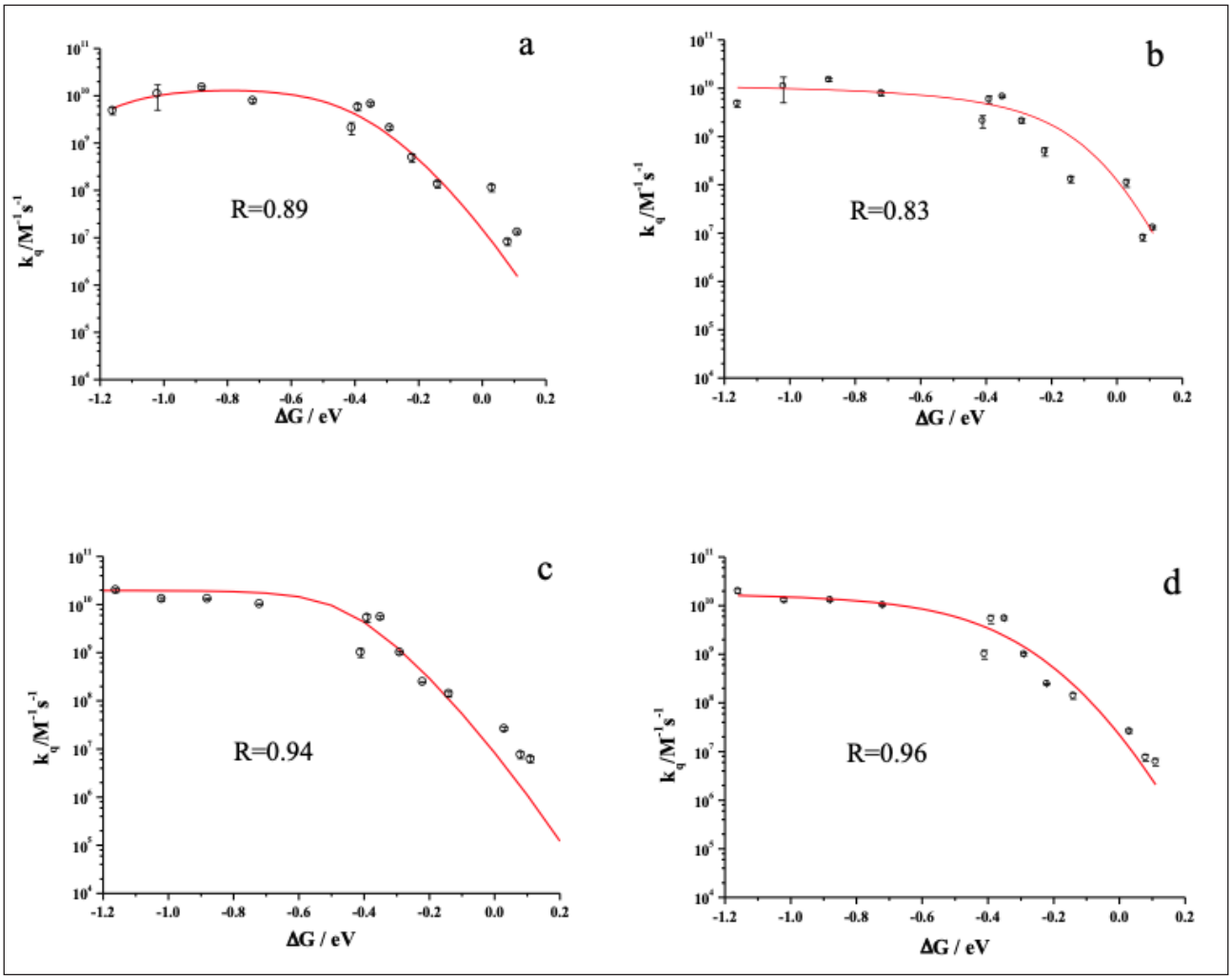

Figure 10. Quenching rate constant dependence on Δ*G* for MLCT luminescence quenching by amines. Figures 10 (a, b) show $k_{q,2}$ vs. Δ*G* for poly-II. The solid line in Fig. 10a shows the best fitting of experimental data points to the Marcus expression of Δ*G*, while the solid line in Fig. 10b shows the best fitting of experimental data points to the Rehm-Weller expression of Δ*G*. Figures 10 (c, d) show $k_{q,1}$ vs. Δ*G* for pyRe(CO)$_3$(bpy)$^+$. The solid line in Fig. 10c shows the best fitting of experimental data points to the Marcus expression of Δ*G*, while the solid line in Fig. 10d shows the best fitting of experimental data points to the Rehm-Weller expression of Δ*G*. The values of κ and λ obtained by the curve fit analysis of Figs. 10 a, b, c and d are collected in Table 5. R stands for the regression coefficient.

Even though the Marcus model for poly-II seems to better describe the k_q relationship with Δ*G* and the Rehm-Weller model seems to be better for pyRe(CO)$_3$(bpy)$^+$, there are two features in which both models are coincident: (i) total reorganization energy (λ) is higher by about 0.3-0.5 eV for pyRe(CO)$_3$(bpy)$^+$ than for poly-II; (ii) the quenching reaction of MLCT by amines is a non-adiabatic reaction (κ~1x10^{-3}-1x10^{-2}). It is important to recall, at this point, that TEM and DLS studies on poly-II demonstrated that Re^I polymer molecules aggregate to form spherical nanoaggregates of radius *R* ~ 156 nm (*vide supra*). The fact that the motion of solvent molecules is retarded by several orders of magnitude in restricted media such as micelles or aggregates, compared to that in homogeneous solvents, is a well-known fact. Thus, solvent reorganization may not be contributing entirely within the time scale of the electron transfer reaction between poly-II MLCT and amines. Higher values of λ are thus expected for pyRe(CO)$_3$(bpy)$^+$ than for poly-II, see Table 4. For $\Delta G < \lambda$, the limiting value of ΔG^* from Equation 19 tends to $\Delta G^* \sim \frac{1}{2}(\Delta G) + \frac{1}{4}(\lambda)$. Since λ is higher for pyRe(CO)$_3$(bpy)$^+$ than for poly-II, then $k_{q,2} \geq k_{q,1}$. However, vibrational modes of uncomplexed pyridines in the polymer backbone may be contributing to a decrease of λ_{in}, explaining the fact that $k_{q,2} \geq k_{q,1}$ for most of the amines studied. Nonetheless, since the amine might have a certain tendency to be close to the polymer by hydrogen bonding interactions with the free pyridine groups, the amine molecules diffusion to form the encounter complex with the –Re(CO)$_3$(bpy)$^+$ chromophore may be favored, compared to pyRe(CO)$_3$(bpy)$^+$, explaining a higher value of k_q in poly-II than in pyRe(CO)$_3$(bpy)$^+$. There might be a simultaneous contribution of these three effects for $k_{q,2} \geq k_{q,1}$ in the normal region. In the inverted region (-Δ*G* >λ) for higher exothermic quenching reactions, the absence of a solvent reorganization in the quenching of poly-II MLCT luminescence by amines may explain a slight tendency of $k_{q,2}$ to decrease while $k_{q,1} \sim k_d$.

Conclusions

Polymers derived from P4VP with attached $–Re(CO)_3(N^N)^+$ pendants show remarkable differences in their photophysical and photochemical properties when compared to the single $LRe(CO)_3(N^N)$ molecules, mainly due to two distinctive properties: (i) the proximity of metallic centers in the polymers, which allows the observation of annihilation processes of the excited states that are not observed in diluted solutions of the single *fac*-$LRe(CO)_3(N^N)$ molecules, and (ii) the solvent/temperature dependent aggregation of polymer strands that impose different morphologies, which ultimate deeply affect the photophysical properties of the attached $–Re(CO)_3(N^N)^+$ pendants. In addition, and connected to (ii), a retardation of the molecular motion due to the restricted media might favor the observation of the Marcus *inverted effect* in bimolecular reactions due to the fact that low values of the solvent reorganization energies may be achieved within aggregates.

Acknowledgements

This work was supported by CONICET (PIP 0389), ANPCyT (PICT0423 and 1435), UNLP (11X/611 and X679), Argentina. E.W. is a member of CONICET

References

[1] Vlček, A.: Ultrafast Excited-State Processes in Re(I) Carbonyl-Diimine Complexes: From Excitation to Photochemistry. In *Photophysics of Organometallics*; Lees, A. J., Ed.; Topics in Organometallic Chemistry; Springer Berlin / Heidelberg, 2010; Vol. 29; pp 73-114.

[2] Fox, M. A.; Chanon, M. *Photoinduced Electron Transfer; Elsevier, Amsterdam, 1988.*

[3] Balzani, V.; Bolletta, F.; Gandolfi, M.; Maestri, M.: Bimolecular electron transfer reactions of the excited states of transition metal complexes. In *Organic Chemistry and Theory*; Topics in Current Chemistry; Springer Berlin / Heidelberg, 1978; Vol. 75; pp 1-64.

[4] Grätzel, M. *Energy Resources Through Photochemistry and Catalysis, Academic Press, New York, 1983.*

[5] Kalyanasundaram, K. Photophysics, photochemistry and solar energy conversion with tris(bipyridyl)ruthenium(II) and its analogues. *Coord. Chem. Rev.*, *46*, 159-244, 1982.

[6] Kalyanasundaram, K.; Grätzel, M. *Photosensitization and Photocatalysis Using Inorganic and Organometallic Compounds, Kluwer Academic Publishers, Dordrecht, 1993.*

[7] Sacksteder, L.; Lee, M.; Demas, J. N.; DeGraff, B. A. Long-lived, highly luminescent rhenium(I) complexes as molecular probes: intra- and intermolecular excited-state interactions. *J. Am. Chem. Soc.*, *115*, 8230-8238, 1993.

[8] Yam, V. W.-W.; Wong, K. M.-C.; Lee, V. W.-M.; Lo, K. K.-W.; Cheung, K.-K. Synthesis, photophysics, ion-binding studies, and structural characterization of organometallic rhenium(I) crown complexes. *Organometallics*, *14*, 4034-4036, 1995.

[9] Yoon, D. I.; Berg-Brennan, C. A.; Lu, H.; Hupp, J. T. Synthesis and preliminary photophysical studies of intramolecular electron transfer in crown-linked donor- (chromophore-) acceptor complexes. *Inorg. Chem.*, *31*, 3192-3194, 1992.

[10] Calabrese, J. C.; Tam, W. Organometallics for non-linear optics: Metal-pyridine and bipyridine complexes. *Chem. Phys. Lett.*, *133*, 244-245, 1987.

[11] Ehler, T. T.; Malmberg, N.; Carron, K.; Sullivan, B. P.; Noe, L. J. Studies of Organometallic Self-Assembled Monolayers on Ag and Au Using Surface Plasmon Spectroscopy. *J. Phys. Chem. B*, *101*, 3174-3180, 1997.

[12] Yam, V. W.-W.; Lau, V. C.-Y.; Cheung, K.-K. Synthesis, photophysics and photochemistry of novel luminescent rhenium(I) photoswitchable materials. *J. Chem. Soc. Chem. Com.*, 259-261, 1995.

[13] Connick, W. B.; Di Bilio, A. J.; Hill, M. G.; Winkler, J. R.; Gray, H. B. Tricarbonyl(1,10-phenanthroline) (imidazole) rhenium(I): a powerful photooxidant for investigations of electron tunneling in proteins. *Inorg. Chim. Acta*, *240*, 169-173, 1995.

[14] Di Bilio, A. J.; Crane, B. R.; Wehbi, W. A.; Kiser, C. N.; Abu-Omar, M. M.; Carlos, R. M.; Richards, J. H.; Winkler, J. R.; Gray, H. B. Properties of Photogenerated Tryptophan and Tyrosyl Radicals in Structurally Characterized Proteins Containing Rhenium(I) Tricarbonyl Diimines. *J. Am. Chem. Soc.*, *123*, 3181-3182, 2001.

[15] Miller, J. E.; Di Bilio, A. J.; Wehbi, W. A.; Green, M. T.; Museth, A. K.; Richards, J. R.; Winkler, J. R.; Gray, H. B. Electron tunneling in rhenium-modified Pseudomonas aeruginosa azurins. *Biochim. Biophys. Acta*, *1655*, 59-63, 2004.

[16] Biver, T.; Secco, F.; Venturini, M. Mechanistic aspects of the interaction of intercalating metal complexes with nucleic acids. *Coord. Chem. Rev.*, *252*, 1163-1177, 2008.

[17] Ruiz, G. T.; Juliarena, M. P.; Lezna, R. O.; Wolcan, E.; Feliz, M. R.; Ferraudi, G. Intercalation of fac-[(4,4′-bpy) ReI(CO) 3(dppz)]+, dppz = dipyridyl[3,2-a:2′3′-c] phenazine, in polynucleotides. on the UV-vis photophysics of the Re(i) intercalator and the redox reactions with pulse radiolysis-generated radicals. *Dalton Trans.*, 2020-2029, 2007.

[18] Armaroli, N.; Accorsi, G.; Felder, D.; Nierengarten, J.-F. Photophysical Properties of the ReI and RuII Complexes of a New C60-Substituted Bipyridine Ligand. *Chem. Eur. J.*, *8*, 2314-2323, 2002.

[19] Bracco, L. L. B.; Juliarena, M. P.; Ruiz, G. T.; Féliz, M. R.; Ferraudi, G. J.; Wolcan, E. Resonance energy transfer in the solution phase photophysics of -Re(CO)3L+ pendants bonded to poly(4-vinylpyridine). *Journal of Physical Chemistry B*, *112*, 11506-11516, 2008.

[20] Baxter, S. M.; Jones, W. E.; Danielson, E.; Worl, L.; Strouse, G.; Younathan, J.; Meyer, T. J. Photoinduced electron and energy transfer in soluble polymers. *Coord. Chem. Rev.*, *111*, 47-71, 1991.

[21] Chen, L. X.; Jäger, W. J. H.; Gosztola, D. J.; Niemczyk, M. P.; Wasielewski, M. R. Ionochromic Effects and Structures of Metalated Poly(p-phenylenevinylene) Polymers Incorporating 2,2‘-Bipyridines. *J. Phys. Chem. B*, *104*, 1950-1960, 2000.

[22] Wang, B.; Wasielewski, M. R. Design and Synthesis of Metal Ion-Recognition-Induced Conjugated Polymers: An Approach to Metal Ion Sensory Materials. *J. Am. Chem. Soc.*, *119*, 12-21, 1997.

[23] Wang, Q.; Wang, L.; Yu, L. Synthesis and Unusual Physical Behavior of a Photorefractive Polymer Containing Tris(bipyridyl)ruthenium(II) Complexes as a Photosensitizer and Exhibiting a Low Glass-Transition Temperature. *J. Am. Chem. Soc.*, *120*, 12860-12868, 1998.

[24] Olmsted, J.; McClanahan, S. F.; Danielson, E.; Younathan, J. N.; Meyer, T. J. Electron and energy shuttling between redox sites on soluble polymers. *J. Am. Chem. Soc.*, *109*, 3297-3301, 1987.

[25] Younathan, J. N.; McClanahan, S. F.; Meyer, T. J. Synthesis and characterization of soluble polymers containing electron- and energy-transfer reagents. *Macromol.*, *22*, 1048-1054, 1989.

[26] Worl, L. A.; Strouse, G. F.; Younathan, J. N.; Baxter, S. M.; Meyer, T. J. Production and storage of multiple, photochemical redox equivalents on a soluble polymer. *J. Am. Chem. Soc.*, *112*, 7571-7578, 1990.

[27] Jones, W. E.; Baxter, S. M.; Strouse, G. F.; Meyer, T. J. Intrastrand electron and energy transfer between polypyridyl complexes on a soluble polymer. *J. Am. Chem. Soc.*, *115*, 7363-7373, 1993.

[28] Dupray, L. M.; Meyer, T. J. Synthesis and Characterization of Amide-Derivatized, Polypyridyl-Based Metallopolymers. *Inorg. Chem.*, *35*, 6299-6307, 1996.

[29] Suzuki, M.; Kimura, M.; Hanabusa, K.; Shirai, H. Photosensitized charge separation using water-insoluble polymer-bound ruthenium(ii) complex films. *Journal of the Chemical Society, Faraday Transactions*, *93*, 4137-4143, 1997.

[30] Dupray, L. M.; Devenney, M.; Striplin, D. R.; Meyer, T. J. An Antenna Polymer for Visible Energy Transfer. *J. Am. Chem. Soc.*, *119*, 10243-10244, 1997.

[31] Friesen, D. A.; Kajita, T.; Danielson, E.; Meyer, T. J. Preparation and Photophysical Properties of Amide-Linked, Polypyridylruthenium-Derivatized Polystyrene. *Inorg. Chem.*, *37*, 2756-2762, 1998.

[32] Worl, L. A.; Jones, W. E.; Strouse, G. F.; Younathan, J. N.; Danielson, E.; Maxwell, K. A.; Sykora, M.; Meyer, T. J. Multiphoton, Multielectron Transfer Photochemistry in a Soluble Polymer. *Inorg. Chem.*, *38*, 2705-2708, 1999.

[33] Smith, G. D.; Maxwell, K. A.; DeSimone, J. M.; Meyer, T. J.; Palmer, R. A. Step-Scan FTIR Time-Resolved Spectroscopy Study of Excited-State Dipole Orientation in Soluble Metallopolymers. *Inorg. Chem.*, *39*, 893-898, 2000.

[34] Connors, P. J.; Tzalis, D.; Dunnick, A. L.; Tor, Y. Coordination Compounds as Building Blocks: Single-Step Synthesis of Heteronuclear Multimetallic Complexes Containing RuII and OsII. *Inorg. Chem.*, *37*, 1121-1123, 1998.

[35] Hou, S.; Chan, W. K. Polymer aggregates formed by polystyrene-block-poly(4-vinyl-pyridine) functionalized with rhenium(I) 2,2′-bipyridyl complexes. *Macrom. Rap. Com.*, *20*, 440-443, 1999.

[36] Bracco, L. L. B.; Einschlag, F. S. G.; Wolcan, E.; Ferraudi, G. J. On the mechanism of the photoinduced reduction of an adduct of ferricytochrome C with a poly(4-vinylpyridine) polymer containing -ReI (CO)3(3,4,7,8-tetramethyl-1,10-phenanthroline) pendants. *J. Photochem. Photobiol. A*, *208*, 50-58, 2009.

[37] Bracco, L. L. B.; Féliz, M. R.; Wolcan, E. On the quenching of MLCT luminescence by amines: The effect of nanoaggregation in the decrease of the reorganization energy. *J. Photochem. Photobiol. A*, *210*, 23-30, 2010.

[38] Bracco, L. L. B.; Lezna, R. O.; Muñoz-Zuñiga, J.; Ruiz, G. T.; Féliz, M. R.; Ferraudi, G. J.; Einschlag, F. S. G.; Wolcan, E. On the mechanism of formation and spectral properties of radical anions generated by the reduction of –[Re I(CO) 3(5-nitro-1,10-phenanthroline)] + and –[Re I(CO) 3(3,4,7,8-tetramethyl-1,10-phenanthroline)] + pendants in poly-4-vinylpyridine polymers. *Inorg. Chim. Acta*, *370*, 482-491, 2011.

[39] Wolcan, E.; Alessandrini, J. L.; Féliz, M. R. On the quenching of MLCTRe-bpy luminescence by Cu(II) species in Re(I) polymer micelles. *J. Phys. Chem. B*, *109*, 22890-22898, 2005.

[40] Wolcan, E.; Féliz, M. R. Temperature and medium effects on the photophysical properties of -Re(CO)3(2,2′-bipyridine) pendant chromophores coordinated to a poly(4-vinylpyridine) backbone. *Photochem. & Photobiol. Sci.*, *2*, 412-417, 2003.

[41] Wolcan, E.; Feliz, M. R.; Alessandrini, J. L.; Ferraudi, G. Aggregation in nanobundles and the effect of diverse environments on the solution-phase photochemistry and photophysics of -Re(CO)3L + (L = 1,10-phenanthroline, 2,2′-bipyridine) pendants bonded to poly(4-vinylpyridine). *Inorg. Chem.*, *45*, 6666-6677, 2006.

[42] Wolcan, E.; Ferraudi, G. Photochemical and photophysical properties of Fac-Re(I) tricarbonyl complexes: A comparison of monomer and polymer species with - ReI(CO)3phen chromophores. *J. Phys. Chem. A*, *104*, 9285-9286, 2000.

[43] Wolcan, E.; Ferraudi, G.; Feliz, M. R.; Gómez, R. V.; Mikelsons, L. UV photolysis of a Re(I) macromolecule, [(4-vinylpyridine)2 (4-vinylpyridineRe(CO)3(1,10-phenanthroline)+] 200: Addition of C-centered radicals to coordinated CO. *Supramolecular Chemistry*, *15*, 143-148, 2003.

[44] Féliz, M. R.; Ferraudi, G. Contrasting Intrastrand Photoinduced Processes in Macromolecules Containing Pendant -Re(CO)3(1,10-phenanthroline)+: Electron versus Energy Transfer. *Inorg. Chem.*, *43* 1551-1557, 2004.

[45] Moncada, A. S.; Einschlag, F. S. G.; Prieto, E. D.; Ruiz, G. T.; Lappin, A. G.; Ferraudi, G. J.; Wolcan, E. Photophysical properties of Re(I)(CO)3(phen) pendants grafted to a poly-4-vinylpyridine backbone. A correlation between photophysical properties and morphological changes of the backbone. *J. Photochem. Photobiol. A*, *321*, 284-296, 2016.

[46] Moncada, A. S.; Gutiérrez-Pineda, E.; Maisuls, I.; Ruiz, G. T.; Lappin, A. G.; Ferraudi, G. J.; Wolcan, E. Photochemical properties of a Re(I) polymer containing dppz in its structure. An interplay between dark and bright states of dppz. *J. Photochem. Photobiol. A*, *353*, 86-100, 2018.

[47] Cheng, K. W.; Chan, W. K. Morphology of Rhenium Complex-Containing Polystyrene-block-poly(4-vinylpyridine) and Its Use as Self-Assembly Templates for Nanoparticles. *Langmuir*, *21*, 5247-5250, 2005.

[48] Hou, S.; Man, K. Y. K.; Chan, W. K. Nanosized Micelles Formed by the Self-assembly of Amphiphilic Block Copolymers with Luminescent Rhenium Complexes. *Langmuir*, *19*, 2485-2490, 2003.

[49] Kumbhakar, M.; Nath, S.; Mukherjee, T.; Pal, H. Intermolecular electron transfer between coumarin dyes and aromatic amines in Triton-X-100 micellar solutions: evidence for Marcus inverted region. *J. Chem. Phys.*, *120*, 2824-2834, 2004.

[50] Rehm, D.; Weller, A. Kinetics of Fluorescence Quenching by Electron and H-Atom Transfer. *Isr. J. Chem.*, *8*, 259-271, 1970.

Bio

Ezequiel Wolcan

Ezequiel Wolcan obtained his BSc (1991) and Ph.D. (1996) at The National University of La Plata (UNLP), Argentina, after which he was the recipient of a Fulbright Research Scholarship at the University of Notre Dame, Indiana, USA. He returned to Argentina, where he joined the staff of the Institute of Research in Applied and Theoretical Physical Chemistry (INIFTA). He was appointed as a Full Professor at the UNLP in 2016. He is now a Principal Researcher of the Argentinian National Research Council (CONICET) at INIFTA where he leads a research group working on the photochemistry of coordination compounds in supramolecular structures, polymers and nanocomposites.

INSTRUCTIONS FOR AUTHORS

GUIDELINES

1. Length

Research reviews should not be less than 7000 words or more than 10,000 words (plus up to 15 figures and up to 50 references).

2. Structure

Whenever possible articles should adjust to the standard structure comprising:
(a) Graphical abstract,
(b) Abstract,
(c) Introduction describing the focus of the review,
(d) Article main body including assessment and discussion of available information (may be further subdivided),
(e) Conclusions,
(f) Bibliography.

3. Format

Authors must submit their articles in a Microsoft Word archive. Figures must be embedded in the article and also submitted in a separate .zip or .rar file.

4. References

References must be numbered in the text ([1] [2] [3]) and identified with the same numbers in the *References* section. Up to 50 references are allowed. The following are examples to take into account in each case.

BOOKS:
- *Single author*
Chung, R. *General Chemistry: Fundamental Knowledge,* 2nd ed.; McGuffin-Hill: Kansas City, 2003.
- *More than one author*
Chung, R.; Williamson, M. *General Chemistry: Fundamental Knowledge*, 2nd ed.; McGuffin-Hill: Kansas City, 2003.
- *Edited Book*
Kurti, F. Photodissociation and Reactive Scattering. In *The Rise of Chemical Physics*; White, AD, Ed.; Wilson: New Jersey, 2007; Vol. 128; p. 257.
- *Book in Series*
Goth, V. Polymer Chemistry. In *The Foundational Course in Organic Chemistry*; ACDC Symposium Series 1151; American Chemical Fraternity: Seattle, 2014; pp 123-149.
- *Article from a reference book*
Powder and Metallurgy. *Dictionary of Chemical Technology*, 3rd ed.; Wilson: New Jersey, 1971; Vol. 12, pp 68-82.

ARTICLES:
- *Article in a scientific journal*
Evans, A.; Stitch, M.; Smithers, ET; Nope, JJ Complex Aldol Reactions to the Total Synthesis of Phorboxazole B. *J. Am. Chem*. Soc. 2012, 122, 10033-10046.
- *Article in a popular/non-scientific magazine*
Tatum, CJ Super Organics. *Wireless* , June 2001, pp 76-93.
- *Article from an online journal*
Turkey-Lopez, E. Inexact Solutions of the Quantum Double Square-Well Potential. *Chem. Ed.* [Online] 2007, 11, pp. 838-847. http://chemeducator.org/bibs/0011006/11060380lb.htm (accessed Aug 5, 2019).

PUBLICATION ETHICS

The journal considers that the primary objective of all submissions must be a contribution of relevant and appropriate content, and that all review processes must be structured based on that general criterion. Therefore, there is an emphasis on the concern to maintain the highest quality and ethics standards in the reception, evaluation and publication of articles. These standards include the three participants of the process: author, reviewer and editor.

1. Author's responsibilities

- Submitted manuscripts should maintain rigorous scientific criteria for data validation and conclusions.
- All data (Figures, Tables, etc.) reproduced from previous published articles must give the appropriate recognition to the source. Plagiarism is cause enough to reject the submission.
- Authorship must include all individuals who have contributed in a substantial way to the composition, prior investigation, and execution of the paper. Minor contributions must be acknowledged, but these contributors should not be listed as authors. The main author or authors of the article will make sure that all participants of the paper have approved the final version of the document submitted.
- All authors must reveal in their final manuscript any financial or other type of conflict of interests that might interfere with the results and interpretations in their research. All funding received to carry out the project must be acknowledged.
- After the article is published, in the event an author notices a crucial fault or inaccuracy, he or she should immediately report that fault or inaccuracy, so that an Erratum can be issued as soon as possible.

2. Reviewer's responsibilities

Reviewing is a time-consuming process that is carried out *ad honorem* by *bona fide* scientists conversant with the subject of the reviewed paper. The quality and the ethical standards of the journal depend critically on the quality of the reviewing process, and the following guidelines are established:

- All documents sent to the journal for review will be considered confidential documents and will not be discussed with external third parties.
- When invited, a potential reviewer should decline if: (a) the subject of the article is not within his/her area of expertise; (b) there is any kind of conflict of interest; (c) if the review cannot be finished within the period established by the journal.
- Any criticism or objections to the paper should be done in a neutral tone and based on reasonable grounds, not limited to simple opinions or purely subjective expressions.

3. Editor's responsibilities

- The editors are responsible for selecting the papers that will be published in the journal. The Editorial Management must comply with the ethical standards of the journal, as well as with all legal guidelines, including the prohibition of plagiarism and any other form of copyright infringement.
- The editors will evaluate and make decisions on the articles sent to the journal regardless of the gender, sexual orientation, religious beliefs, ethnic origin, nationality or political ideology of the authors.
- Revealing information identifying reviewers is forbidden.
- The final version of all materials can be published only with the prior approval of their author.
- The editors will refrain from publishing manuscripts that imply a conflict of interests because of any possible connection with other institutions, companies and authors.
- Before deciding to send an article to a peer review, the editors are committed to thoroughly read all texts received and determine their appropriateness to the thematic universe of the journal.
- If a misbehavior or unethical action by an author or reviewer is identified, the editors must request the informer of such conduct or action to provide the evidence that may justify a possible investigation. All accusations will be handled seriously until reliable results are obtained regarding its truthfulness or falseness. If an investigation takes place, the editors are responsible for choosing the appropriate way in which it will be carried out. They can also request the advice and assistance from the Editorial Board, as well as from reviewers and authors.
- In the event a serious non-malicious mistake or a dishonest conduct by an author or a reviewer is proved, the editors shall act according to the nature and seriousness of the case. The actions the editors may take include, but are not limited to: notifying the author or reviewer of the existence of a serious mistake or misapplication of the ethical standards of the journal; writing a strong statement that reports and warns about a bad practice or unethical behavior; publishing that statement; unilaterally withdrawing the reported paper from the review or publication process; revoking the paper if it has already been published; communicating the journal's decision and the reasons behind it to the general public; and banning paper submissions by the people involved for a certain period of time.

PRIVACY STATEMENT

The names and email addresses entered in this journal site will be used exclusively for the stated purposes of this journal and will not be made available for any other purpose or to any other party.

NEXT ISSUE

Vol. 1, No. 3

TO BE PUBLISHED ON JUNE 15, 2020

GUEST EDITOR: CRISTINA HOPPE

ARTICLES

ISSN 2683-9288

Science Reviews
from the end of the world

Centro de Estudios sobre Ciencia, Desarrollo y
Educación Superior
538 Pueyrredón Av. - 2° C – Second building
Buenos Aires, Argentina - C1032ABS
(54 11) 4963-7878/8811
sciencereviews@centroredes.org.ar
www.scirevfew.net